On the Geometric Conservation Law for the Non-Linear Frequency Domain and Time Spectral Methods in Aerodynamic Computations

Marc Benoit

Master of Engineering

Department of Mechanical Engineering

McGill University
Montreal, Quebec
April 2018

A thesis submitted to McGill University in partial fulfilment of the requirements of the degree of Master of Engineering

> © Marc Benoit All rights reserved 2018

ACKNOWLEDGMENTS

First of all, I would like to thank my supervisor Professor Siva Nadarajah who accepted my transfer to the Thesis program. It was his enthusiasm and his vast technical insight during the course of Subsonic Aerodynamics that inspired me to approach him for a research topic. His constant encouragements, his confidence in my progress and his patience were indispensable assets throughout this research. Secondly, I would like to thank all my colleagues from the Computational Aerodynamics Group. A very special thanks to Philip Zwanenburg and Aditya Kashi for their invaluable advice and their technical help. I will always be indebted for their support and friendship. I would like also to extend my gratitude to Doug Shi-Dong for the many questions I had and who always took time to answer me.

Last but not least, I want to express my deepest gratitude to my parents and my family for their constant support through all my years of study.

This research has benefited from the generous support of the Natural Sciences and Engineering Research Council of Canada (NSERC).

ABSTRACT

Novel approaches to enforce the Geometric Conservation Law (GCL) on moving grids using spectral in time solvers are introduced. The governing equations are based on the Arbitrary Lagrangian-Eulerian formulation of the Navier-Stokes equations, discretized in time through either the Non-Linear Frequency Domain (NLFD) or the Time-Spectral (TS) methods. The equations are spatially discretized by a structured finite-volume scheme on three-dimensional hexahedral meshes or two-dimensional quadrilateral grids. The derived methodologies follow a general approach where the positions and the velocities of the grid points are known at each time step based on the dynamic mesh deformation using the Radial Basis Functions (RBF) technique. The Integrated Face Mesh Velocities (IFMV) are derived either from the Approximation of the Exact Volumetric Increments (AEVI) relative to the undeformed mesh or exactly computed based on a Mapping (MAP) between the physical domain and the computational space. It was shown that satisfying the GCL does not guarantee that the errors in the Integrated Face Mesh Velocities (IFMV) are either at the same level or converge at the same rate. The methods are validated numerically by verifying the conservation of uniform flow and by comparing the integrated face mesh velocities to the exact values derived from the mapping. Their impact on aerodynamic computations is evaluated through two-dimensional plunging or pitching simulations of a cylinder and a NACA0012 airfoil.

ABRÉGÉ

De nouvelles méthodes pour résoudre les Lois de Conservation Géométriques sur des maillages déformables sont introduites pour une discrétisation temporelle des équations fondamentales de la mécanique des fluides selon des approches spectrales. Les équations de Navier et Stokes sont exprimées selon la formulation arbitrairement Lagrangienne-Eulérienne, et sont discrétisées en temps par la méthode non linéaire dans le domaine fréquentiel ou par la méthode en temps spectral. La discrétisation spatiale des équations utilise la technique des volumes finis pour des maillages tridimensionnels hexaédriques ou bidimensionnels composés de quadrilatères. Les méthodologies de résolution proposées suivent une approche globale où seules les positions et vitesses des noeuds du maillage sont connues à partir de sa déformation par la technique d'interpolation des fonctions en base radiale. Les vitesses du maillage intégrées sur chaque face sont obtenues soit en utilisant une approximation la plus précise possible des incréments volumiques de chaque élément, ou exactement calculées par l'intermédiaire d'une cartographie entre l'espace physique et l'espace numérique. Il est observé que satisfaire les Lois de Conservation Géométriques ne garantit pas que l'erreur sur les vitesses de maillage intégrées sur chaque face soit du même ordre ou converge à la même vitesse. Les méthodes sont validées numériquement en vérifiant la conservation d'un écoulement uniforme et en comparant les valeurs des vitesses de maillage intégrées sur chaque face. Les effets de ces différentes approches sur le calcul des coefficients aérodynamiques sont évalués en effectuant des simulations de mouvements oscillatoires d'un cylindre et d'un profil d'aile NACA0012.

NOMENCLATURE

This section defines the main abbreviations and symbols employed in this thesis. Unless it is specified otherwise by the subscript " \mathcal{C} ", all relevant spatial quantities are expressed in physical space. When necessary local modifications and additional variables will be introduced directly in the text of the dissertation.

Abbreviation

AEVI Approximation of the Exact Volumetric Increment

ALE Arbitrary Lagrangian-Eulerian

AVG Average

BI-MAP Bilinear Mapping

DFT Discrete Fourier Transform

GCL Geometric Conservation Law

IDFT Inverse Discrete Fourier Transform

IFMV Integrated Face Mesh Velocity

LVI Linear Volumetric Increment

NLFD Non-Linear Frequency Domain

RBF Radial Basis Functions

SCL Surface Conservation Law

TRI-MAP Trilinear Mapping

TS Time-Spectral

VCL Volume Conservation Law

Operators

 $(\cdot)^t$ Transpose operator

 $\langle \cdot \rangle_T$ Time-average over a period operator

 \mathcal{L} Scalar triple product operator

 \mathcal{T} Trilinear mapping operator

 ∇ Nabla operator

 \times Cross-product operator

Scalar quantities

 C_D Total drag coefficient

 $C_{D,p}$ Pressure drag

 $C_{D,v}$ Skin friction drag

 C_L Total lift coefficient

 C_{ps} Stagnation pressure coefficient

E Total energy per unit mass

G Sum of the integrated face mesh velocities over a cell faces

 G_m Integrated face mesh velocity

 \hat{G}_k k^{th} Fourier coefficient of the sum of integrated face mesh veloc-

ities over a cell faces

 $\hat{G}_{m,k}$ k^{th} Fourier coefficient of the integrated face mesh velocity

H Total enthalpy per unit mass

 l_m Linear part of the volumetric increment

 M_{∞} Freestream Mach number

N Number of harmonics in the temporal discretization

 N_f Number of faces

 N_{grid} Number of grid points

 N_{RBF} Number of RBF points

 N_{ts} Number of time instances

p Pressure

 p_m Periodic part of the volumetric increment

 Re_{∞} Freestream Reynolds number

 S_t Strouhal number

t Time variable

Temporal period

 T_{emp} Temperature

 V_{∞} Freestream fluid velocity

 α_i RBF interpolation coefficients

 δ_{ij} Kronecker symbol

 γ Heat capacity ratio

 \mathcal{E}_{GCL} Level of convergence of the GCL

 $\mathcal{E}_{IFMV,x}, \mathcal{E}_{IFMV,y}$ Level of convergence of the IFMV

 κ Reduced frequency

 ρ Density

 τ_{ij} Components of viscous stresses

 ϕ RBF basis function

 Ω_m Volumetric increment

 $\hat{\Omega}_k$ k^{th} Fourier coefficient of the volume Ω

 $\hat{\Omega}_{m,k}$ k^{th} Fourier coefficient of the volumetric increment

 $\partial\Omega$ Boundary of the volume Ω

 n_1, n_2, n_3 Cartesian components of unit normal vector

 u_1, u_2, u_3 Cartesian components of fluid velocity vector

 x_1, x_2, x_3 or x, y, z Cartesian components of position vector in physical space

 ξ, η, ζ Cartesian components of position vector in computational space

Subscripts

 \mathcal{C} Computational space index

h General hexahedron element (Definition 3.3.2) designation

m Face index

n Time instance index

q Quadrilateral element designation

Vector quantities

 $\mathbf{F_c}$ Inviscid flux vector

 $\mathbf{F}_{\mathbf{c}}^{\mathbf{M}}$ Modified inviscid flux vector for moving boundaries

 $\mathbf{F_d}$ Artificial dissipation flux vector

 $\mathbf{F}_{\mathbf{v}}$ Viscous flux vector

n Normal vector

 $\hat{\mathbf{n}}$ Unit normal vector

 $\hat{\mathbf{N}}_{\mathcal{C}}$ Unit normal vector in computational space

r Position vector

 $\mathbf{r}_{\mathcal{C}}$ Position vector in computational space

Residual vector

 $\hat{\mathbf{R}}_k$ k^{th} Fourier coefficient of the residual vector

 $\hat{\mathbf{R}}_{k}^{*}$ k^{th} Fourier coefficient of the unsteady residual vector

v Velocity vector

 $\mathbf{v}_{\mathcal{C}}$ Velocity vector in computational space

V Contravariant flow velocity vector

 V_t Contravariant boundary velocity vector

 \mathbf{x}_r Position vector of a RBF point in the undeformed mesh

 \mathbf{x}_v Position vector of a grid point in the undeformed mesh

 $\Delta \mathbf{x}_r$ Displacement vector of all RBF points in the x direction

 $\Delta \mathbf{x}_v$ Displacement vector of all grid points in the x direction

w Vector of the conservative variables

 $\bar{\mathbf{w}}$ Modified vector of the conservative variables

 $\hat{\mathbf{w}}_k$ k^{th} Fourier coefficient of the modified vector of the conservative

variables

 \mathcal{A} RBF volume point basis function matrix

D Fourier temporal-derivation operator matrix

 $\mathcal{I}_{\mathcal{N}}$ Identity matrix of dimension 2N+1

M RBF basis function matrix

TABLE OF CONTENTS

ACI	KNOW	TLEDGMENTS ii			
ABS	STRAC	CT			
ABI	RÉGÉ				
NOI	MENC	LATURE vi			
LIST	ГОБТ	ΓABLES xiii			
LIST	г оғ і	FIGURES xiv			
1	Intro	duction			
	1.1 1.2 1.3 1.4	Context1Frequency domain solutions2Mesh deformation and Geometric Conservation Law4Research objectives6			
2	Flow solver framework				
	2.1 2.2 2.3 2.4	Governing equations8Spatial discretization11Temporal discretization12Dynamic mesh deformation14			
3	Deriv	ration and enforcement of the Geometric Conservation Law 17			
	3.1 3.2 3.3	Derivation of the GCL in the NLFD framework			
		5.5.5 Extension to two difficultional quadrilateral grids 90			

	3.4	Alternative approach based on the exact integrated face mesh	
		velocities	41
		3.4.1 Trilinear mapping	41
		3.4.2 Derivation of the GCL in the NLFD framework	48
		3.4.3 Extension to two-dimensional quadrilateral grids	49
	3.5	Extension of the results to Time-Spectral method	50
		3.5.1 Time-Spectral method	51
		3.5.2 Derivation and enforcement of the GCL	53
4	Num	erical validation of the different methodologies	56
	4.1	Protocol	56
	4.2	Test cases	58
		4.2.1 Without RBF	59
		4.2.2 With RBF	60
	4.3	Freestream preservation	61
	4.4	Comparison of the integrated face mesh velocities to the reference value	64
	4.5	Time-Spectral Method	72
	4.6	Discussion	72
5	Two-	-dimensional aerodynamic simulations	74
	5.1	Plunging cylinder	76
	5.2	Pitching cylinder	78
	5.3	Plunging NACA0012 airfoil	82
	5.4	Pitching NACA0012 airfoil	84
		5.4.1 Pitching NACA0012 at $\pm 5^{\circ}$ angle and $\kappa = 2$	84
		5.4.2 Pitching NACA0012 at $\pm 20^{\circ}$ angle and $\kappa = 3 \dots \dots$	87
	5.5	Discussion	94
c	Cons	duction and future work	06

LIST OF TABLES

<u> Fable</u>		page
5–1	Level of satisfaction of the GCL and convergence of the integrated face mesh velocities in the case of the plunging cylinder using $1 \le N \le 7$ harmonics in the DFT	. 76
5–2	Mean values of the drag coefficients in the case of the plunging cylinder with $M_{\infty}=0.3,\ Re_{\infty}=100$ and $St=0.16704.$. 77
5–3	Mean values of the drag coefficients and maximum lift coefficient in the case of the pitching cylinder	. 81
5–4	Level of satisfaction of the GCL and convergence of the integrated face mesh velocities in the case of the plunging NACA0012 using $1 \le N \le 7$ harmonics in the DFT	. 82
5–5	Mean values of the drag coefficients in the case of the plunging NACA0012 with $M_{\infty}=0.2,Re_{\infty}=1850$ and $St=0.288.$. 82
5–6	Mean values of the drag coefficients and maximum lift coefficient in the case of the pitching NACA0012 airfoil at $\pm 5^{\circ}$ and $\kappa=2$. 86
5–7	Mean values of the drag coefficients and maximum lift coefficient in the case of the pitching NACA0012 airfoil at $\pm 20^{\circ}$ and $\kappa = 3$. 87

LIST OF FIGURES

Figure		page
3–1	Example of linear volumetric increment in 2D relatively to a reference time instant t_0	21
3–2	(a) The initial undeformed quadrilateral element is shown in black while the movement of the mesh points is presented in red with two deformed configurations of the cell in dashed lines, (b) Exact volumetric increment for the face 2-3 in the x direction relatively to the initial configuration (in dash dot line) in blue	23
3–3	Trilinear mapping between a "general hexahedron" (Definition 3.3.2) in the physical space and a reference cube in the computational domain	29
3–4	(a) Approximated volumetric increment between two time steps t_{n-1} and $t_n: \Omega_h(t_n)$ (b) Approximation of a volumetric increment as a sum of "general hexahedra" (Definition 3.3.2)	30
3–5	Approximation of a volumetric increment as a sum of quadrilaterals representing the linear volumetric increments between two successive time steps	40
3–6	Bilinear mapping of a quadrilateral in the physical space (x, y) to a reference square in the computational domain (ξ, η)	40
4–1	Mesh deformations of the exterior grid points for cases 2, 4 and 5 at an arbitrary chosen time step	62
4-2	Relative error regarding the uniform flow preservation for each test cas	se 63
4–3	Case 1: (a) Comparison of the sum of the integrated face mesh velocities to the NLFD temporal derivative of the volume (b) Comparison of the individual integrated face mesh velocity to the reference values (TRI-MAP) in the x direction (c) in the y direction (d) in the z direction	65

4–4	Two-dimensional projection of the motion in case 2 for one cell: the exact volumetric increment in the x direction is filled in clear green and in dark blue in the y direction. The blue dashed dot arrows show the paths of the vertices	67
4–5	Case 2: (a) Comparison of the sum of the integrated face mesh velocities to the NLFD temporal derivative of the volume (b) Comparison of the individual integrated face mesh velocity to the values (TRI-MAP) in the x direction (c) in the y direction (d) in the z direction	68
4-6	Case 3: (a) Comparison of the sum of the integrated face mesh velocities to the NLFD temporal derivative of the volume (b) Comparison of the individual integrated face mesh velocity to the values (TRI-MAP) in the x direction (c) in the y direction (d) in the z direction	69
4–7	Case 4: (a) Comparison of the sum of the integrated face mesh velocities to the NLFD temporal derivative of the volume (b) Comparison of the individual integrated face mesh velocity to the values (TRI-MAP) in the x direction (c) in the y direction (d) in the z direction	70
4-8	Case 5: (a) Comparison of the sum of the integrated face mesh velocities to the NLFD temporal derivative of the volume (b) Comparison of the individual integrated face mesh velocity to the values (TRI-MAP) in the x direction (c) in the y direction (d) in the z direction	71
5-1	Near resolution of the undeformed meshes employed for the simulations	75
5–2	Total drag coefficient analysis for a plunging cylinder	78
5–3	Level of satisfaction of the GCL and convergence of the IFMV for the pitching cylinder case	80
5–4	Drag polar C_D vs C_L for the pitching cylinder case	81
5–5	Instantaneous total drag and total lift coefficients over a period for the plunging NACA0012 case	83

5–6	Level of satisfaction of the GCL and convergence of the IFMV for the pitching NACA0012 case at $\pm 5^{\circ}$ and $\kappa = 2 \dots \dots \dots$	85
5-7	Drag polar C_D vs C_L for the NACA0012 airfoil case at $\pm 5^{\circ}$ and $\kappa = 2$	86
5–8	Density residual, level of satisfaction of the GCL and convergence of the IFMV for the pitching NACA0012 case at $\pm 20^\circ$ and $\kappa=3$	88
5–9	Drag polar C_D vs C_L for the NACA0012 airfoil case at $\pm 20^\circ$ and $\kappa = 3$	89
5-10	Error distributions on the IFMV for the pitching NACA0012 case at $\pm 20^{\circ}$ and $\kappa = 3$	90
5–11	Fluid velocity contours and streamlines for the pitching NACA0012 case at $\pm 20^{\circ}$ and $\kappa = 3$ at time instances t_0, t_5 and t_{10}	92
5–12	Relative errors on the mean pressure coefficient $\overline{c_p}$ and the mean wall shear stress $\overline{\tau_w}$ for the pitching NACA0012 case at $\pm 20^{\circ}$ and $\kappa = 3$ at a time instance $t_5 = \frac{5}{11}T$	93

CHAPTER 1 Introduction

1.1 Context

Since the 1950s, rapid advances in computer science and its associated technologies have prompted engineers to develop and employ software in order to exploit the enormous calculation efficiency of computers. As problems of greater complexity could be tackled in a reasonable amount of time, novel disciplines focused on the development of numerical methods in various engineering fields emerged in the last several decades. Among them the Computational Fluid Dynamics (CFD) field aims to predict the behaviour of a fluid flow under predefined spatial boundary conditions and temporal initial conditions by using numerical methods to approximate the solution of the governing equations. In aerodynamics, the lack of analytical methods to exactly solve those equations for flows around smooth geometries such as two-dimensional airfoils motivated the development of CFD as a discipline. Today aircraft and turbomachinery manufacturers exploit CFD to optimize the design of their products and predict as precisely as possible the aerodynamic performances. The accuracy of the results provided by the CFD simulations enables engineers to explore multiple configurations.

However, despite the progress realized in numerical simulation and the increase of computing capacities in recent decades, the accurate computation of unsteady aerodynamic flows in a reasonable amount of time still presents a challenge in the field of computational fluid dynamics. Compared to steady flow problems which only require an accurate spatial discretization, unsteady flow solvers have to provide an accurate temporal resolution of the flow. The accurate computation of unsteady flows is essential for applications such as helicopter rotor design or rotor-stator interactions in turbomachinery.

1.2 Frequency domain solutions

Until recently, simulations of unsteady flows were performed through time marching techniques for which the solution is constructed in time from an initial freestream solution. One widely used approach is Jameson's dual time stepping technique [17] which is based on two nested loops. The outer loop is used to march the solution in physical (or real) time through a second-order backward difference scheme. Then at each physical time step the inner loop is used to march the solution to a steady state in pseudo time through a multistage Runge-Kutta scheme. The convergence of this technique is usually improved using local time-stepping and a multigrid strategy [16]. For periodic in time problems, the time step is advanced until a periodic steady state solution is resolved. In some instances if only the periodic solution is of interest, a large number of time steps or computational expense is required to shed the initial transient solutions.

In the specific case of time periodic flows encountered in problems such as aeroelastic analysis or turbomachinery, several new techniques have been developed over the last two decades to hasten the convergence of the numerical solvers. In such flows, any flow characteristic repeats itself every temporal period T, which makes it possible to exploit Fourier collocation techniques to accurately and efficiently represent the solution in physical time. The accuracy of the solution and the computational cost are then determined by the number of harmonics employed to model the periodic unsteadiness of the flow.

At first, periodic time-linearized techniques were introduced [11, 12], in which the flow is decomposed into a steady non-linear background flow and small periodic perturbations. Both steady and perturbed parts are advanced separately, where the steady part is solved using a conventional solver while a system of wave equations is employed to advance the perturbations. Despite the high computational efficiency of such an approach, it is unable to model non-linearities inherent to unsteady flow problems due to the decoupled nature of the solution strategy.

This motivated the development of completely non-linear techniques to capture the unsteadiness. The Harmonic Balance (HB) method initially introduced by Hall and al. [13] was the first of such an approach capable to capture the non-linearities of the flow. Then, McMullen and al. [24–26] developed the Non-Linear Frequency Domain (NLFD) method in order to solve the Euler and Navier-Stokes equations directly in the frequency domain contrary to Hall's method where equations were still solved in time. An alternative to this approach is the Time-Spectral (TS) method presented by Gopinath and al. [8, 9], which avoids the explicit use of a Discrete Fourier Transform (DFT) and discretizes the temporal derivative operator through a Fourier collocation matrix to solve the equation in time. Since these techniques directly converge to the periodic state solution, there is no initial transient effects to be computed which makes these methods computationally more efficient than time marching approaches for periodic flows. These methods were validated for both

Euler and Navier-Stokes equations through several unsteady periodic problems and proved to be successful in the capture of flow non-linearities as well as significantly decreased the required time to obtain the solution compared to time marching solvers [3, 8, 13, 25, 32].

Regardless of the approach, the expression of the residual as a function of the state vector is always non-linear and a pseudo-time stepping technique have to be employed to decrease the residual to negligible values. The convergence of the NLFD method originally solved using a Runge-Kutta multistage scheme in pseudo-time was later improved by employing the Lower-Upper Symmetric-Gauss-Seidel (LU-SGS) implicit scheme [4] or by taking into account the local level of unsteadiness of the flow through adapting the number of harmonics [28–31].

1.3 Mesh deformation and Geometric Conservation Law

Although the accurate computation of unsteady flows presents many difficulties, such simulations are essential during the aircraft design process and especially to evaluate the aeroelastic behaviour of aircraft components such as the wings, compressor and turbine blades. Aeroelasticity is the study of fluid-structure interactions between a body and a fluid flow. The accurate prediction of such behavior is critical to avoid structural failure. It can be decomposed into two analysis, the static (or steady) response of the body and its dynamic (unsteady) behavior such as vibrations. For instance, the flutter instability is a dynamic phenomenon which occurs when there is a positive feedback between the aerodynamic forces and the deflection of the structure. It produces a negative damping which leads either to self

oscillations or to diverging oscillations of the body which eventually would trigger structural failure.

Besides the complexity due to the unsteadiness of the flow, aeroelastic problems require by definition the motion of the body. To account for the movement of the boundaries, it becomes necessary to perform simulations on moving and potentially deforming grids. One popular approach for such problems is the formulation of the governing equations through an Arbitrary Lagrangian-Eulerian method [15, 35]. The approach requires the evaluation of the geometric quantities of the mesh such as vertices positions and velocities. In addition, in order to treat arbitrary body-fitted grids with complex geometry a mapping from the physical domain (x, y, z) to the computational space (ξ, η, ζ) is needed. Due to the motion of the coordinate system, additional care has to be taken to compute the mesh velocities and the mapping metrics. Thomas and al. [38] were the first to formally define the necessity to solve additional laws to preserve the conservation of the solver numerical scheme. Termed as the Geometric Conservation Law, it is composed of two subsets of laws known as the Surface Conservation Law (SCL) and the Volume Conservation Law (VCL). A mathematical interpretation of the SCL relates that any cell volume has to be closed by its surfaces whereas the VCL states that the temporal rate of change of the cell volume is equal to the sum of the temporal rate of change of the algebraic volumes swept by each face enclosing it through time. SCL differs from the VCL in the way that it needs to be verified even for fixed grids (steady state) while the VCL appears only on deforming grids.

The violation of any of these laws may result in errors in the flow solution, for instance it was reported that the violation of the GCL leads to inaccurate flutter prediction for aeroelastic cases [20]. Further investigation on time marching schemes clarified the theoretical status of the GCL, exposing its link to temporal-order accuracy [10], or stability conditions [7]. In addition, the Discrete Geometric Conservation Law (DGCL) were derived in order to preserve the temporal accuracy for first-order [33], second-order [19] and high temporal-order schemes [6, 22, 23]. These methods are well adapted for time marching approaches, but their extension to the NLFD or Time-Spectral methods is not straightforward since it becomes necessary to compute all quantities: state vector, fluxes, mesh positions and mesh velocities, at all time steps before applying the Fourier discretization. A popular approach to satisfy the GCL is to deduce the mesh velocities from the prior knowledge of the volumetric increments between successive time steps [22, 23, 43]. Following this idea, Tardif and al. [37] introduced a methodology to enforce the GCL in the NLFD framework.

1.4 Research objectives

The main objective is to develop methods to satisfy the Geometric Conservation Law in a three-dimensional finite volume framework with a temporal discretization following the Non-Linear Frequency Domain method presented by McMullen and al. [24]. In order to achieve this objective, the steps listed below were followed:

1. Investigate the approach from Tardif and al. [37] and demonstrate its limitations;

- Propose and develop new methods to enforce the GCL in a NLFD framework and demonstrate their impact on the convergence and accuracy, both analytically and numerically;
- 3. Evaluate and compare the impact of the developed methods on aerodynamic simulations.

The dissertation is organized through the following structure. In Chapter 2, the Navier-Stokes equations governing compressible viscous flows and their discretization in space and time are presented along with the dynamic mesh deformation technique using Radial Basis Functions (RBF). In Chapter 3, the Geometric Conservation Law is introduced and the developed methodologies are derived analytically. Numerical validation of the analytical results are presented in Chapter 4, and the impact on the aerodynamic coefficients of a cylinder and a NACA0012 airfoil for different motions is discussed in Chapter 5. Lastly conclusions, research contributions and future work are presented in Chapter 6.

CHAPTER 2 Flow solver framework

In this chapter, the characteristics of the flow solver employed to derive the different methodologies to enforce the Geometric Conservation Law are presented. Section 2.1 presents the formulation of the Navier-Stokes equations on a moving mesh using the Arbitrary Lagrangian-Eulerian approach while its spatial discretization on a hexahedral structured grid through a finite volume approach is introduced in Section 2.2 and its discretization in physical time using the Non-Linear Frequency Domain method is explained Section 2.3. The method employed for the dynamic mesh deformation through the Radial Basis Functions technique is developed Section 2.4.

2.1 Governing equations

When solving the Navier-Stokes equations on a moving grid a popular approach is to use an Arbitrary Lagrangian-Eulerian (ALE) formulation [2] which can be derived from the differential form of the conservation equations given without source terms by:

$$\frac{\partial \mathbf{w}}{\partial t} + \nabla \cdot [\mathbf{F_c}(\mathbf{w}) + \mathbf{F_v}(\mathbf{w}, \nabla \mathbf{w})] = 0, \tag{2.1}$$

where \mathbf{w} is the vector containing the conservative variables and often named the state vector or solution, $\nabla \mathbf{w}$ is the solution gradient, $\mathbf{F_c}(\mathbf{w})$ is the inviscid flux vector and $\mathbf{F_v}(\mathbf{w}, \nabla \mathbf{w})$ is the viscous flux vector.

For a control volume Ω enclosed by a boundary $\partial\Omega$ with the corresponding unit normal vector $\hat{\mathbf{n}}$ pointing outward, the integration of this differential form and the application of the divergence theorem yields:

$$\int_{\Omega} \frac{\partial \mathbf{w}}{\partial t} d\Omega + \oint_{\partial \Omega} \mathbf{F_c}(\mathbf{w}) \cdot \hat{\mathbf{n}} dS + \oint_{\partial \Omega} \mathbf{F_v}(\mathbf{w}, \nabla \mathbf{w}) \cdot \hat{\mathbf{n}} dS = 0.$$
 (2.2)

Then applying the Leibniz integral rule to the first term leads to:

$$\frac{\partial}{\partial t} \int_{\Omega} \mathbf{w} d\Omega + \oint_{\partial \Omega} (\mathbf{F_c}(\mathbf{w}) - \mathbf{w} \mathbf{V_t}) \cdot \hat{\mathbf{n}} dS + \oint_{\partial \Omega} \mathbf{F_v}(\mathbf{w}, \nabla \mathbf{w}) \cdot \hat{\mathbf{n}} dS = 0, \quad (2.3)$$

where $V_t = \frac{\partial x}{\partial t}$ is the contravariant velocity of the boundary enclosing the control volume.

This equation is known as the Arbitrary Lagrangian-Euleurian formulation of the Navier-Stokes equations and can be written as:

$$\frac{\partial}{\partial t} \int_{\Omega} \mathbf{w} d\Omega + \oint_{\partial \Omega} \mathbf{F}_{\mathbf{c}}^{\mathbf{M}}(\mathbf{w}) \cdot \hat{\mathbf{n}} dS + \oint_{\partial \Omega} \mathbf{F}_{\mathbf{v}}(\mathbf{w}, \nabla \mathbf{w}) \cdot \hat{\mathbf{n}} dS = 0, \tag{2.4}$$

where $\mathbf{F_c^M}(\mathbf{w}) = \mathbf{F_c}(\mathbf{w}) - \mathbf{wV_t}$ is the convective flux vector on a moving grid, if $\mathbf{V_t} = 0$ then it is equal to the original inviscid flux vector.

In three dimensions, the state vector \mathbf{w} , the vector of the convective fluxes on a moving grid $\mathbf{F}_{\mathbf{c}}^{\mathbf{M}}(\mathbf{w})$ and the viscous flux vector $\mathbf{F}_{\mathbf{v}}(\mathbf{w}, \nabla \mathbf{w})$ are expressed as follows

using Einstein notation with the index i = 1, 2, or 3:

$$\mathbf{w} = \begin{cases} \rho \\ \rho u_1 \\ \rho u_2 \\ \rho u_3 \\ \rho E \end{cases}; \mathbf{F_c^M(\mathbf{w})} = \begin{cases} \rho V \\ \rho u_1 V + n_1 p \\ \rho u_2 V + n_2 p \\ \rho u_3 V + n_3 p \\ \rho H V \end{cases} - \begin{cases} \rho V_t \\ \rho u_1 V_t \\ \rho u_2 V_t \\ \rho u_3 V_t \\ \rho E V_t \end{cases},$$
and
$$\mathbf{F_v(\mathbf{w}, \nabla \mathbf{w})} = \begin{cases} 0 \\ n_j \tau_{ij} \delta_{i1} \\ n_j \tau_{ij} \delta_{i2} \\ n_j \tau_{ij} \delta_{i3} \\ n_i (u_j \tau_{ij} + k \frac{\partial T_{emp}}{\partial x_i}) \end{cases} \text{ with the Kronecker symbol } \delta_{ij},$$

$$(2.5)$$

where ρ , u_1 , u_2 , u_3 , E, p, τ_{ij} , T_{emp} , k and H are respectively, the density, the Cartesian velocities of the fluid, the total energy per unit mass, the pressure, the components of the viscous stresses, the temperature, the thermal conductivity coefficient and the total enthalpy per unit mass defined by:

$$H = E + \frac{p}{\rho}. (2.6)$$

In order to close the system of equations, the pressure is evaluated under the assumption of ideal gas through the combination of the equation of state with the definition of total energy (2.7):

$$p = (\gamma - 1) \left(\rho E - \frac{(\rho u_1)^2 + (\rho u_2)^2 + (\rho u_3)^2}{2\rho} \right), \tag{2.7}$$

where γ is the heat capacity ratio.

Also, $\mathbf{V} = (u_1, u_2, u_3)$ is the contravariant velocity of the fluid, $\mathbf{V_t} = \left(\frac{\partial x_1}{\partial t}, \frac{\partial x_2}{\partial t}, \frac{\partial x_3}{\partial t}\right)$ is the contravariant velocity of the boundary enclosing the control volume and $\hat{\mathbf{n}} = (n_1, n_2, n_3)$ is the boundary unit normal vector pointing outward of the control volume. It yields:

$$\begin{cases} V = \mathbf{V} \cdot \hat{\mathbf{n}} = u_i n_i, \\ V_t = \mathbf{V_t} \cdot \hat{\mathbf{n}} = \frac{\partial x_i}{\partial t} n_i. \end{cases}$$
 (2.8)

By introducing a discretized control volume and an artificial dissipation flux vector $\mathbf{F_d}$ to avoid an odd-even decoupling of the solution and to increase the accuracy at discontinuities, equation (2.4) can be written under a semi-discretized non-dimensionalized form as:

$$\frac{\partial(\Omega \mathbf{w})}{\partial t} + \sum_{\partial \Omega} \left[\left(\mathbf{F}_{\mathbf{c}}^{\mathbf{M}} - \frac{\sqrt{\gamma} M_{\infty}}{R e_{\infty}} \mathbf{F}_{\mathbf{v}} \right) S - \mathbf{F}_{\mathbf{d}} \right] = 0. \tag{2.9}$$

The previous set of equations has to hold for each control volume and can be expressed as a semi-discrete system of ordinary differential equations in time:

$$\frac{\partial(\Omega \mathbf{w})}{\partial t} + \mathbf{R}(\mathbf{w}) = 0, \tag{2.10}$$

where
$$\mathbf{R}(\mathbf{w}) = \sum_{\partial\Omega} \left[\left(\mathbf{F}_{\mathbf{c}}^{\mathbf{M}} - \frac{\sqrt{\gamma} M_{\infty}}{Re_{\infty}} \mathbf{F}_{\mathbf{v}} \right) S - \mathbf{F}_{\mathbf{d}} \right]$$
 is the residual vector.

2.2 Spatial discretization

In this work, the discretization in space is performed employing a second-order finite volume method either on three-dimensional hexahedral grids or two-dimensional quadrilateral meshes. Given an arbitrary control volume, the state vector \mathbf{w} is evaluated at the cell centroid, while the residual vector $\mathbf{R}(\mathbf{w})$ is calculated through the summation of the fluxes over all the faces of the control volume. Using the indices i, j and k to denote the cell centroid, the discretized form of equation (2.10) can be written as such :

$$\begin{cases}
\frac{\partial (\Omega_{ijk} \mathbf{w}_{ijk})}{\partial t} + \mathbf{R}(\mathbf{w}_{ijk}) = 0, \\
\mathbf{R}(\mathbf{w}_{ijk}) = \sum_{m=1}^{N_f} \left[\left(\mathbf{F}_{\mathbf{c}}^{\mathbf{M}} - \frac{\sqrt{\gamma} M_{\infty}}{R e_{\infty}} \mathbf{F}_{\mathbf{v}m} \right) S_m - \mathbf{F}_{\mathbf{d}m} \right],
\end{cases} (2.11)$$

where m is the index of summation through the faces and N_f the number of faces enclosing the control volume.

The modified convective flux is computed as the average of the fluxes at a cell face and the artificial dissipation is evaluated using the Jameson-Schmidt-Turkel (JST) scheme [17]. The viscous flux is computed using a central second-order discretization. The residual vector is calculated as the summation over the faces of the control volume of the different fluxes.

2.3 Temporal discretization

The temporal discretization of the flow solver employs the NLFD approach developed by McMullen and al. [24]. Under the assumption that both the modified state vector $\bar{\mathbf{w}} = \Omega \mathbf{w}$ and the residual vector $\mathbf{R}(\mathbf{w})$ are periodic in physical time, the two quantities can be expanded as discrete Fourier series using a finite number of harmonics,

$$\bar{\mathbf{w}}(t) = \sum_{k=-N}^{N} \hat{\mathbf{w}}_k e^{i(2\pi k/T)t}, \qquad (2.12)$$

$$\mathbf{R}(\mathbf{w}(t)) = \sum_{k=-N}^{N} \hat{\mathbf{R}}_k e^{i(2\pi k/T)t}, \qquad (2.13)$$

where $i = \sqrt{-1}$ is the imaginary unit, T is the temporal period, k is the wave number, and N is the number of modes employed in the Discrete Fourier Transform (DFT). The k^{th} Fourier coefficients $\hat{\mathbf{w}}_k$ and $\hat{\mathbf{R}}_k$ are given by the following equations (2.14) and (2.15), for $-N \le k \le N$:

$$\hat{\mathbf{w}}_k = \frac{1}{2N+1} \sum_{n=0}^{2N} \Omega(t_n) \mathbf{w}(t_n) e^{-i(2\pi k/T)t_n},$$
(2.14)

$$\hat{\mathbf{R}}_k = \frac{1}{2N+1} \sum_{n=0}^{2N} \mathbf{R}(\mathbf{w}(t_n)) e^{-i(2\pi k/T)t_n},$$
(2.15)

where their computations require the sampling of the modified state vector and the residual vector for $N_{ts} = 2N + 1$ time steps at equally spaced time instances such that the n^{th} time sample t_n is:

$$t_n = \frac{n}{2N+1}T$$
, for $n = 0, ..., 2N$. (2.16)

At this point, it is important to emphasize that the state and residual vectors need to be evaluated at all time instances before transferring in the Fourier domain, this is a fundamental difference with the time marching approach. The Fourier representation is then substituted into the semi-discrete form of the Navier-Stokes equations (2.10) to yield:

$$\frac{\partial}{\partial t} \left(\sum_{k=-N}^{N} \hat{\mathbf{w}}_k e^{i(2\pi k/T)t} \right) + \sum_{k=-N}^{N} \hat{\mathbf{R}}_k e^{i(2\pi k/T)t} = 0, \tag{2.17}$$

$$\Leftrightarrow \sum_{k=-N}^{N} \frac{i2\pi k}{T} \hat{\mathbf{w}}_k e^{i(2\pi k/T)t} + \sum_{k=-N}^{N} \hat{\mathbf{R}}_k e^{i(2\pi k/T)t} = 0.$$
 (2.18)

By exploiting the orthogonality property of the Fourier basis, this leads to a set of 2N + 1 equations (2.19), each being associated to a wave number k:

$$i\frac{2\pi k}{T}\hat{\mathbf{w}}_k + \hat{\mathbf{R}}_k = 0 \text{ for } -N \le k \le N.$$
(2.19)

Since the representation of $\hat{\mathbf{R}}_k$ as a function of $\hat{\mathbf{w}}_k$ is not straightforward, an unsteady residual $\hat{\mathbf{R}}_k^*$ is defined and driven to zero using a pseudo-time marching approach such that:

$$\begin{cases}
\hat{\mathbf{R}}_{k}^{*} = i \frac{2\pi k}{T} \hat{\mathbf{w}}_{k} + \hat{\mathbf{R}}_{k} \\
, \text{ for } -N \leq k \leq N. \\
\frac{\partial \hat{\mathbf{w}}_{k}}{\partial t^{*}} + \hat{\mathbf{R}}_{k}^{*} = 0
\end{cases} (2.20)$$

Thus at convergence, $\hat{\mathbf{R}}_k^* = 0$ and equation (2.20) is satisfied for each wave number.

The new periodic solution is then transferred back to the physical time domain using an Inverse Fourier Discrete Transform (IDFT) and evaluated at each time instance t_n by dividing by the volume :

$$\mathbf{w}(t_n) = \frac{\bar{\mathbf{w}}(t_n)}{\Omega(t_n)}, \text{ for } 0 \le n \le 2N.$$
(2.21)

The equation in pseudo-time can be solved using any time-stepping scheme. In this work, we use a hybrid five-stage Runge-Kutta scheme with blending coefficients for the artificial dissipation [16].

2.4 Dynamic mesh deformation

The deformation of the mesh is performed using the Radial Basis Functions (RBF) [37]. The method is based on the assumption that the movement of all grid

points can be interpolated from an *a priori* known motion of a set of points called the RBF points. In this study, the RBF points are always a subset of the grid points at the boundary of the domain, their displacements relative to the undeformed mesh are prescribed at each time instance using analytical functions. Because of the NLFD method, the mesh positions and velocities are therefore computed and stored for all N_{ts} time steps. For any grid point v_j of position vector \mathbf{x}_{v_j} in the undeformed mesh, its displacement in the x-direction $s_x(\mathbf{x}_{v_j}, t)$ is defined as:

$$s_x(\mathbf{x}_{v_j}, t) = \sum_{i=1}^{N_{RBF}} \alpha_i(t)\phi(||\mathbf{x}_{v_j} - \mathbf{x}_{r_i}||_2), \qquad (2.22)$$

where N_{RBF} is the number of RBF points, α_i are the interpolation coefficients, \mathbf{x}_{r_i} is the position vector of the i^{th} RBF point in the undeformed grid and ϕ is some basis function depending on the Euclidean distance $||\mathbf{x}_{v_j} - \mathbf{x}_{r_i}||_2$ between the points v_j and r_i . In this work, Wendland C0's basis function [39] is considered, it is defined as follows:

$$\begin{cases} (1-l)^2 & \text{if } l < 1\\ 0 & \text{if } l \ge 1 \end{cases}, \text{ with } l = \frac{||\mathbf{x}_{v_j} - \mathbf{x}_{r_i}||_2}{R}, \tag{2.23}$$

where R is the support radius relative to the surface of RBF points. Since the equation (2.22) holds for any grid point whether it is a RBF point or a standard grid point, the RBF points are denoted with the subscript r while the grid (or volume) points are denoted with the subscript v. Then in the x-direction, the displacements of all RBF points and the interpolated displacements of all grid points are regrouped respectively in the vector $\Delta \mathbf{x}_r$ and in the vector $\Delta \mathbf{x}_v$. Therefore the a priori unknown

displacements $\Delta \mathbf{x}_v$ are obtained through equation (2.24):

$$\Delta \mathbf{x}_v = \mathcal{A}(\mathcal{M}^{-1})\Delta \mathbf{x}_r,\tag{2.24}$$

where:

$$\mathcal{M} = \begin{pmatrix} \phi_{r_{1}r_{1}} & \phi_{r_{1}r_{2}} & \dots & \phi_{r_{1}r_{N_{RBF}}} \\ \phi_{r_{2}r_{1}} & \ddots & & \vdots \\ \vdots & & & & & \vdots \\ \phi_{r_{N_{RBF}}r_{1}} & \dots & \phi_{r_{N_{RBF}}r_{N_{RBF}}} \end{pmatrix}, \mathcal{A} = \begin{pmatrix} \phi_{v_{1}r_{1}} & \phi_{v_{1}r_{2}} & \dots & \phi_{v_{1}r_{N_{RBF}}} \\ \phi_{v_{2}r_{1}} & \ddots & & \vdots \\ \vdots & & & & & \vdots \\ \phi_{v_{N_{grid}}r_{1}} & \dots & \phi_{v_{N_{grid}}r_{N_{RBF}}} \end{pmatrix},$$

$$(2.25)$$

with:

$$\phi_{v_i r_i} = \phi\left(||\mathbf{x}_{v_i} - \mathbf{x}_{r_i}||_2\right),\tag{2.26}$$

and N_{grid} is the total number of grid points. The displacements in the y and z directions can be computed with the same matrices given in equation (2.25), by considering the RBF points displacements in the corresponding direction.

Similarly, the mesh velocities for any grid point are computed using the Radial Basis Functions for Velocities (RBFV) by interpolating the *a priori* known velocities of the RBF points which leads to the following expression:

$$\mathbf{v}_{v,dir} = \mathcal{A}(\mathcal{M}^{-1})\mathbf{v}_{r,dir},\tag{2.27}$$

where $\mathbf{v}_{v,dir}$ is the vector of the velocities of the grid points and $\mathbf{v}_{r,dir}$ is the vector of the velocities of the RBF points and the direction is given by dir = x, y, or z.

CHAPTER 3

Derivation and enforcement of the Geometric Conservation Law

As previously stated our interest is focused on the Volume Conservation Law aspect of the GCL. Under integral form the VCL for a control volume Ω enclosed by a boundary $\partial\Omega$ can be written as follows:

$$\frac{\partial}{\partial t} \int_{\Omega} d\Omega - \oint_{\partial \Omega} (\mathbf{V_t} \cdot \hat{\mathbf{n}}) dS = 0.$$
 (3.1)

where V_t is the mesh velocity vector and $\hat{\mathbf{n}}$ is the unit normal vector to the surface $\partial\Omega$ pointing outward. The law relates only on geometrical considerations and is always satisfied under continuous form and implicitly satisfied for rigid grid motion. It arises from the deformation of the mesh and is closely related to the preservation of uniform flow by the numerical scheme. Therefore in order to obtain a consistent solution method, the GCL must be discretized using the same numerical scheme employed to discretize the primary conservation laws [10]. In our case, it yields a hexahedral stuctured finite-volume framework and a temporal discretization using the NLFD method.

A first approach to enforce the VCL in the NLFD context was presented by Tardif and al. [37] but more investigation is needed to determine its limitations. In this chapter, further developments are added to this approach in Section 3.2 which expose its analytical limits and new methods are proposed in Sections 3.3 and 3.4.

3.1 Derivation of the GCL in the NLFD framework

Considering any discretized control volume Ω enclosed by N_f faces, then equation (3.1) can be written as:

$$\frac{\partial \Omega}{\partial t} - \sum_{m=1}^{N_f} \iint_{\partial \Omega_m} (\mathbf{V_t} \cdot \hat{\mathbf{n}}_m) dS = 0, \tag{3.2}$$

where $\hat{\mathbf{n}}_m$ is the unit normal vector to the face $\partial \Omega_m$ pointing outward. Then the integrated face mesh velocities (IFMV) $G_m(t)$ corresponding to the temporal rate of change of the algebraic volume swept by each face through time are introduced in equation (3.3):

$$G_m(t) = \iint_{\partial\Omega_m} (\mathbf{V_t} \cdot \hat{\mathbf{n}}_m) dS, \tag{3.3}$$

and also G(t) is the sum of the IFMV over all faces of the control volume:

$$G(t) = \sum_{m=1}^{N_f} G_m(t). \tag{3.4}$$

Then equation (3.2) can be written as:

$$\frac{\partial\Omega}{\partial t} - G(t) = 0. {(3.5)}$$

Under the assumption that the volume Ω and the sum of the integrated face mesh velocities G are periodic functions of time, the NLFD discretization can be applied:

$$\Omega(t) = \sum_{k=-N}^{N} \hat{\Omega}_k e^{i(2\pi k/T)t}, \qquad (3.6)$$

$$G(t) = \sum_{k=-N}^{N} \hat{G}_k e^{i(2\pi k/T)t}.$$
 (3.7)

By substituting these expressions into equation (3.5), it yields:

$$\frac{\partial}{\partial t} \left(\sum_{k=-N}^{N} \hat{\Omega}_k e^{i(2\pi k/T)t} \right) - \sum_{k=-N}^{N} \hat{G}_k e^{i(2\pi k/T)t} = 0$$
 (3.8)

$$\Leftrightarrow \left(\sum_{k=-N}^{N} \frac{i2\pi k}{T} \hat{\Omega}_k e^{i(2\pi k/T)t}\right) - \sum_{k=-N}^{N} \hat{G}_k e^{i(2\pi k/T)t} = 0.$$
 (3.9)

Then by exploiting the orthogonality property of the Fourier basis, it leads to a system of 2N + 1 equations, each corresponding to a wave number k:

$$\frac{i2\pi k}{T}\hat{\Omega}_k = \hat{G}_k \text{ for } -N \le k \le N.$$
 (3.10)

The set of equations (3.10) provides the necessary condition to enforce the GCL in the NLFD approach. Such criterion is not satisfied in general and has to be enforced through the correct computation of the cell volume and the integrated face mesh velocities, in a way consistent with the solver numerical scheme. Since the volume is usually exactly known, one popular approach in time marching methods is to split the GCL over each face [22, 23, 43]. In the current framework, the volume of a cell can be expressed as the sum of the volume at a reference initial instant t_0 and the algebraic (positive or negative) volumetric increments due to each face Ω_m relative to this reference instant:

$$\Omega(t) = \Omega(t_0) + \sum_{m=1}^{N_f} \Omega_m(t). \tag{3.11}$$

By substituting relations (3.11) and (3.4) into the equation (3.5), it yields:

$$\sum_{m=1}^{N_f} \left(\frac{\partial \Omega_m}{\partial t} - G_m(t) \right) = 0.$$
 (3.12)

Then for each face m enclosing the discretized control volume, we need to ensure the relation (3.13):

$$\frac{\partial \Omega_m}{\partial t} = G_m(t). \tag{3.13}$$

However, even if the positions of the mesh vertices and their velocities are known at all time instances from the dynamic mesh deformation, the implementation of the GCL using this relation is not straightforward using the NLFD method. In the following, volumetric increments are always considered as algebraic values which can either be positive or negative.

3.2 Approach of Tardif and al. [37]

The first approach developed by Tardif and al. [37] is based on a linear representation of the volumetric increments relative to a reference time instance t_0 . For any face m defined by its vertices the induced volumetric change would simply be represented by drawing straight lines from their initial position at t_0 to their position at time instant t, see Figure 3–1.

This approach has two advantages: first, it is easy to compute the volumetric increments at each time instant using standard cell volume computational algorithms; second, the volumetric increments due to each face are time periodic as long as the movement of the vertices is periodic.

Once the volumetric increments are known for 2N + 1 time instances defined by equation (2.16), their Fourier representations are calculated:

$$\Omega_m(t) = \sum_{k=-N}^{N} \hat{\Omega}_{m,k} e^{(i2\pi k/T)t}, \qquad (3.14)$$

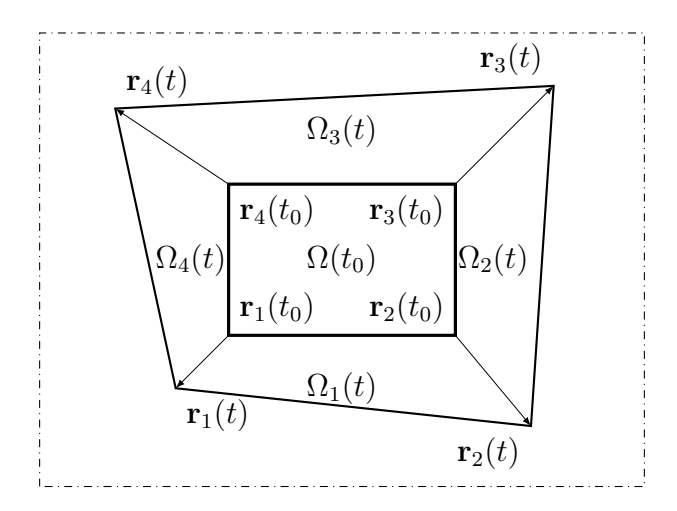


Figure 3–1: Example of linear volumetric increment in 2D relatively to a reference time instant t_0

and the Fourier formulations of the integrated face mesh velocities for each face m are introduced:

$$G_m(t) = \sum_{k=-N}^{N} \hat{G}_{m,k} e^{(i2\pi k/T)t}.$$
 (3.15)

Then by substituting, the Fourier representations into criteria (3.13), and exploiting the orthogonality of the Fourier basis, a system of 2N + 1 equations (3.16) is obtained for each face m:

$$\frac{i2\pi k}{T}\hat{\Omega}_{m,k} = \hat{G}_{m,k} \text{ for } -N \le k \le N.$$
(3.16)

Therefore, the GCL are satisfied independently for each face of the control volume by computing the Fourier coefficients $\hat{G}_{m,k}$ and then applying an IDFT to transfer back the integrated face mesh velocities to the temporal domain. Despite its attractiveness, this method is restricted to linear movements due to the manner in which the volumetric increments are computed. In general, the motion would not be linear and such representation of the volumetric increments will not be sufficient to ensure the correct computation of the IFMV.

Moreover the NLFD method is based on the assumption that the quantities are time periodic and can be expanded in Fourier series, but having a time periodic movement of the vertices does not guarantee time periodic volumetric increments but only that their temporal derivative will be periodic. This statement will be demonstrated through the following example.

A 2D quadrilateral element is considered with the following motion defined by equation (3.17) and shown Figure 3–2:

$$\begin{cases}
\alpha(t) = 2\pi t, \\
\mathbf{r_1} = \mathbf{r_{1,0}}, \\
\mathbf{r_2} = \mathbf{r_{2,0}}, \\
\mathbf{r_3} = \mathbf{r_{3,0}} + R(1 - \cos(\alpha(t)))\mathbf{e_x} + R(\sin(\alpha(t)))\mathbf{e_y}, \\
\mathbf{r_4} = \mathbf{r_{4,0}},
\end{cases} (3.17)$$

where the index 0 refers to the initial position of the grid, R is the radius defining the amplitude of the circular motion and $\mathbf{e_x}$ and $\mathbf{e_y}$ are the unit vectors in respectively the x and y directions.

For the face defined by the vertices \mathbf{r}_2 and \mathbf{r}_3 , the derivation of the expression of the exact volumetric increment in the x direction and its time derivative leads to the following expressions respectively (3.18) and (3.19):

$$\Omega_{23,x}(t) = \frac{R^2}{2} (\alpha(t) - \sin(\alpha(t))) + \frac{Ry_{3,0}}{2} (1 - \cos(\alpha(t))), \tag{3.18}$$

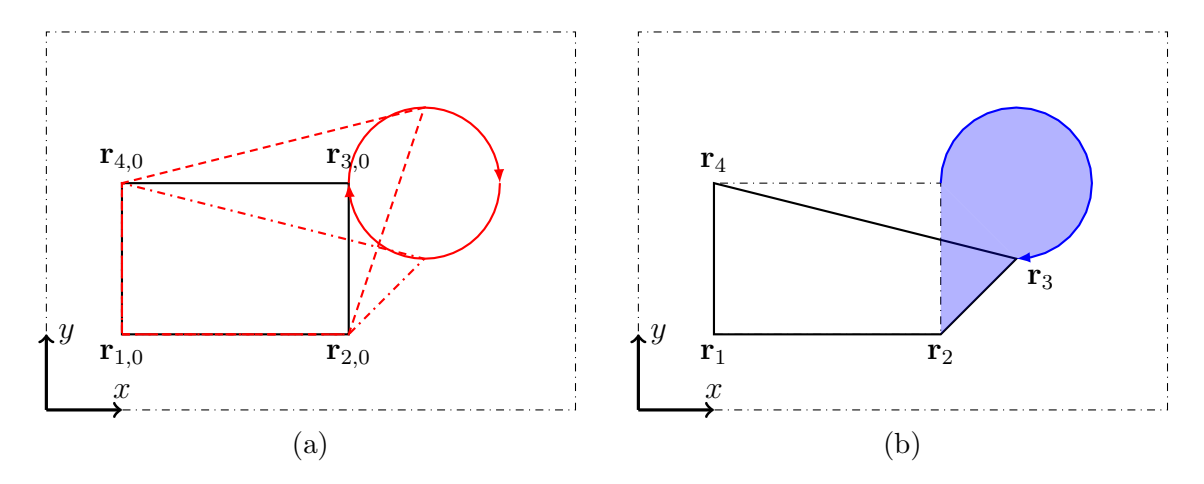


Figure 3–2: (a) The initial undeformed quadrilateral element is shown in black while the movement of the mesh points is presented in red with two deformed configurations of the cell in dashed lines, (b) Exact volumetric increment for the face 2-3 in the x direction relatively to the initial configuration (in dash dot line) in blue

$$\frac{\partial \Omega_{23,x}(t)}{\partial t} = \frac{R^2}{2} \frac{\partial \alpha}{\partial t} (1 - \cos(\alpha(t))) + \frac{Ry_{3,0}}{2} \frac{\partial \alpha}{\partial t} \sin(\alpha(t)), \tag{3.19}$$

where the length $y_{3,0} = (\mathbf{r}_{3,0} \cdot \mathbf{e}_{\mathbf{y}})$.

Thus the temporal derivative of the volumetric increment is periodic whereas the volumetric increment is the sum of a linear term and a periodic term and the direct application of the NLFD method on the exact volumetric increment is not possible since the linear term is not expandable as a Fourier serie. Additional work is required to ensure equation (3.13) is compliant with the NLFD method.

3.3 New method based on the exact volumetric increments

In this section, first a new methodology which relies on the exact volumetric increments is introduced analytically in Section 3.3.1. Then, the accuracy due to the numerical discretization of the method on hexahedral grids is derived in Section 3.3.2 and then extended to quadrilateral grids in Section 3.3.3.

3.3.1 Method

In this section, we introduce and demonstrate the new Theorem 3.3.1,

Theorem 3.3.1. Let Ω be a discretized control volume, enclosed by N_f faces, and subjected to a periodic motion of its vertices. Then given the knowledge of the exact volumetric increments Ω_m for $m = 1, ..., N_f$, a sufficient condition to ensure the satisfaction of GCL in the NLFD framework is the computation of the integrated face mesh velocities, where the zeroth and higher modes can be expressed as

$$\hat{G}_{m,0} = \frac{\Omega_m(T)}{T},\tag{3.20}$$

$$\hat{G}_{m,k} = \frac{i2\pi k}{T}\hat{p}_{m,k} \text{ for } -N \le k \le N, \ k \ne 0,$$
 (3.21)

where $\hat{G}_{m,k}$ and $\hat{p}_{m,k}$ are the Fourier coefficients of respectively the integrated face mesh velocities and the periodic parts of the exact volumetric increments given by,

$$p_m(t) = \Omega_m(t) - \left(\frac{\Omega_m(T)}{T}\right)t. \tag{3.22}$$

Proof. Under the assumption that the motion of the vertices is periodic, the temporal rate of change of the algebraic volume swept by each face through time is periodic. Thus the temporal derivatives of the volumetric increments and the integrated face mesh velocities are periodic, the DFT is applied to the equation (3.13) leading to:

$$G_m(t) = \frac{\partial \Omega_m}{\partial t} = \hat{G}_{m,0} + \sum_{k=-N, k\neq 0}^{N} \hat{G}_{m,k} e^{i\frac{2\pi}{T}kt}, \qquad (3.23)$$

where $\hat{G}_{m,k}$, for $-N \leq k \leq N$ are the Fourier coefficients of both the temporal derivative of the volumetric increment and the integrated face mesh velocity of a face m.

By integrating the equation in time, any volumetric increment is expressed as:

$$\Omega_m(t) = \int \frac{\partial \Omega_m}{\partial t} dt = \hat{\Omega}_{m,0} + \hat{G}_{m,0}t + \sum_{k=-N, k \neq 0}^{N} \frac{T}{i2\pi k} \hat{G}_{m,k} e^{i\frac{2\pi}{T}kt}.$$
 (3.24)

where $\hat{\Omega}_{m,0}$ is a constant of integration. Then any volumetric increment can be interpreted as the sum of a linear term $l_m(t)$ and a periodic function $p_m(t)$ defined by:

$$l_m(t) = \hat{G}_{m,0}t, (3.25)$$

$$p_m(t) = \hat{\Omega}_{m,0} + \sum_{k=-N,k\neq 0}^{N} \frac{T}{i2\pi k} \hat{G}_{m,k} e^{i\frac{2\pi}{T}kt}.$$
 (3.26)

Knowing the values of the volumetric increments at $t = t_0$ and $t = t_0 + T$, and exploiting the periodicity of the functions p_m , yields:

$$\Omega_{m}(t_{0}) = \hat{G}_{m0}t_{0} + p_{m}(t_{0})$$

$$\Omega_{m}(t_{0} + T) = \hat{G}_{m0}(t_{0} + T) + p_{m}(t_{0} + T)$$

$$p_{m}(t_{0}) = p_{m}(t_{0} + T)$$

$$\hat{G}_{m,0} = \frac{\Omega_{m}(t_{0} + T) - \Omega_{m}(t_{0})}{T}$$
(3.27)

Hence the zeroth Fourier coefficients of the integrated face mesh velocities are known through equation (3.27) applied for each face m and the linear parts l_m of the volumetric increments can be computed at each instant. Then, an expression of the

periodic part of any volumetric increment p_m is obtained as:

$$p_m(t) = \Omega_m(t) - l_m(t) = \Omega_m(t) - \left(\frac{\Omega_m(t_0 + T) - \Omega_m(t_0)}{T}\right)t.$$
 (3.28)

Usually t_0 would be taken as the initial time instant $t_0 = 0$ corresponding to the undeformed configuration of the mesh, for this specific reference time instant $\Omega_m(0) = 0$, and the previous expression can be further simplified into equation (3.29):

$$p_m(t) = \Omega_m(t) - \left(\frac{\Omega_m(T)}{T}\right)t. \tag{3.29}$$

Therefore, at each instant t the periodic parts of the volumetric increments p_m are known and for each face m we introduce the Fourier coefficients for p_m , noted as $\hat{p}_{m,k}$ for $-N \leq k \leq N$. By calculating the temporal derivative in Fourier space of p_m and exploiting the orthogonality of the Fourier basis functions, the rest of the Fourier coefficients of the integrated face mesh velocities $\hat{G}_{m,k}$ are deduced for each face m from a system of 2N equations

$$\hat{G}_{m,k} = \frac{i2\pi k}{T}\hat{p}_{m,k} \text{ for } -N \le k \le N, \ k \ne 0.$$
 (3.30)

Since the derivation in Fourier space puts to zero the contribution from the zeroth coefficient, the values of the integration constants $\hat{\Omega}_{m,0}$ are not relevant to compute the integrated face mesh velocities.

Finally the procedure to compute the IFMV to enforce GCL by deducing the temporal derivative of the volumetric increment for each face is given by the pseudocode (Algorithm 1). It is important to note that since the values of the volumetric

```
for n = 0, ..., 2N do
    Calculate the mesh deformation using the RBF for equally space time
     instances t_n;
end
for face = 1, ..., face_{max} do
    for n = 0, ..., 2N + 1 do
        Calculate the volumetric increments \Omega_{face}(t_n);
    end
    Deduce the zeroth Fourier coefficient via \hat{G}_{face,0} = \frac{\Omega_{face}(t_{2N+1})}{T};
    for n = 0, ..., 2N do
        Extract the periodic part of the volumetric increment via
         p_{face}(t_n) = \Omega_{face}(t_n) - \hat{G}_{face,0}t_n ;
    end
    Compute the Fourier coefficients \hat{p}_{face,k} via FFT on p_{face}(t);
    for k = -N, ..., 1 and k = 1, ...N do
        Deduce the k^{th} Fourier coefficient of the integrated face mesh velocity
         via \hat{G}_{face,k} = \frac{i2\pi k}{T} \hat{p}_{face,k};
    end
    Compute the integrated face mesh velocity G_{face}(t) via IFFT on \hat{G}_{face,k}
     with -N \le k \le N;
end
```

Algorithm 1: Pseudo-code representing the derived procedure to compute the integrated face mesh velocities and ensure GCL in the NLFD framework

increments are required at t = T in order to deduce the zeroth Fourier coefficients $\hat{G}_{m,0}$ through equation (3.20), one additional time step is needed t_{2N+1} compared to the number of time steps for the flow solver. However for this final time step the configuration of the mesh is the same as the initial (the undeformed mesh), thus no additional time step is needed for the mesh deformation. For this procedure, the key point is to compute the exact volumetric increments as accurately as possible in order to preserve the spectral convergence of the NLFD method.

3.3.2 Practical enforcement and error estimation on hexahedral grids

In practice the accuracy of the previous method highly depends on the accuracy of the computation of the volumetric increments. For a hexahedral grid, as each face m sweeps through the computational domain, between time intervals they form 8-vertex cells with 12 straight line segment edges but 6 faces which may no longer be planar depending on the mesh deformation; thus these 8-vertex cells may not form hexahedra. However 8-vertex cells with 12 straight line segment edges are topologically equivalent to hexahedra independent of the planarity of the faces [5] and sometimes termed as "general hexahedra" [44]. The surfaces of any "general hexahedron" can be defined using a trilinear mapping [5] between the 8-vertex cells in physical space with 12 straight line segment edges for either planar or non planar faces and a reference cube in the computational domain Figure 3–3. Thanks to this mapping which depends only on the vertices positions and the numeration convention, the volume of any of these general hexahedra can be computed. This yields the following Definitions 3.3.2, 3.3.3 and 3.3.4.

Definition 3.3.2. The terminology general hexahedron is employed to design a 8-vertex cell with 12 straight line segment edges for either planar or non planar faces which is topologically equivalent to a hexahedron.

Definition 3.3.3. The volume of any "general hexahedron" (Definition 3.3.2) as a function of the position vectors of the vertices in the physical space \mathbf{r}_i for i = 1, ..., 8, is evaluated through,

$$\begin{cases}
\Omega_h = (\Omega_{4321} + \Omega_{5678} + \Omega_{3487} + \Omega_{1265} + \Omega_{4158} + \Omega_{2376}), \\
with \Omega_{ijkl} = \frac{1}{12} (\mathbf{r}_j + \mathbf{r}_k) \cdot ((\mathbf{r}_i + \mathbf{r}_j) \times (\mathbf{r}_i + \mathbf{r}_l)).
\end{cases}$$
(3.31)

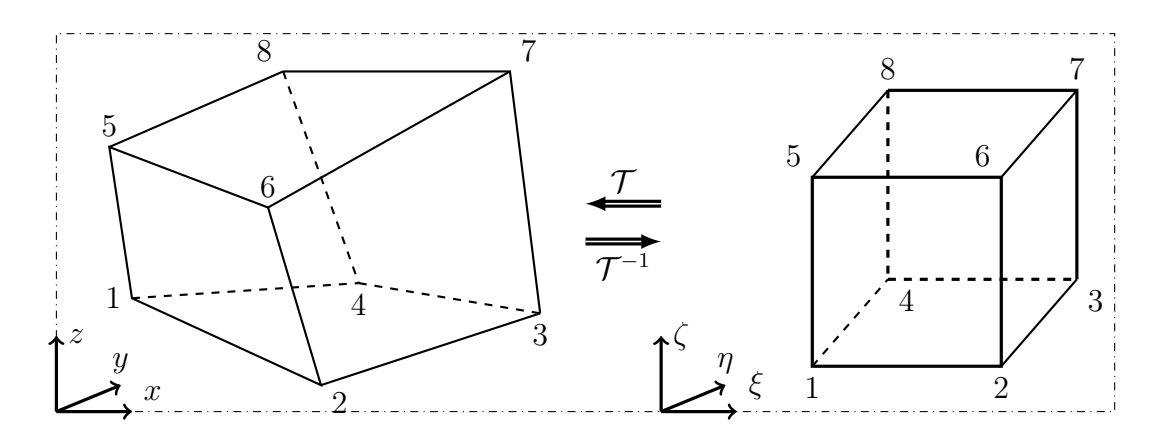


Figure 3–3: Trilinear mapping between a "general hexahedron" (Definition 3.3.2) in the physical space and a reference cube in the computational domain

Definition 3.3.4. For any face m of a hexahedral cell, the exact volumetric increment is estimated through a sum of "general hexahedra" (Definition 3.3.2) each corresponding to the approximated volumetric increment between two time samples

 t_{n-1} and t_n and noted as $\Omega_{m,h}(t_n)$, (see Figure 3-4):

$$\begin{cases}
\Omega_m(t_0) = 0, \\
\Omega_m(t_n) = \left(\sum_{k=1}^n \Omega_{m,h}(t_k)\right) + \epsilon_m^T(t_n), \text{ for } 1 \le n \le 2N + 1,
\end{cases}$$
(3.32)

where $t_0 = 0$ is the initial instant corresponding to the undeformed mesh and $\epsilon_m^T(t_n)$ is the truncation error at time instant t_n .

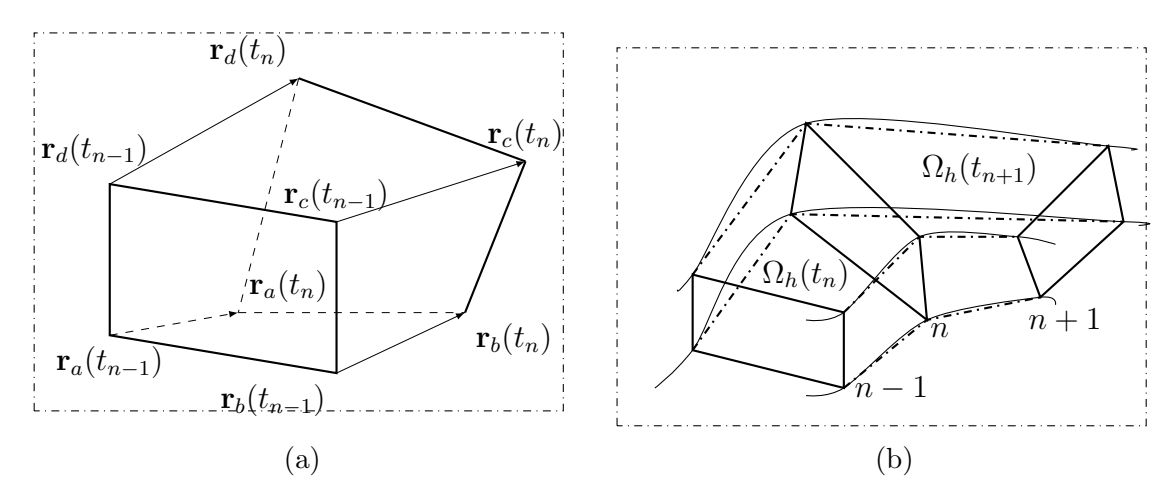


Figure 3–4: (a) Approximated volumetric increment between two time steps t_{n-1} and $t_n : \Omega_h(t_n)$ (b) Approximation of a volumetric increment as a sum of "general hexahedra" (Definition 3.3.2)

Now that the mathematical tools to compute the volumetric increments are introduced, the accuracy of the procedure presented in Section 3.3.1 can be established, we have the first Lemma 3.3.5,

Lemma 3.3.5. In the context of Theorem 3.3.1, and under the Definitions 3.3.2, 3.3.3 and 3.3.4, for any face m the temporal-order of accuracy of the zeroth Fourier coefficient of the integrated face mesh velocity $\hat{G}_{m,0}$ is limited to one.

Proof. We introduce the scalar triple product application \mathcal{L} defined by,

$$\mathcal{L} = \begin{cases} \mathbb{R}^3 \times \mathbb{R}^3 \times \mathbb{R}^3 & \to \mathbb{R} \\ (\mathbf{V_1}, \mathbf{V_2}, \mathbf{V_3}) & \to \mathbf{V_1} \cdot (\mathbf{V_2} \times \mathbf{V_3}) = \det(\mathbf{V_1}, \mathbf{V_2}, \mathbf{V_3}) \end{cases}$$
(3.33)

due to the properties of the determinant this application is a 3-linear alternating form meaning that if any of the three vector is a linear combination of the two others the result is zero.

Recalling that the volume of any "general hexahedron" (Definition 3.3.2) is computed as a function of the position vectors of the vertices in the physical space \mathbf{r}_i for i = 1, ..., 8 through the following equation (see Definition 3.3.3):

$$\begin{cases}
\Omega_{h} = (\Omega_{4321} + \Omega_{5678} + \Omega_{3487} + \Omega_{1265} + \Omega_{4158} + \Omega_{2376}), \\
\text{with } \Omega_{ijkl} = \frac{1}{12} \mathcal{L}(\mathbf{r}_{j} + \mathbf{r}_{k}, \mathbf{r}_{i} + \mathbf{r}_{j}, \mathbf{r}_{i} + \mathbf{r}_{l}).
\end{cases} (3.34)$$

For each face m the path of the four corresponding vertices between two time steps is linearly approximated, as shown in Figure 3–4. Then, for any of these vertices \mathbf{r}_i , i=a,b,c,d at the n^{th} time sample, we have the Taylor expansion :

$$\mathbf{r}_{i}(t_{n}) = \mathbf{r}_{i}(t_{n-1}) + \left(\frac{\partial \mathbf{r}_{i}}{\partial t}(t_{n-1})\right)(t_{n} - t_{n-1}) + \underbrace{\frac{1}{2}\left(\frac{\partial^{2} \mathbf{r}_{i}}{\partial t^{2}}(t_{n-1})\right)(t_{n} - t_{n-1})^{2} + \mathcal{O}((t_{n} - t_{n-1})^{3})}_{\text{Truncation error on the vertex path}}.$$

$$(3.35)$$

The volumetric increment is then defined by the vertices positions with the following indexation,

$$\begin{cases}
\mathbf{r}_{1} = \mathbf{r}_{a}(t_{n-1}), & \mathbf{r}_{2} = \mathbf{r}_{b}(t_{n-1}), & \mathbf{r}_{3} = \mathbf{r}_{c}(t_{n-1}), & \mathbf{r}_{4} = \mathbf{r}_{d}(t_{n-1}), \\
\mathbf{r}_{5} = \mathbf{r}_{a}(t_{n}), & \mathbf{r}_{6} = \mathbf{r}_{b}(t_{n}), & \mathbf{r}_{7} = \mathbf{r}_{c}(t_{n}), & \mathbf{r}_{8} = \mathbf{r}_{d}(t_{n}).
\end{cases} (3.36)$$

By substituting the Taylor expansions into the vertices positions to compute the volume of the volumetric increment through equation (3.34), and then by exploiting the 3-linearity of the triple product application, the order of the truncation error is evaluated. The lowest order terms of the truncation error are given by one of the following generic forms:

$$\mathcal{L}(\mathbf{r}_i(t_{n-1}), \mathbf{r}_j(t_{n-1}), \boldsymbol{\epsilon}_k(t_n)) = \left\{ \mathbf{r}_i(t_{n-1}) \cdot \left[\mathbf{r}_j(t_{n-1}) \times \frac{1}{2} \left(\frac{\partial^2 \mathbf{r}_k}{\partial t^2}(t_{n-1}) \right) \right] \right\} \tau^2 + \mathcal{O}(\tau^3),$$

$$\mathcal{L}(\mathbf{r}_i(t_{n-1}), \boldsymbol{\epsilon}_j(t_n), \mathbf{r}_k(t_{n-1})) = \left\{ \mathbf{r}_i(t_{n-1}) \cdot \left[\frac{1}{2} \left(\frac{\partial^2 \mathbf{r}_j}{\partial t^2}(t_{n-1}) \right) \times \mathbf{r}_k(t_{n-1}) \right] \right\} \tau^2 + \mathcal{O}(\tau^3),$$

$$\mathcal{L}(\boldsymbol{\epsilon}_{i}(t_{n}), \mathbf{r}_{j}(t_{n-1}), \mathbf{r}_{k}(t_{n-1})) = \left\{ \frac{1}{2} \left(\frac{\partial^{2} \mathbf{r}_{i}}{\partial t^{2}}(t_{n-1}) \right) \cdot \left[\mathbf{r}_{j}(t_{n-1}) \times \mathbf{r}_{k}(t_{n-1}) \right] \right\} \tau^{2} + \mathcal{O}(\tau^{3}).$$
(3.37)

where i, j and k are the vertices indices. Therefore for any face m, the truncation error $\epsilon_{m,h}^T$ on the volumetric increment between two time steps t_{n-1} and t_n is of order two in $\tau = (t_n - t_{n-1})$. In addition, it is possible to write the lowest order term of the error as a linear combination of the previous forms equation (3.37), thus there exists a scalar function \mathcal{E}_m^T depending on the vertices paths \mathbf{r}_i and their second temporal

derivatives $\frac{\partial^2 \mathbf{r}_i}{\partial t^2}$ such that,

$$\epsilon_{m,h}^{T}(t_n) = \mathcal{E}_m^{T}(t_{n-1})\tau^2 + \mathcal{O}(\tau^3).$$
 (3.38)

Due to the temporal periodicity of the vertices paths \mathbf{r}_i , the function \mathcal{E}_m^T is also periodic. Recalling that the number of time steps $N_{ts} = 2N + 1$ and using the definition of the time instance, the difference $(t_n - t_{n-1})$ is written as

$$\tau = \frac{[n - (n-1)]T}{2N+1} = \frac{T}{N_{ts}}.$$
(3.39)

Thus the truncation error during the estimation of the volumetric increment between two time steps at the n^{th} instant and noted $\epsilon_{m,h}^T(t_n)$ is of order two in τ and can be expanded as:

$$\begin{cases}
\epsilon_{m,h}^{T}(t_0) = 0, \\
\epsilon_{m,h}^{T}(t_n) = \mathcal{E}_m^{T}(t_{n-1})\tau^2 + \mathcal{O}(\tau^3), \text{ for } 1 \le n \le 2N + 1,
\end{cases}$$
(3.40)

where $\mathcal{E}_m^T(t)$ is a scalar periodic function depending on $\mathbf{r}_i(t)$, and $\frac{\partial^2 \mathbf{r_i}}{\partial t^2}$, for i = a, b, c, d.

In order to estimate the error committed on the exact volumetric increment approximated at the n^{th} time sample, these errors have to be summed, and yields:

$$\begin{cases} \epsilon_m^T(t_0) = 0, \\ \epsilon_m^T(t_n) = \sum_{k=1}^n \epsilon_{m,h}^T(t_k) = \left(\sum_{k=1}^n \mathcal{E}_m^T(t_{k-1})\right) \tau^2 + n\mathcal{O}(\tau^3), \text{ for } 1 \le n \le 2N + 1. \end{cases}$$
(3.41)

Hence, for $1 \le n \le 2N + 1$:

$$|\epsilon_m^T(t_n)| \le n \left(\max_{1 \le n \le 2N+1} |\mathcal{E}_m^T(t_{n-1})| \right) \tau^2 + n\mathcal{O}(\tau^3) = n\mathcal{O}(\tau^2)$$
 (3.42)

Thus for $n = N_{ts}$:

$$|\epsilon_m^T(t_{N_{ts}})| \le N_{ts} \mathcal{O}\left(\left(\frac{T}{N_{ts}}\right)^2\right) = \mathcal{O}(\tau)$$
 (3.43)

The order of the error to approximate the exact volume of the volumetric increment may decrease over a period from 2 to 1 for the final value. Thus for any face m, the order of the truncation error $\epsilon_m^T(t_{N_{ts}})$ done to compute the zeroth Fourier coefficient of any integrated face mesh velocity $\hat{G}_{m,0}$ is one.

Recalling that the zeroth Fourier coefficients are then used to extract the periodic part of any volumetric increment see Theorem 3.3.1, the error committed on the rest of the Fourier coefficients of the integrated face mesh velocities is given by the following Lemma 3.3.6,

Lemma 3.3.6. In the context of Theorem 3.3.1, and under the Definitions 3.3.2, 3.3.3 and 3.3.4, for any face m the temporal-order of accuracy of the Fourier coefficients $\hat{G}_{m,k}$, for $-N \leq k \leq N$ with $k \neq 0$, is limited to between one and two.

Proof. For $1 \leq n \leq N_{ts}$, the periodic part of a volumetric increment can be further

expanded as:

$$p_m(t_n) = \Omega_m(t_n) - \frac{\Omega_m(t_{N_{ts}})}{T} t_n$$

$$= \sum_{k=1}^n \Omega_{m,h}(t_k) + \epsilon_m^T(t_n) - \left(\frac{\sum_{k=1}^{N_{ts}} \Omega_{m,h}(t_k) + \epsilon_m^T(t_{N_{ts}})}{T} \left(\frac{nT}{N_{ts}}\right)\right)$$

From equation (3.41), we have :

$$p_{m}(t_{n}) = \sum_{k=1}^{n} \Omega_{m,h}(t_{k}) + \left(\sum_{k=1}^{n} \mathcal{E}_{m}^{T}(t_{k-1})\right) \tau^{2} + n\mathcal{O}(\tau^{3})$$

$$- \left(\sum_{k=1}^{N_{ts}} \Omega_{m,h}(t_{k}) + \left(\sum_{k=1}^{N_{ts}} \mathcal{E}_{m}^{T}(t_{k-1})\right) \tau^{2} + (N_{ts})\mathcal{O}(\tau^{3}) + \left(\frac{nT}{N_{ts}}\right)\right)$$

$$= \left(\sum_{k=1}^{n} \Omega_{m,h}(t_{k}) - \frac{n}{N_{ts}} \sum_{k=1}^{N_{ts}} \Omega_{m,h}(t_{k})\right) + \left[\sum_{k=1}^{n} \mathcal{E}_{m}^{T}(t_{k-1}) - \frac{n}{N_{ts}} \sum_{k=1}^{N_{ts}} \mathcal{E}_{m}^{T}(t_{k-1})\right] \tau^{2} + n\mathcal{O}(\tau^{3}).$$

Then the truncation error on the periodic part of any volumetric increment $p_m(t)$ is given for $1 \le n \le N_{ts}$ by :

$$\epsilon_{p_m}^T(t_n) = \left[\sum_{k=1}^n \mathcal{E}_m^T(t_{k-1}) - \frac{n}{N_{ts}} \sum_{k=1}^{N_{ts}} \mathcal{E}_m^T(t_{k-1}) \right] \tau^2 + n\mathcal{O}(\tau^3).$$
 (3.44)

Since the bracketed term in equation (3.44) is dependent of n, the order of accuracy for any n is still unclear. To refine the determination of the order of accuracy during the computation of p_m , the approximation of an integral using the Riemann sum is exploited.

For any T-periodic function f at least three times continuous ($f \in \mathcal{C}^3([0;T])$), we have the following asymptotic development (3.45) where $f' = \frac{\partial f}{\partial t}$:

$$\begin{cases}
R_{N_{ts}} = \frac{T}{N_{ts}} \sum_{k=0}^{N_{ts}-1} f(t_k), \\
R_{N_{ts}} = \int_{0}^{T} f(t)dt - \frac{T}{2N_{ts}} (f(T) - f(0)) + \frac{T^2}{12(N_{ts})^2} (f'(T) - f'(0)) + \mathcal{O}\left(\left(\frac{T}{N_{ts}}\right)^3\right). \\
(3.45)
\end{cases}$$

Then applying this result to the truncation error $\epsilon_{p_m}^T(t_n)$, for $1 \leq n \leq N_{ts}$:

$$\epsilon_{p_m}^T(t_n) = \left[\sum_{k=0}^{n-1} \mathcal{E}_m^T(t_k) - \frac{n}{T} \frac{T}{N_{ts}} \sum_{k=0}^{N_{ts-1}} \mathcal{E}_m^T(t_k) \right] \tau^2 + n\mathcal{O}(\tau^3) \\
= \left[\sum_{k=0}^{n-1} \mathcal{E}_m^T(t_k) - \frac{n}{T} \left(\int_0^T \mathcal{E}_m^T(t) dt - \frac{\tau}{2} (\mathcal{E}_m^T(T) - \mathcal{E}_m^T(0)) \right) \right] \\
+ \frac{\tau^2}{12} (\mathcal{E}_m^{T'}(T) - \mathcal{E}_m^{T'}(0)) + \mathcal{O}(\tau^3) \right] \tau^2 + n\mathcal{O}(\tau^3) \\
= \left[\sum_{k=0}^{n-1} \mathcal{E}_m^T(t_k) - n \left(\langle \mathcal{E}_m^T \rangle_T - \frac{\tau}{2T} (\mathcal{E}_m^T(T) - \mathcal{E}_m^T(0)) \right) \right] \\
+ \frac{\tau^2}{12T} (\mathcal{E}_m^{T'}(T) - \mathcal{E}_m^{T'}(0)) \right] \tau^2 + n\mathcal{O}(\tau^3) \\
= \left[\sum_{k=0}^{n-1} \mathcal{E}_m^T(t_k) - n \langle \mathcal{E}_m^T \rangle_T \right] \tau^2 + n\mathcal{O}(\tau^3) \\
= \left[\sum_{k=0}^{n-1} (\mathcal{E}_m^T(t_k) - n \langle \mathcal{E}_m^T \rangle_T) \right] \tau^2 + n\mathcal{O}(\tau^3),$$

where $\langle . \rangle_T$ represents the mean of a function on the segment [0;T]. Taking advantage of the fact that the function $\Delta \mathcal{E}_m^T = \mathcal{E}_m^T - \langle \mathcal{E}_m^T \rangle_T$ is T-periodic with zero mean value

and exploiting a second time the expression (3.45), yields for $n = N_{ts}$:

$$\left\{ \sum_{k=0}^{N_{ts}-1} \left[\left(\mathcal{E}_m^T(t_k) - \langle \mathcal{E}_m^T \rangle_T \right) \right] \right\} \tau = \underbrace{\int_0^T \left(\Delta \mathcal{E}_m^T \right) dt}_{=0} - \frac{\tau}{2} (\Delta \mathcal{E}_m^T(T) - \Delta \mathcal{E}_m^T(0)) + \mathcal{O}(\tau^2)$$

$$= \quad -\frac{\tau}{2}(\mathcal{E}_m^T(T) - \mathcal{E}_m^T(0)) + \mathcal{O}(\tau^2).$$

(3.47)

Substituting back the expression (3.47) into the final equation in (3.46) for $n = N_{ts}$, leads to :

$$\epsilon_{p_m}^T(t_{N_{ts}}) = -\tau^2(\mathcal{E}_m^T(T) - \mathcal{E}_m^T(0)) + N_{ts}\mathcal{O}(\tau^3) = \mathcal{O}(\tau^2).$$
 (3.48)

In summary the truncation error committed on the periodic part of any volumetric increment follows the equation :

$$\begin{cases}
\epsilon_{p_m}^T(t_0) = 0, \\
\epsilon_{p_m}^T(t_n) = \left\{ \sum_{k=0}^{n-1} \left[\left(\mathcal{E}_m^T(t_k) - \langle \mathcal{E}_m^T \rangle_T \right) \right] \right\} \tau^2 + n\mathcal{O}(\tau^3), \text{ for } 1 \le n \le 2N. \\
\epsilon_{p_m}^T(t_{N_{ts}}) = \mathcal{O}(\tau^2).
\end{cases} (3.49)$$

In general, the order of the truncation error on the approximation of the periodic part of any volumetric increment used as input for the NLFD method is of order between one and two. Analytically, we observe that for each face m this order is determined by the sum $\sum_{k=0}^{n-1} \left[\left(\mathcal{E}_m^T(t_k) - \langle \mathcal{E}_m^T \rangle_T \right) \right]$, which is bounded for $1 \leq n \leq N_{ts}$

by $\left\{N_{ts} \max_{1 \leq k \leq N_{ts}} | \left(\mathcal{E}_{m}^{T}(t_{k}) - \langle \mathcal{E}_{m}^{T} \rangle_{T}\right)| \right\}$. This upper bound ensures that in the worst case, the order of accuracy is 1. However asymptotically it is reasonable to assume that for small and high values of n, the term $\sum_{k=0}^{n-1} \left[\left(\mathcal{E}_{m}^{T}(t_{k}) - \langle \mathcal{E}_{m}^{T} \rangle_{T}\right) \right]$ is small enough to consider that the truncation error is of order 2 whereas for n in the middle of the range $[1; N_{ts}]$, the order is greater than 1 but lesser than 2.

Assuming that the spectral convergence of the Fourier transform is reached and taking advantage of its bijectivity, the truncation error on the Fourier coefficients $\hat{G}_{m,k}$ and finally on the integrated face mesh velocities is of order between 1 and 2. Therefore the accuracy of the procedure is given by the following Corollary 3.3.7: Corollary 3.3.7. In the context of Theorem 3.3.1, and under the Definitions 3.3.2, 3.3.3 and 3.3.4, for any face m the temporal-order of accuracy of the integrated face mesh velocity is limited to between one and two.

Thus it is important to note that even if the method described in Section 3.3.1 enforced the Geometric Conservation Law, the integrated face mesh velocities are determined within an accuracy of order 1 to 2. This is a disadvantage since the benefit of the spectral convergence of the NLFD method.

3.3.3 Extension to two-dimensional quadrilateral grids

The extension of these results to a 2D quadrilateral grid where the exact volumetric increments are approximated through a sum of quadrilaterals (see Figure 3–5) is straightforward following the same procedure as in Section 3.3.2. The volume of

any quadrilateral can be approximated using a bilinear mapping between the physical domain and the computational space see Figure 3–6. This yields the adapted definitions.

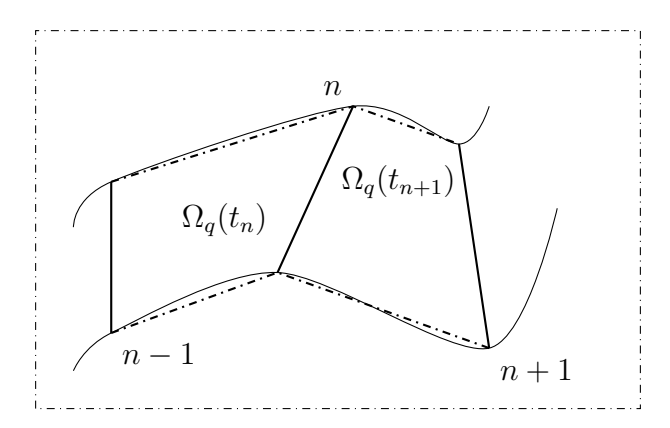


Figure 3–5: Approximation of a volumetric increment as a sum of quadrilaterals representing the linear volumetric increments between two successive time steps

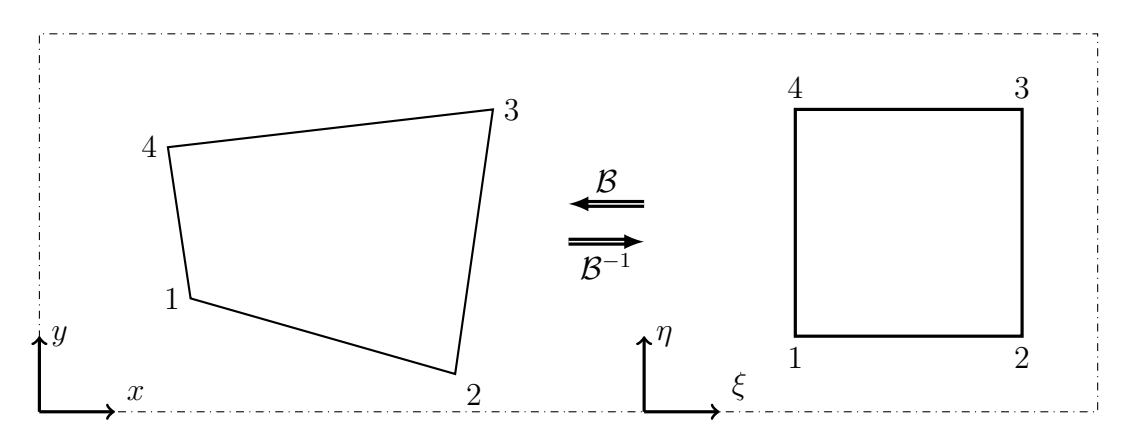


Figure 3–6: Bilinear mapping of a quadrilateral in the physical space (x, y) to a reference square in the computational domain (ξ, η)

Definition 3.3.8. The volume of any quadrilateral as a function of the position vectors of the vertices in the physical domain \mathbf{r}_i for i = 1, ..., 4, is evaluated through,

$$\Omega_q = \frac{1}{2} Det \left[(\mathbf{r}_3 - \mathbf{r}_1) , (\mathbf{r}_4 - \mathbf{r}_2) \right]. \tag{3.50}$$

Definition 3.3.9. For any face m of a quadrilateral cell, the exact volumetric increment is estimated through a sum of quadrilaterals each corresponding to the approximated volumetric increment between two time samples t_{n-1} and t_n and noted as $\Omega_{m,q}(t_n)$, (see Figure 3-4):

$$\begin{cases}
\Omega_m(t_0) = 0, \\
\Omega_m(t_n) = \left(\sum_{k=1}^n \Omega_{m,q}(t_k)\right) + \epsilon_m^T(t_n), \text{ for } 1 \le n \le 2N + 1,
\end{cases}$$
(3.51)

where $t_0 = 0$ is the initial instant corresponding to the undeformed mesh and $\epsilon_m^T(t_n)$ is the truncation error at time instant t_n .

By employing the new Definitions 3.3.8 and 3.3.9, and exploiting the bilinearity of the determinant in the volume calculation and following the same proofs as that shown for Lemmas 3.3.5 and 3.3.6, the Theorem 3.3.10 that ensures the correct order of accuracy of the Integrated Face Mesh Velocities is derived:

Theorem 3.3.10. In the context of Theorem 3.3.1, and under the Definitions 3.3.8 and 3.3.9, for any face m the temporal-order of accuracy of the integrated face mesh velocities is limited to between one and two.

3.4 Alternative approach based on the exact integrated face mesh velocities

3.4.1 Trilinear mapping

The computation of the metrics of a grid is often easier in a Cartesian grid, for this reason a mapping between the curvilinear physical domain and a Cartesian computational space can be performed. In this work, a trilinear mapping is already used to compute the volume of any *general hexahedron* (Definition 3.3.2) [5], but it can also be used to compute the temporal derivative of the volume, the surface vectors and the exact integrated face mesh velocities as long as the position and velocity vectors of the vertices are known. This section develops the derivation of these expressions.

Notation:

By default variables are expressed in the physical domain unless it is specified otherwise with the index " \mathcal{C} ".

 $\mathcal{T} \leftrightarrow \text{Trilinear mapping}$

 $\mathcal{C} \leftrightarrow \text{computational space} : (\xi, \eta, \zeta)$

 $m \leftrightarrow \text{any face of a hexahedral cell}$ (3.52)

 $\mathbf{n} \leftrightarrow \text{normal vector}$

 $\hat{\mathbf{n}} \leftrightarrow \text{unit normal vector}$

Derivation:

The mapping $\mathcal T$ from the physical domain to the computational space is introduced :

$$\mathcal{T} = \begin{cases} (\mathcal{D}_{\mathcal{C}}) \to (\mathcal{D}) \\ (\xi, \eta, \zeta) \to (x, y, z) = (\mathcal{T}(\xi, \eta, \zeta)), \end{cases}$$
(3.53)

where $(\mathcal{D}_{\mathcal{C}})$ is the computational space and (\mathcal{D}) is the physical domain. The application is defined by considering a reference cube in the computational space which

enables the mapping of any "general hexahedron" in the physical domain. A necessary and sufficient condition to ensure the invertibility of the mapping is the strict positivity of the Jacobian for any point of the element. However no simple relations exist in order to verify the positivity of the Jacobian in 3D [18, 21].

In this work, the position vector $\mathbf{r}=(x,y,z)$ in the physical domain is mapped through $\mathbf{r}_{\mathcal{C}}=(x(\xi,\eta,\zeta),y(\xi,\eta,\zeta),z(\xi,\eta,\zeta))$ based on the location vectors in the physical domain of the vertices $\mathbf{r}_i=[x_i,y_i,z_i]$ i=1,...,8 with the following convention derived from Figure 3–3:

$$\mathbf{r}_{\mathcal{C}} = (1 - \xi)(1 - \eta)(1 - \zeta)\mathbf{r}_{1} + \xi(1 - \eta)(1 - \zeta)\mathbf{r}_{2} + \xi\eta(1 - \zeta)\mathbf{r}_{3} + (1 - \xi)\eta(1 - \zeta)\mathbf{r}_{4}$$
$$+ (1 - \xi)(1 - \eta)\zeta\mathbf{r}_{5} + \xi(1 - \eta)\zeta\mathbf{r}_{6} + \xi\eta\zeta\mathbf{r}_{7} + (1 - \xi)\eta\zeta\mathbf{r}_{8},$$
(3.54)

where $0 \le \xi, \eta, \zeta \le 1$.

The velocity vector $\mathbf{v}=(v_x,v_y,v_z)$ in the physical domain is mapped in the same way $\mathbf{v}_{\mathcal{C}}=(v_x(\xi,\eta,\zeta),v_y(\xi,\eta,\zeta),v_z(\xi,\eta,\zeta))$ based on the velocity vectors of the vertices in the physical domain $\mathbf{v}_i=[v_{x,i},v_{y,i},v_{z,i}]\ i=1,...,8$:

$$\mathbf{v}_{\mathcal{C}} = (1 - \xi)(1 - \eta)(1 - \zeta)\mathbf{v}_{1} + \xi(1 - \eta)(1 - \zeta)\mathbf{v}_{2} + \xi\eta(1 - \zeta)\mathbf{v}_{3} + (1 - \xi)\eta(1 - \zeta)\mathbf{v}_{4} + (1 - \xi)(1 - \eta)\zeta\mathbf{v}_{5} + \xi(1 - \eta)\zeta\mathbf{v}_{6} + \xi\eta\zeta\mathbf{v}_{7} + (1 - \xi)\eta\zeta\mathbf{v}_{8}.$$
(3.55)

For any face m of a cell, the normal vector is given by one of the following expressions:

$$\mathbf{n}_{\mathcal{C},\zeta=0} = -\left(\frac{\partial \mathbf{r}_{\mathcal{C}}}{\partial \xi}\right) \mathbf{x} \left(\frac{\partial \mathbf{r}_{\mathcal{C}}}{\partial \eta}\right), \quad \mathbf{n}_{\mathcal{C},\zeta=1} = +\left(\frac{\partial \mathbf{r}_{\mathcal{C}}}{\partial \xi}\right) \mathbf{x} \left(\frac{\partial \mathbf{r}_{\mathcal{C}}}{\partial \eta}\right),$$

$$\mathbf{n}_{\mathcal{C},\xi=0} = -\left(\frac{\partial \mathbf{r}_{\mathcal{C}}}{\partial \eta}\right) \mathbf{x} \left(\frac{\partial \mathbf{r}_{\mathcal{C}}}{\partial \zeta}\right), \quad \mathbf{n}_{\mathcal{C},\xi=1} = +\left(\frac{\partial \mathbf{r}_{\mathcal{C}}}{\partial \eta}\right) \mathbf{x} \left(\frac{\partial \mathbf{r}_{\mathcal{C}}}{\partial \zeta}\right), \quad (3.56)$$

$$\mathbf{n}_{\mathcal{C},\eta=0} = -\left(\frac{\partial \mathbf{r}_{\mathcal{C}}}{\partial \zeta}\right) \mathbf{x} \left(\frac{\partial \mathbf{r}_{\mathcal{C}}}{\partial \xi}\right), \quad \mathbf{n}_{\mathcal{C},\eta=1} = +\left(\frac{\partial \mathbf{r}_{\mathcal{C}}}{\partial \zeta}\right) \mathbf{x} \left(\frac{\partial \mathbf{r}_{\mathcal{C}}}{\partial \xi}\right),$$

where the signs are determined in order to have the normals pointing outward of the cell volume. The Jacobian matrix $J(\xi, \eta, \zeta)$ is expressed as:

$$J(\xi, \eta, \zeta) = \begin{pmatrix} \frac{\partial \mathbf{r}_{\mathcal{C}}}{\partial \xi} & \frac{\partial \mathbf{r}_{\mathcal{C}}}{\partial \eta} & \frac{\partial \mathbf{r}_{\mathcal{C}}}{\partial \zeta} \end{pmatrix}$$
(3.57)

and its determinant can be calculated with one of the following expressions:

$$|J| = \left(\frac{\partial \mathbf{r}_{\mathcal{C}}}{\partial \xi}\right) \cdot \left[\left(\frac{\partial \mathbf{r}_{\mathcal{C}}}{\partial \eta}\right) \times \left(\frac{\partial \mathbf{r}_{\mathcal{C}}}{\partial \zeta}\right)\right] = \left(\frac{\partial \mathbf{r}_{\mathcal{C}}}{\partial \eta}\right) \cdot \left[\left(\frac{\partial \mathbf{r}_{\mathcal{C}}}{\partial \zeta}\right) \times \left(\frac{\partial \mathbf{r}_{\mathcal{C}}}{\partial \zeta}\right)\right] = \left(\frac{\partial \mathbf{r}_{\mathcal{C}}}{\partial \zeta}\right) \cdot \left[\left(\frac{\partial \mathbf{r}_{\mathcal{C}}}{\partial \zeta}\right) \times \left(\frac{\partial \mathbf{r}_{\mathcal{C}}}{\partial \eta}\right)\right].$$
(3.58)

Once the position vector, velocity vector, normal vectors and Jacobian are known, these quantities are used to compute the integrals of the volume and mesh velocities through a change of variables.

Volume integral

Through the application of the divergence theorem, the volume of any "general hexahedron" can be evaluated as such,

$$\Omega = \int_{\Omega} d\Omega = \iint_{\partial\Omega} \frac{1}{3} \mathbf{r} \cdot \mathbf{dS} = \frac{1}{3} \iint_{\partial\Omega} (\mathbf{r} \cdot \hat{\mathbf{n}}) dS$$

We can then write the integral in the computational domain through the trilinear mapping to acquire,

$$\Omega = \frac{1}{3} \iint_{\partial \Omega} (\mathbf{r} \cdot \hat{\mathbf{n}}) dS = \frac{1}{3} \iint_{\partial \Omega_{\mathcal{C}}} (\mathbf{r}_{\mathcal{C}} \cdot \hat{\mathbf{n}}_{\mathcal{C}}) |J_{\mathcal{C}}| dS_{\mathcal{C}}$$

$$=\frac{1}{3}\sum_{m=1}^{N_f}\iint_{\partial\Omega_{\mathcal{C},m}}(\mathbf{r}_{\mathcal{C},m}\cdot\hat{\mathbf{n}}_{\mathcal{C},m})|J_{\mathcal{C},m}|dS_{\mathcal{C},m},$$

where $dS_{\mathcal{C},m}$ is either $d\xi d\eta$, $d\eta d\zeta$ or $d\zeta d\xi$ and the integral boundaries are $[0\ 1]^2$. **N.B.**: On any face of the "general hexahedron" only one of the variables in the computational space ξ , η or ζ has a fixed value. Thus the quantity $(\mathbf{r}_{\mathcal{C},m}.\hat{\mathbf{n}}_{\mathcal{C},m})|J_{\mathcal{C},m}|$ is still a function of two variables which has to be integrated over the face.

For each face, the computation of the integral over the surface under this form is not straightforward (the difficulty comes from the unit normal vector) and needs to be simplified *a priori*. This is done by exploiting the relation (3.59), for the derivation of this expression see Appendix B in [45]:

$$\hat{\mathbf{n}}_{\mathcal{C},m}|J_{\mathcal{C},m}| = C_{\mathcal{C},m}\hat{\mathbf{N}}_{\mathcal{C},m},\tag{3.59}$$

where $C_{\mathcal{C},m} = C(\xi, \eta, \zeta)$ is the cofactor matrix of the Jacobian matrix J for the trilinear mapping and $\hat{\mathbf{N}}_{\mathcal{C},m}$ is the constant unit normal vector to the corresponding

face in the computational space:

$$\hat{\mathbf{N}}_{\mathcal{C},\zeta=0} = [\begin{array}{cccc} 0 & 0 & -1 \end{array}]^t, \quad \hat{\mathbf{N}}_{\mathcal{C},\zeta=1} = [\begin{array}{cccc} 0 & 0 & +1 \end{array}]^t,$$

$$\hat{\mathbf{N}}_{\mathcal{C},\eta=0} = [0 \quad -1 \quad 0]^t, \quad \hat{\mathbf{N}}_{\mathcal{C},\eta=1} = [0 \quad +1 \quad 0]^t, \tag{3.60}$$

$$\hat{\mathbf{N}}_{\mathcal{C},\xi=0} = \begin{bmatrix} -1 & 0 & 0 \end{bmatrix}^t$$
, $\hat{\mathbf{N}}_{\mathcal{C},\xi=1} = \begin{bmatrix} +1 & 0 & 0 \end{bmatrix}^t$.

Once the equation (3.59) is substituted into the integrals over the surfaces, an explicit expression of the volume as a function of \mathbf{r}_i , i = 1, ..., 8 is obtained:

$$(\Omega)_{\mathcal{T}} = (\Omega_{4321} + \Omega_{5678} + \Omega_{3487} + \Omega_{1265} + \Omega_{4158} + \Omega_{2376})_{\mathcal{T}}, \tag{3.61}$$

where for any set $(i, j, k, l) \in \{4321; 5678; 3487; 1265; 4158; 2376\}$, the volumetric contribution of the face S_{ijkl} is given by (3.62):

$$(\Omega_{ijkl})_{\mathcal{T}} = \frac{1}{3} \iint_{\partial\Omega_{\mathcal{C},ijkl}} \mathbf{r}_{\mathcal{C},ijkl} \cdot (C_{\mathcal{C},ijkl} \hat{\mathbf{N}}_{\mathcal{C},ijkl}) dS_{\mathcal{C},ijkl}$$

$$= \frac{1}{12} (\mathbf{r}_i + \mathbf{r}_j) \cdot ((\mathbf{r}_j + \mathbf{r}_k) \times (\mathbf{r}_i + \mathbf{r}_l)).$$
(3.62)

Temporal derivative of the volumetric integral

The temporal derivative of the volumetric integral can be expressed as,

$$\frac{\partial \Omega}{\partial t} = \frac{\partial}{\partial t} \int_{\Omega} d\Omega. \tag{3.63}$$

By substituting the results of the previous section, primarily equations (3.61) and (3.62), an explicit expression of the temporal derivative of the volume as a function

of \mathbf{r}_i and \mathbf{v}_i , i = 1, ..., 8 is derived:

$$\left(\frac{\partial\Omega}{\partial t}\right)_{\mathcal{T}} = \left(\frac{\partial\Omega_{4321}}{\partial t} + \frac{\partial\Omega_{5678}}{\partial t} + \frac{\partial\Omega_{3487}}{\partial t} + \frac{\partial\Omega_{1265}}{\partial t} + \frac{\partial\Omega_{4158}}{\partial t} + \frac{\partial\Omega_{2376}}{\partial t}\right)_{\mathcal{T}},$$
(3.64)

where for any set $(i, j, k, l) \in \{4321; 5678; 3487; 1265; 4158; 2376\}$, the temporal derivative volumetric contribution of the face S_{ijkl} is given by (3.65):

$$\left(\frac{\partial\Omega_{ijkl}}{\partial t}\right)_{\mathcal{T}} = \frac{1}{12}(\mathbf{v}_i + \mathbf{v}_j) \cdot ((\mathbf{r}_j + \mathbf{r}_k) \times (\mathbf{r}_i + \mathbf{r}_l))$$

$$+ \frac{1}{12}(\mathbf{r}_i + \mathbf{r}_j) \cdot ((\mathbf{v}_j + \mathbf{v}_k) \times (\mathbf{r}_i + \mathbf{r}_l))$$

$$+ \frac{1}{12}(\mathbf{r}_i + \mathbf{r}_j) \cdot ((\mathbf{r}_j + \mathbf{r}_k) \times (\mathbf{v}_i + \mathbf{v}_l)).$$
(3.65)

Integrated face mesh velocities

The integral of the face mesh velocity in the physical domain for a face m is given by,

$$G_m = \iint_{\partial\Omega_m} (\mathbf{v} \cdot \hat{\mathbf{n}}_m) dS_m.$$

By introducing the trilinear mapping, we can express the integrated face mesh velocities as,

$$G_m = \iint_{\partial\Omega_{\mathcal{C},m}} \mathbf{v}_{\mathcal{C},m} \cdot (\hat{\mathbf{n}}_{\mathcal{C},m} | J_{\mathcal{C},m}|) dS_{\mathcal{C},m} = \iint_{\partial\Omega_{\mathcal{C},m}} \mathbf{v}_{\mathcal{C},m} \cdot (C_{\mathcal{C},m} \hat{\mathbf{N}}_{\mathcal{C},m}) dS_{\mathcal{C},m}.$$

Once the integration is performed, the explicit expressions of the integrated face mesh velocities are obtained as a function of \mathbf{r}_i and \mathbf{v}_i , i = 1, ..., 8. For a face with

e set
$$(i, j, k, l) \in \{4321; 5678; 3487; 1265; 4158; 2376\}$$
:
$$\begin{cases}
\mathbf{v}_{t} = \mathbf{v}_{i} + \mathbf{v}_{j} + \mathbf{v}_{k} + \mathbf{v}_{l} \\
\mathbf{S}_{ijkl} = (\mathbf{r}_{i} \times \mathbf{r}_{j}) + (\mathbf{r}_{j} \times \mathbf{r}_{k}) + (\mathbf{r}_{k} \times \mathbf{r}_{l}) + (\mathbf{r}_{l} \times \mathbf{r}_{i}) \\
\mathbf{S}_{\alpha\beta\gamma} = (\mathbf{r}_{\alpha} \times \mathbf{r}_{\beta}) + (\mathbf{r}_{\beta} \times \mathbf{r}_{\gamma}) + (\mathbf{r}_{\gamma} \times \mathbf{r}_{\alpha}) \text{ for any set } \alpha, \beta, \gamma
\end{cases}$$

$$(3.66)$$

$$(3.66)$$

$$(3.66)$$

$$(3.66)$$

It was verified that with these expressions for the IFMV and the temporal derivative of the volume as functions of velocity and position vectors of the vertices, the semi-discrete equation of the GCL (3.5) is analytically retrieved. In other words, the sum of equation (3.66) applied to the 6 sets $\{4321, 5678, 3487, 1265, 4158, 2376\}$ is equal to expression (3.64).

Derivation of the GCL in the NLFD framework

The methods presented in Sections 3.2 and 3.3 to enforce the GCL are based on equation (3.13), and the integrated face mesh velocities are deduced from the calculation of the volumetric increments as input. The approach presented in this section using the trilinear mapping is quite different because no volumetric increments are computed, the integrated face mesh velocities are directly evaluated in physical time using equation (3.66). In addition the cell volumes are computed using equation (3.31). Hence in the GCL equation as established in (3.5), both Ω and $G = \sum_{m=1}^{N_f} G_m$ are exactly calculated, the only degree of freedom remaining to enforce the equation is the discretization of the temporal derivative operator $\left(\frac{\partial}{\partial t}\right)$. In the NLFD framework, this operator is discretized in the Fourier domain and is a function of the number of harmonics N employed in the temporal discretization. Therefore the GCL equation will be satisfied if and only if the temporal derivative of the cell volume expressed in Fourier space converge to the Fourier temporal differentiation applied to the cell volume,

DFT
$$\left\{ \left(\frac{\partial \Omega}{\partial t} \right)_{\mathcal{T}} \right\} = \left(\frac{\partial}{\partial t} \right)_{Fourier} \left(\text{DFT} \left\{ (\Omega_{\mathcal{T}}) \right\} \right),$$
 (3.67)

where \mathcal{T} refers to the trilinear mapping. Hence, this method will not enforce the GCL for any number of time steps contrary to the method presented in Section 3.3, but for a sufficient number of harmonics ensuring the convergence of the equation (3.67). Since this approach is based on the exact integrated face mesh velocities and ensures the GCL with a spectral rate of convergence depending on the mesh motion, it provides a good alternative to the method exploiting the volumetric increments with an order of accuracy comprised between one and two. In the Chapter 4, we will present the numerical results of these different methods for several test cases.

3.4.3 Extension to two-dimensional quadrilateral grids

As stated in Section 3.3.3, any quadrilateral cell in the physical domain (x, y) can be mapped through a bilinear formulation to a reference square in the computational space (ξ, η) . In this work, for any quadrilateral cell, both position and velocity vectors in the physical domain respectively denoted \mathbf{r} and \mathbf{v} are mapped based on the location and velocity vectors of the vertices respectively \mathbf{r}_i and \mathbf{v}_i for i = 1, ..., 4 (see Figure 3–6 for the numeration), the corresponding quantities in the computational space are defined as:

$$\mathbf{r}_{\mathcal{C}} = (1 - \xi)(1 - \eta)\mathbf{r}_1 + \xi(1 - \eta)\mathbf{r}_2 + \xi\eta\mathbf{r}_3 + (1 - \xi)\eta\mathbf{r}_4, \tag{3.68}$$

$$\mathbf{v}_{\mathcal{C}} = (1 - \xi)(1 - \eta)\mathbf{v}_1 + \xi(1 - \eta)\mathbf{v}_2 + \xi\eta\mathbf{v}_3 + (1 - \xi)\eta\mathbf{v}_4, \tag{3.69}$$

where $0 \le \xi, \eta \le 1$.

Then the volume Ω and the integrated face mesh velocities G_{ij} are exactly derived and expressed in the physical domain as:

$$\Omega = \frac{1}{2} \operatorname{Det} \left[(\mathbf{r}_3 - \mathbf{r}_1) , (\mathbf{r}_4 - \mathbf{r}_2) \right], \qquad (3.70)$$

$$G_{ij} = \frac{1}{2} \text{Det} \left[(\mathbf{v}_i + \mathbf{v}_j) , (\mathbf{r}_j - \mathbf{r}_i) \right],$$
 (3.71)

where ij belong to one of the 4 sets $\{12; 23; 34; 41\}$.

Thus in the GCL equation (3.5), both the volume and the integrated face mesh velocities are exactly evaluated and the results of the previous Section 3.4.2 are applicable. Therefore on quadrilateral meshes, this method will enforce the GCL for a sufficient number of harmonics in the NLFD discretization and employs the exact integrated face mesh velocities, hence it provides a good alternative to the methods based on the volumetric increments.

3.5 Extension of the results to Time-Spectral method

In this section, we extent the previous results from Section 3.3.2 to Time-Spectral (TS) method presented by Gopinath and al. [8, 9]. Compared to the NLFD method which solves the governing equations in the frequency domain, the Time-Spectral

method solves the governing equations in the time domain but exploits the features of a spectral approach.

3.5.1 Time-Spectral method

Assuming a periodic flow and a periodic deformation of the mesh, we recall the temporal discretization of the modified state vector $\bar{\mathbf{w}} = \Omega \mathbf{w}$ equations (2.12) and (2.14),

$$\bar{\mathbf{w}}(t) = \sum_{k=-N}^{N} \hat{\mathbf{w}}_k e^{i(2\pi k/T)t},$$

with:

$$\hat{\mathbf{w}}_k = \frac{1}{2N+1} \sum_{n=0}^{2N} \Omega(t_n) \mathbf{w}(t_n) e^{-i(2\pi k/T)t_n},$$

where T is the time period, N is the number of modes considered in the DFT and t_n the equally spaced time instances given by,

$$t_n = \frac{n}{2N+1}T$$
, for $n = 0, ..., 2N$.

In Fourier space, the time discretization operator leads to,

$$\frac{\partial \bar{\mathbf{w}}}{\partial t}(t) = \sum_{k=-N}^{N} \frac{i2\pi k}{T} \hat{\mathbf{w}}_k e^{i(2\pi k/T)t}, \qquad (3.72)$$

$$\Leftrightarrow \frac{\partial \bar{\mathbf{w}}}{\partial t}(t) = \frac{2\pi}{T} \sum_{k=-N}^{N} ik \left(\frac{1}{2N+1} \sum_{K=0}^{2N} \Omega(t_K) \mathbf{w}(t_K) e^{-i(2\pi k/T)t_K} \right) e^{i(2\pi k/T)t}.$$
(3.73)

By evaluating this expression for each time instance t_n , we have for n = 0, ..., 2N,

$$\frac{\partial \bar{\mathbf{w}}}{\partial t}(t_n) = \frac{2\pi}{T} \sum_{k=-N}^{N} ik \left(\frac{1}{2N+1} \sum_{K=0}^{2N} \Omega(t_K) \mathbf{w}(t_K) e^{-i(2\pi k/T)t_K} \right) e^{i(2\pi k/T)t_n}, \quad (3.74)$$

$$\Leftrightarrow \frac{\partial \bar{\mathbf{w}}}{\partial t}(t_n) = \sum_{K=0}^{2N} \left[\Omega(t_K) \mathbf{w}(t_K) \left(\frac{2\pi}{T} \frac{1}{2N+1} \sum_{k=-N}^{N} ik e^{i(2\pi k)(n-K)/(2N+1)} \right) \right]. \quad (3.75)$$

We introduce, the coefficients $d_{n,K}$, defined for n = 0, ..., 2N by,

$$d_{n,K} = \frac{2\pi}{T} \frac{1}{2N+1} \sum_{k=-N}^{N} ik e^{i(2\pi k)(n-K)/(2N+1)},$$
(3.76)

the compact form of the coefficients for an odd number of time steps is written as follows (for the derivation see Reference [9]),

$$d_{n,K} = \begin{cases} \frac{2\pi}{T} \frac{1}{2} (-1)^{n-K} \csc\left(\frac{\pi(n-K)}{2N+1}\right), & \text{if } K \neq n \\ 0, & \text{if } K = n, \end{cases}$$
(3.77)

and,

$$\frac{\partial \bar{\mathbf{w}}}{\partial t}(t_n) = \sum_{K=0}^{2N} d_{n,K} \bar{\mathbf{w}}(t_K). \tag{3.78}$$

The temporal-derivation operator appears as the multiplication of a matrix $\mathcal{D} = (d_{n,K})_{0 \leq n,K \leq 2N}$ with each vector $(\bar{\mathbf{w}}_i(t_K))_{0 \leq K \leq 2N}$, for i = 1,...,5 where the index i refers to the component of the modified state vector in the governing equations. In addition, this matrix is skew-symmetric, independent of any state variables and completely determined by the number of harmonics used in the DFT and the temporal period. Then a pseudo-time t^* is introduced and the equations are solved in the time domain through,

$$\frac{\partial \bar{\mathbf{w}}}{\partial t^*}(t_n) + \frac{\partial \bar{\mathbf{w}}}{\partial t}(t_n) + \mathbf{R}(\mathbf{w}(t_n)) = 0, \text{ for } n = 0, ..., 2N.$$
(3.79)

3.5.2 Derivation and enforcement of the GCL

Recall that in order to obtain a consistent solution method, the GCL must be discretized using the same numerical scheme employed to discretize the governing equations. In the case of Time-Spectral method, it leads to the following Theorem 3.5.1,

Theorem 3.5.1. Let Ω be a discretized control volume, enclosed by N_f faces, and subjected to a periodic motion of its vertices. Then given the knowledge of the exact volumetric increments Ω_m for $m = 1, ..., N_f$, a sufficient condition to ensure the satisfaction of GCL in the TS framework is the computation of the integrated face mesh velocities through the following relations,

$$\mathbf{G}_m = (\mathcal{D})\boldsymbol{p}_m + \langle G_m \rangle_T (\mathcal{I}_{\mathcal{N}}), \tag{3.80}$$

where for all m, $\langle G_m \rangle_T$ are the temporal mean values of the integrated face mesh velocities, \mathcal{I}_N is the identity matrix of dimension 2N+1, $\mathbf{G}_m=(G_m(t_n))_{0\leq n\leq 2N}$ and $\mathbf{p}_m=(p_m(t_n))_{0\leq n\leq 2N}$ are the vectors grouping the time instances of respectively the integrated face mesh velocities and the periodic part of the exact volumetric increments given by,

$$p_m(t) = \Omega_m(t) - \left(\frac{\Omega_m(T)}{T}\right)t, \qquad (3.81)$$

and $\mathcal{D} = (d_{n,K})_{0 \leq n,K \leq 2N}$ is the matrix representing the temporal derivation operator of the Time-Spectral method, defined by its coefficients $d_{n,K}$ for $0 \leq n, K \leq 2N$,

$$d_{n,K} = \begin{cases} \frac{\pi}{T} (-1)^{n-K} \csc\left(\frac{\pi(n-K)}{2N+1}\right), & if \quad K \neq n \\ 0, & if \quad K = n. \end{cases}$$
(3.82)

Proof. Under the assumption that the motion of the vertices is periodic, the temporal rate of change of the algebraic volume swept by each face through time is periodic. Thus the temporal derivative of the volumetric increments and the integrated face mesh velocities are periodic, the DFT is applied to equation (3.13) leading to:

$$G_m(t) = \frac{\partial \Omega_m}{\partial t} = \hat{G}_{m,0} + \sum_{k=-N, k\neq 0}^{N} \hat{G}_{m,k} e^{i\frac{2\pi}{T}kt}, \qquad (3.83)$$

where for any face m, $\hat{G}_{m,k}$ are the Fourier coefficients of both the temporal derivative of the volumetric increment and the integrated face mesh velocity. The mean of a function expandable in Fourier serie is given by its zeroth Fourier coefficient thus,

$$\langle G_m \rangle_T = \hat{G}_{m,0}. \tag{3.84}$$

From the proof of Theorem 3.3.1, we have the following relations,

$$\Omega_m(t) = l_m(t) + p_m(t), \qquad (3.85)$$

$$l_m(t) = \hat{G}_{m,0}t = \frac{\Omega_m(T)}{T}t,$$
 (3.86)

$$p_m(t) = \hat{\Omega}_{m,0} + \sum_{k=-N,k\neq 0}^{N} \frac{T}{i2\pi k} \hat{G}_{m,k} e^{i\frac{2\pi}{T}kt}, \qquad (3.87)$$

$$p_m(t) = \Omega_m(t) - \left(\frac{\Omega_m(T)}{T}\right)t. \tag{3.88}$$

Then, by exploiting these results and applying the Time-Spectral temporal derivation to the periodic part of the volumetric increment, we can write for each face m and

time instance t_n , with n = 0, ..., 2N,

$$G_{m}(t_{n}) = \frac{\partial \Omega_{m}}{\partial t}(t_{n})$$

$$= \frac{\partial (l_{m} + p_{m})}{\partial t}(t_{n})$$

$$= \langle G_{m} \rangle_{T} + \frac{\partial p_{m}}{\partial t}(t_{n})$$

$$= \langle G_{m} \rangle_{T} + \sum_{K=0}^{2N} d_{n,K} p_{m}(t_{K}),$$
(3.89)

Finally, if we group all the time instances in a vector \mathbf{G}_m , we obtain,

$$\mathbf{G}_{m} = (\mathcal{D})\boldsymbol{p}_{m} + \langle G_{m} \rangle_{T} (\mathcal{I}_{\mathcal{N}}), \tag{3.90}$$

where $\mathcal{I}_{\mathcal{N}}$ is the identity matrix of dimension 2N+1 and $\mathcal{D}=(d_{n,K})_{0\leq n,K\leq 2N}$ is the matrix representing the temporal derivation operator of the Time-Spectral method. The condition given by equation (3.90) is a criteria to ensure that the GCL are enforced in the Time-Spectral framework.

The new approaches to enforce the Geometric Conservation Law developed in Chapter 3 are numerically tested in order to validate their procedures. The protocol, test cases and results are presented in the following sections. A simple 3D finite volume solver was developed on Matlab¹ to perform the simulations.

4.1 Protocol

The physical interpretation of the GCL is that any uniform flow must be preserved by the numerical scheme employed for the flow solver and independently of the mesh movements. This law imposes constraints on the manner to compute some geometrical quantities such as the volume and the integrated face mesh velocities. Thus the first step of our test is to ensure the preservation of uniform flow by computing the relative error between the initially defined uniform state vector \mathbf{w}_0 and the computed state vector \mathbf{w} by the flow solver,

$$RelErr = \max_{0 \le n \le 2N} \left\{ \max_{1 \le n_v \le N_{cell}} \left(\max_{1 \le j \le 5} \left| \frac{w_j(n_v, t_n) - w_{0,j}(n_v, t_n)}{w_{0,j}(n_v, t_n)} \right| \right) \right\}, \tag{4.1}$$

where $w_1 = \rho$, $w_2 = \rho u_1$, $w_3 = \rho u_2$, $w_4 = \rho u_3$ and $w_5 = \rho E$ and n_v is the index pointing to the grid cell with N_{cell} the number of cells in the mesh.

¹ The MathWorks, Inc., Natick, Massachusetts, United States.

However the verification of uniform flow preservation only guarantees that the GCL are satisfied "by summing over the faces", but not that the computed integrated face mesh velocities are correct. Indeed as long as the sum of the temporal derivative of the volumetric increments is equal to the temporal derivative of the cell volume,

$$\frac{\partial \Omega}{\partial t} = \sum_{m=1}^{N_f} \frac{\partial \Omega_m}{\partial t},\tag{4.2}$$

the deduced integrated face mesh velocities from the temporal derivative of the volumetric increments from equation (3.13) enforce the GCL after the summation through the faces (see equation (3.5)) but the integrated face mesh velocities themselves may not converge to the correct values.

Thus in order to verify that the GCL are enforced with a correct evaluation of the integrated face mesh velocities, the values derived from the trilinear mapping equations (3.64) and (3.66) based on the location and velocity vectors of the grid points retrieved from the dynamic mesh deformation, are considered as reference. Therefore for each motion of the mesh and for various number of harmonics N, four different implementations of the integrated face mesh velocities are compared:

- 1. the IFMV deduced from the linear volumetric increments from Tradif and al. [37] see Figure 3–1 noted as "NLFD-LVI";
- 2. the IFMV calculated with the new method based on the exact volumetric increments approximated as a sum of "general hexahedra" (Definition 3.3.2) see Figure 3–4 and noted as "NLFD-AEVI";

- the approximation obtained by taking the average of the velocity of the four vertices defining a face and projected along the surface normal vector noted as "AVG";
- 4. the method based on the trilinear mapping noted as "TRI-MAP" and used as reference for the exact values of the IFMV.

For each of these approaches, the preservation of uniform flow is tested. Then different quantities are compared by computing the maximum absolute error:

• comparison of the sum of the IFMV to the NLFD temporal derivative of the cell volume computed using the numerical scheme of the flow solver. This comparison is similar to a demonstration of the preservation of uniform flow:

$$AbsErr_{1} = \max_{0 \leq n \leq 2N} \left\{ \max_{1 \leq n_{v} \leq N_{cell}} \left| \left(\sum_{m=1}^{N_{f}} G_{m}(n_{v}, t_{n}) \right)_{METHOD} - \left(\frac{\partial \Omega}{\partial t}(n_{v}, t_{n}) \right)_{NLFD} \right| \right\};$$

$$(4.3)$$

• comparison of the IFMV to the reference integrated face mesh velocities (TRI-MAP) in each direction dir = x, y or z:

$$AbsErr_{2} = \max_{0 \le n \le 2N} \left\{ \max_{1 \le n_{v} \le N_{cell}} \left| (G_{m,dir}(n_{v}, t_{n}))_{METHOD} - (G_{m,dir}(n_{v}, t_{n}))_{TRI-MAP} \right| \right\}.$$
(4.4)

4.2 Test cases

This section presents the different mesh motions impose as test cases. The temporal period is always taken to be unity. All tests are performed on a square mesh of size $10 \times 10 \times 10$, and of lengths $L_x = 3.2$, $L_y = 2.8$, and $L_z = 2.4$. The undeformed positions of the mesh are indexed with the subscript 0, if needed the

RBF points are indexed with the subscript r. The two parameters in the Jameson-Schmidt-Turkel (JST) scheme are $\kappa^{(2)} = 1$ and $\kappa^{(4)} = 1/32$. The simulations are run for a number of harmonics, N from 1 to 20. The mesh deformations for cases 2, 4 and 5 at an arbitrary time instant are presented on Figure 4–1.

4.2.1 Without RBF

Three test cases are performed by directly imposing the mesh deformation to the entire mesh. The velocity of the vertices is computed based on the analytic temporal derivation of the vector position of the vertices. For any vertex, its initial position is noted (x_0, y_0, z_0) . The parameters A_x , A_y , A_z , R, and α_0 can be arbitrarily chosen as long as no degenerative cells (cells with negative volume) appear during the motion. The analytic functions employed for the motions are as follows:

Case 1: 1-harmonic sinusoidal perturbation of the mesh with a linear motion, the direction is held fixed while each point has its own motion amplitude based on its initial position:

$$\begin{cases} x(t) = x_0 + A_x \sin\left(\frac{\pi x_0}{L_x}\right) \sin\left(\frac{\pi y_0}{L_y}\right) \sin\left(\frac{\pi z_0}{L_z}\right) \sin(2\pi t) \\ y(t) = y_0 + A_y \sin\left(\frac{\pi x_0}{L_x}\right) \sin\left(\frac{\pi y_0}{L_y}\right) \sin\left(\frac{\pi z_0}{L_z}\right) \sin(2\pi t) \\ z(t) = z_0 + A_z \sin\left(\frac{\pi x_0}{L_x}\right) \sin\left(\frac{\pi y_0}{L_y}\right) \sin\left(\frac{\pi z_0}{L_z}\right) \sin(2\pi t) \end{cases}$$
(4.5)

Case 2: 2D perturbation of the mesh with a non-linear motion; however the timeaverage volume swept by a face, $\hat{G}_{m,0} = 0$ in equation (3.23). For any cell the projection of the motion along a plane z = constant is shown in Figure 4-4:

$$\begin{cases}
\alpha(t) = \alpha_0 \sin(2\pi t) \\
x(t) = x_0 + y_0 \cos(\frac{\pi}{2} - \alpha(t)) \\
y(t) = y_0 \sin(\frac{\pi}{2} - \alpha(t)) \\
z(t) = z_0
\end{cases}$$
(4.6)

Case 3: 2D perturbation of the mesh with a non-linear motion and $\hat{G}_{m,0} \neq 0$ in equation (3.23), the deformation is prescribed only for the interior grid points while the boundary points are fixed. The projection of the motion along a plane z = constant is identical to the movement of the 3rd node on the Figure 3–2 presented in Section 3.2:

$$\begin{cases}
\alpha(t) = 2\pi t \\
x(t) = x_0 + R(1 - \cos(\alpha(t))) \\
y(t) = y_0 + R\sin(\alpha(t)) \\
z(t) = z_0
\end{cases}$$
(4.7)

4.2.2 With RBF

Two test cases are performed by deforming the mesh through the RBF. The analytic functions employed for the RBF motions are as follows:

Case 4: 3D perturbation of the mesh using the RBF, with each point having its own linear motion (amplitude and direction):

$$\begin{cases} s_x(t) = r_x(x_{0,r}, y_{0,r}, z_{0,r}) \sin(2\pi y_{0,r}) \sin(2\pi z_{0,r}) \sin(2\pi t) \\ s_y(t) = r_y(x_{0,r}, y_{0,r}, z_{0,r}) \sin(2\pi x_{0,r}) \sin(2\pi z_{0,r}) \sin(2\pi t) \\ s_z(t) = r_z(x_{0,r}, y_{0,r}, z_{0,r}) \sin(2\pi y_{0,r}) \sin(2\pi z_{0,r}) \sin(2\pi t) \\ \text{where } r_x(x_{0,r}, y_{0,r}, z_{0,r}); r_y(x_{0,r}, y_{0,r}, z_{0,r}) \text{ and} \\ r_z(x_{0,r}, y_{0,r}, z_{0,r}) \text{ are randomly generated} \end{cases}$$
(4.8)

Case 5: simulation of a sinusoidal pitching motion:

$$\begin{cases}
\alpha(t) = \alpha_0 \cos(2\pi t) \\
x_p = 0.621L_x \\
s_x(t) = (x_{0,r} - x_p)[\cos(\alpha(t)) - 1] + y_{0,r}\sin(\alpha(t)) \\
s_y(t) = -(x_{0,r} - x_p)\sin(\alpha(t)) + y_{0,r}[\cos(\alpha(t)) - 1] \\
s_z(t) = z_{0,r}
\end{cases}$$
(4.9)

4.3 Freestream preservation

The results demonstrating uniform flow preservation are shown for all test cases in Figure 4–2. The evolution of the relative error defined by equation (4.1) is presented as a function of the number of time steps N_{ts} .

The results show that the two methods employing the IFMV deduced from the Fourier discretization preserve uniform flow, while the approximation derived from the AVG yields the least accurate results. This is consistent since for both methods NLFD-LVI and NLFD-AEVI, despite different definitions of the volumetric increments, they still ensure that the sum of the temporal derivative of the volumetric

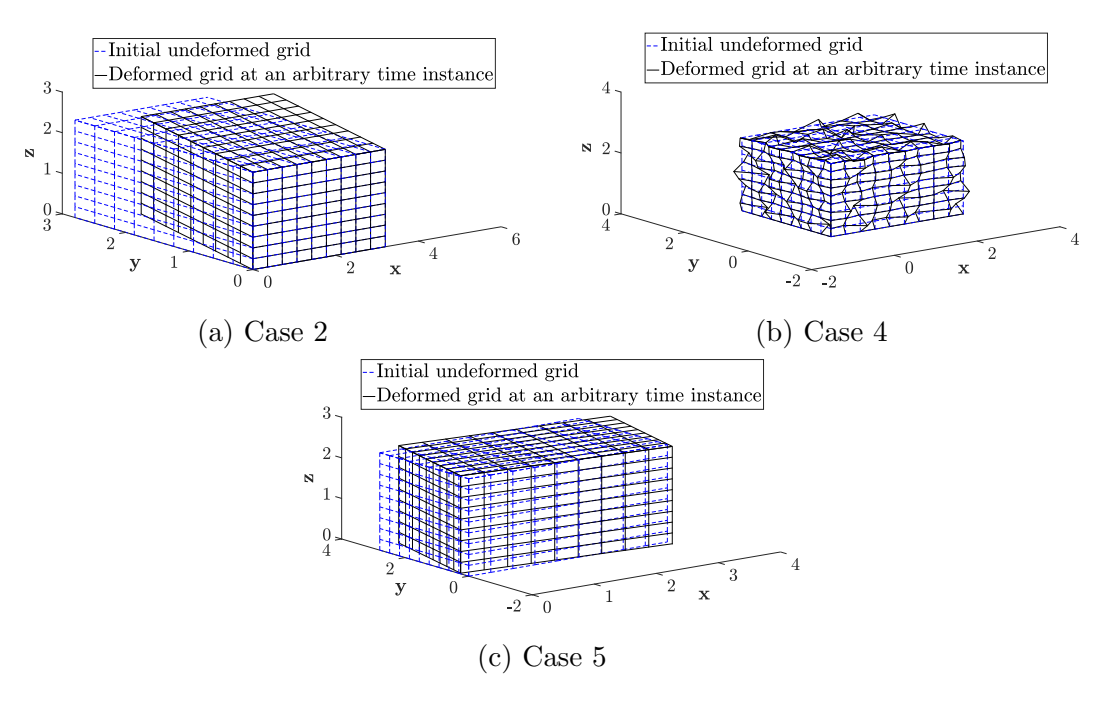


Figure 4–1: Mesh deformations of the exterior grid points for cases 2, 4 and 5 at an arbitrary chosen time step

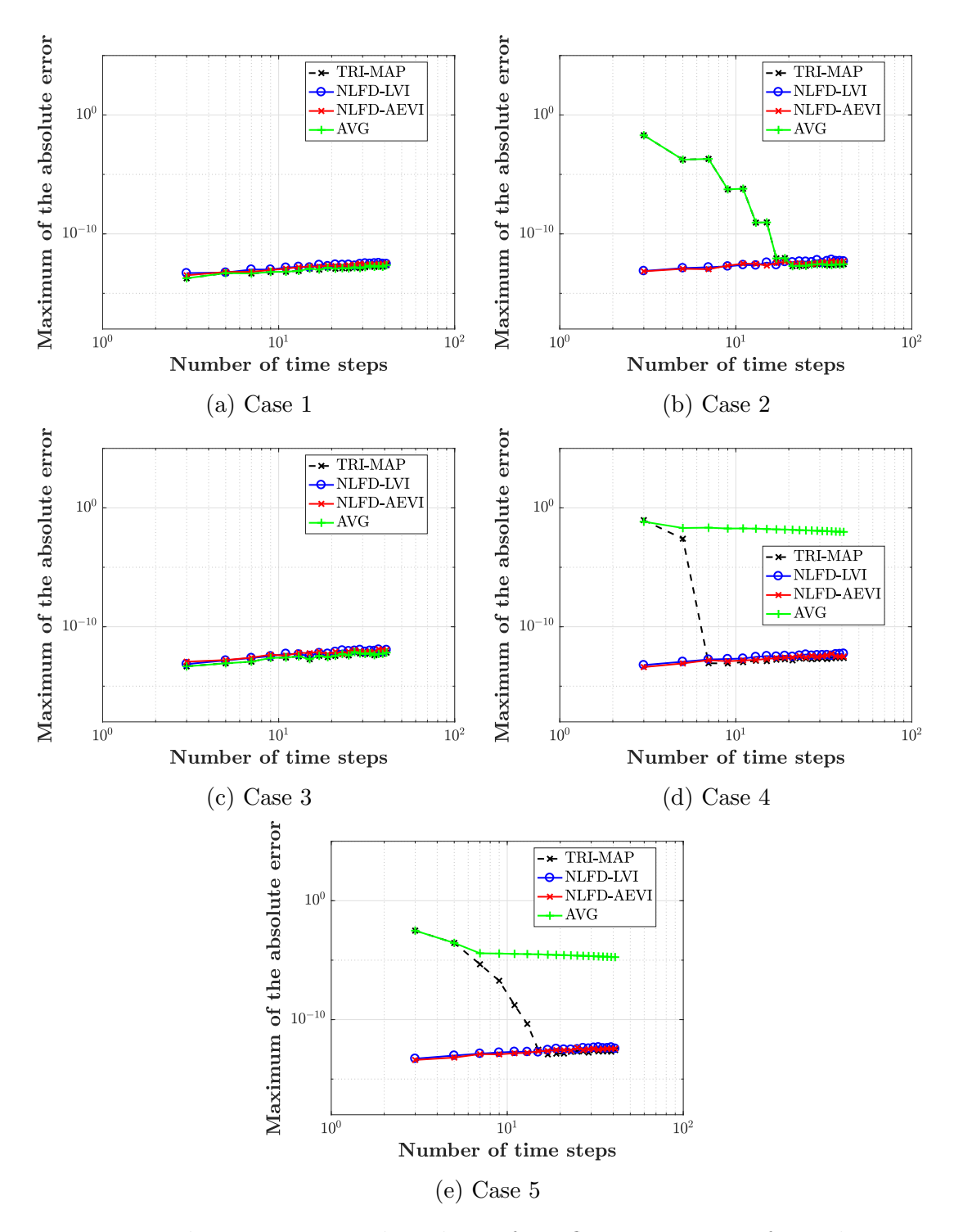


Figure 4–2: Relative error regarding the uniform flow preservation for each test case

increments is equal to the temporal derivative of the cell volume evaluated in the frequency domain (equation (4.2)).

It is also observed that using the (TRI-MAP) integrated face mesh velocities preserves uniform flow and thus satisfies the GCL given a sufficient number of harmonics (see cases 2, 4 and 5) which is expected. Its rate of convergence should be exactly the same as the rate of convergence of the temporal derivative of the cell volume in the Fourier space. This is verified in the next section.

4.4 Comparison of the integrated face mesh velocities to the reference value

The results are shown on Figures 4–3 through 4–8. It is important to note that for all figures, the graph (a) refers to equation (4.3) as the function of the number of time steps and is not the sum of the graphs from (b), (c) and (d) which refer to equation (4.4). The errors that appear on the y-axis of the figures are the max norm between the investigated approaches, both NLFD-based and AVG and the reference approach (TRI-MAP).

Regarding the comparison of the *sum of the* integrated face mesh velocities (IFMV) to the NLFD temporal derivative of the volume from Figures 4–3(a) through Figure 4–8(a), the results show that the sum of the IFMV computed with the methods NLFD-LVI, NLFD-AEVI and TRI-MAP converge to the expected values for all cases while the AVG method provides the correct values only for cases 1 through 3 and yields a constant absolute error above 10^{-5} for cases 4 and 5. Recall that the maximum error in the sum of the IFMV is a measure of the level to which GCL is satisfied as given in the semi-discrete GCL equation (3.5). Hence the NLFD-based approaches prove to satisfy the GCL for all considered grid deformation and for any

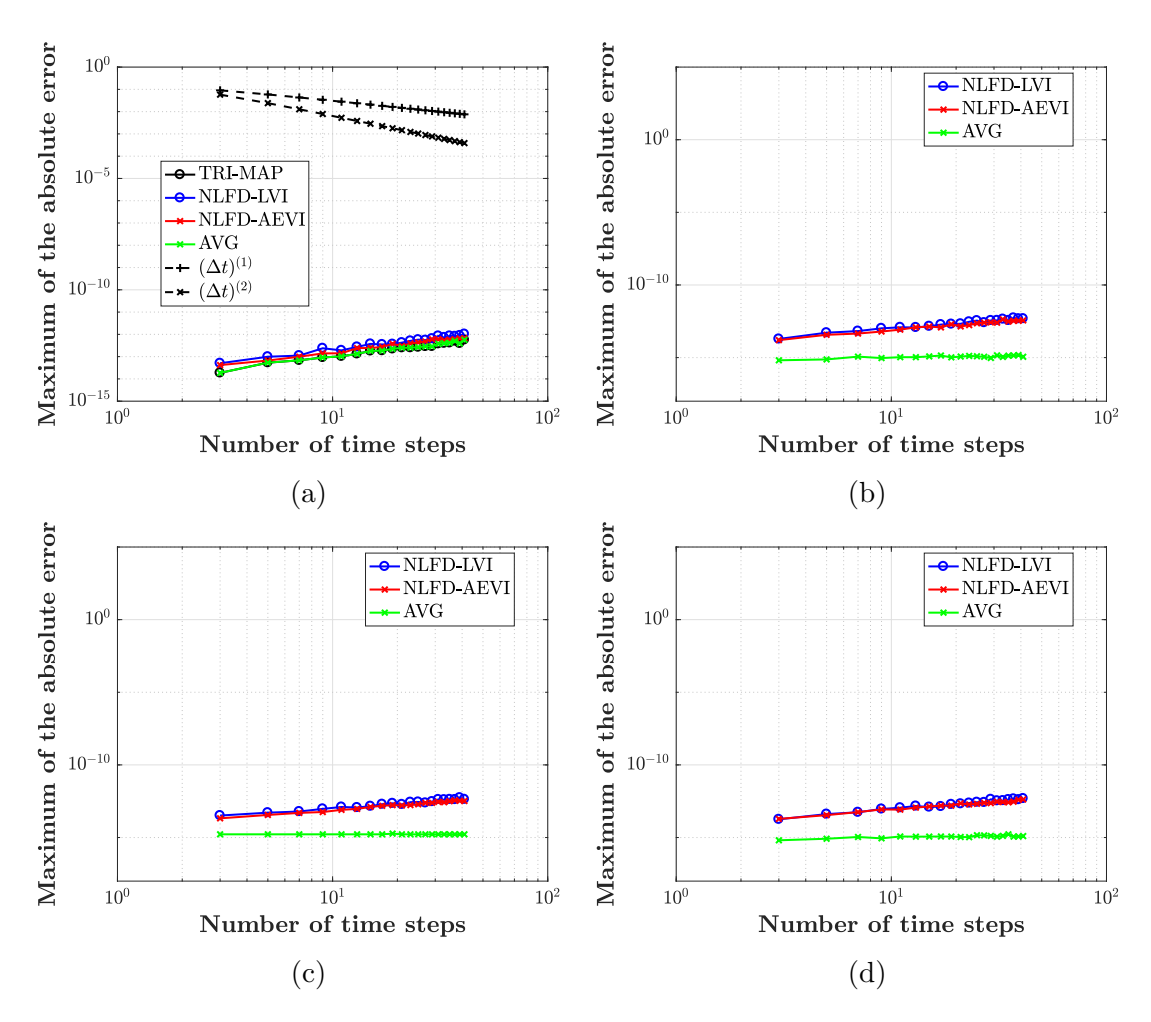


Figure 4–3: Case 1: (a) Comparison of the sum of the integrated face mesh velocities to the NLFD temporal derivative of the volume (b) Comparison of the individual integrated face mesh velocity to the reference values (TRI-MAP) in the x direction (c) in the y direction (d) in the z direction

number of harmonics which is expected by design. The reference approach (TRI-MAP) satisfies this requirement exactly for linear deformation cases as shown for Cases 1 (Figure 4–3(a)) and 4 (Figure 4–7(a)) for any number of harmonics and converged spectrally for non-linear deformation cases (Cases 2, 3, and 5). The spectral rate of convergence is observed compared to the first-order backward finite-difference ($\Delta t^{(1)}$) and second-order centered finite-difference ($\Delta t^{(2)}$) approximating the temporal derivative of the cell volume. As expected, this rate of convergence is found to be similar for the preservation of uniform flow using the reference TRI-MAP method. However, the AVG approach is not designed to enforce the GCL, it is only an approximation based on the mesh velocities and face metrics and hence for the cases considered herein, the method proved to ensure the GCL with an accuracy up to 10^{-5} .

A comparison of the *individual* integrated face mesh velocities for each direction reveals the limits and provides interesting insights of the investigated approaches. Two primary observations can be made. First, the NLFD based approaches converge at most at second order as expected based on Corollary 3.3.7, if the mesh deformation along the observed direction is non-linear. For Cases 2, 3, and 5, the mesh deformation in both the x-and y-directions are non-linear as shown in subfigures (b) and (c) of Figures 4–5, 4–6, and 4–8. One exception is the spectral rate of convergence for the y-direction in Case 2. These results can be explained by analyzing in details the mesh movement. Since the motion is in two dimensions, let us consider a constant z plane, then the deformation of any cell can be represented as shown in Figure 4–4. We observe that in the y-direction, the area swept by the

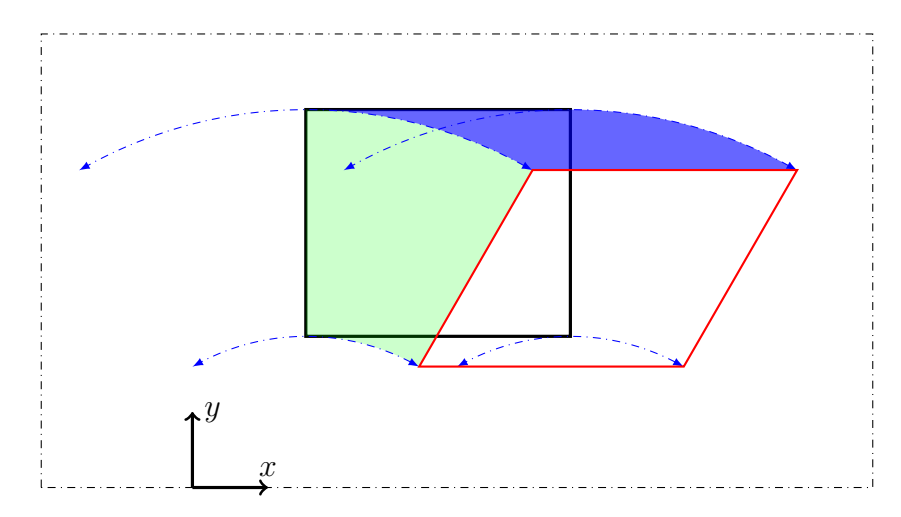


Figure 4–4: Two-dimensional projection of the motion in case 2 for one cell: the exact volumetric increment in the x direction is filled in clear green and in dark blue in the y direction. The blue dashed dot arrows show the paths of the vertices.

faces can be exactly evaluated using a linear approximation of the curved boundaries shown in blue. Therefore in the y-direction, the volumetric increments are exactly computed and the individual IFMV are correctly computed using either the NLFD-LVI or NLFD-AEVI methods once the temporal derivative operator is converged in Fourier space. In the x-direction, a linear approximation is insufficient to compute exactly the volumetric increments thus the NLFD-AEVI method converges at an order between one and two as stated in Corollary 3.3.7.

Second, even if the numerical scheme enforces the GCL by preserving uniform flow, the employed method may not converge to the correct integrated face mesh velocities. The method based on the approximation of the exact volumetric increment (NLFD-AEVI) is found to be converging toward the reference values at an order between one and two in the worst test cases considered here (4 & 5). This is consistent with the derivation of the error from Section 3.3.2 and the resulting Corollary 3.3.7.

The NLFD-LVI and AVG methods may present significant inaccuracies depending on the mesh deformation.

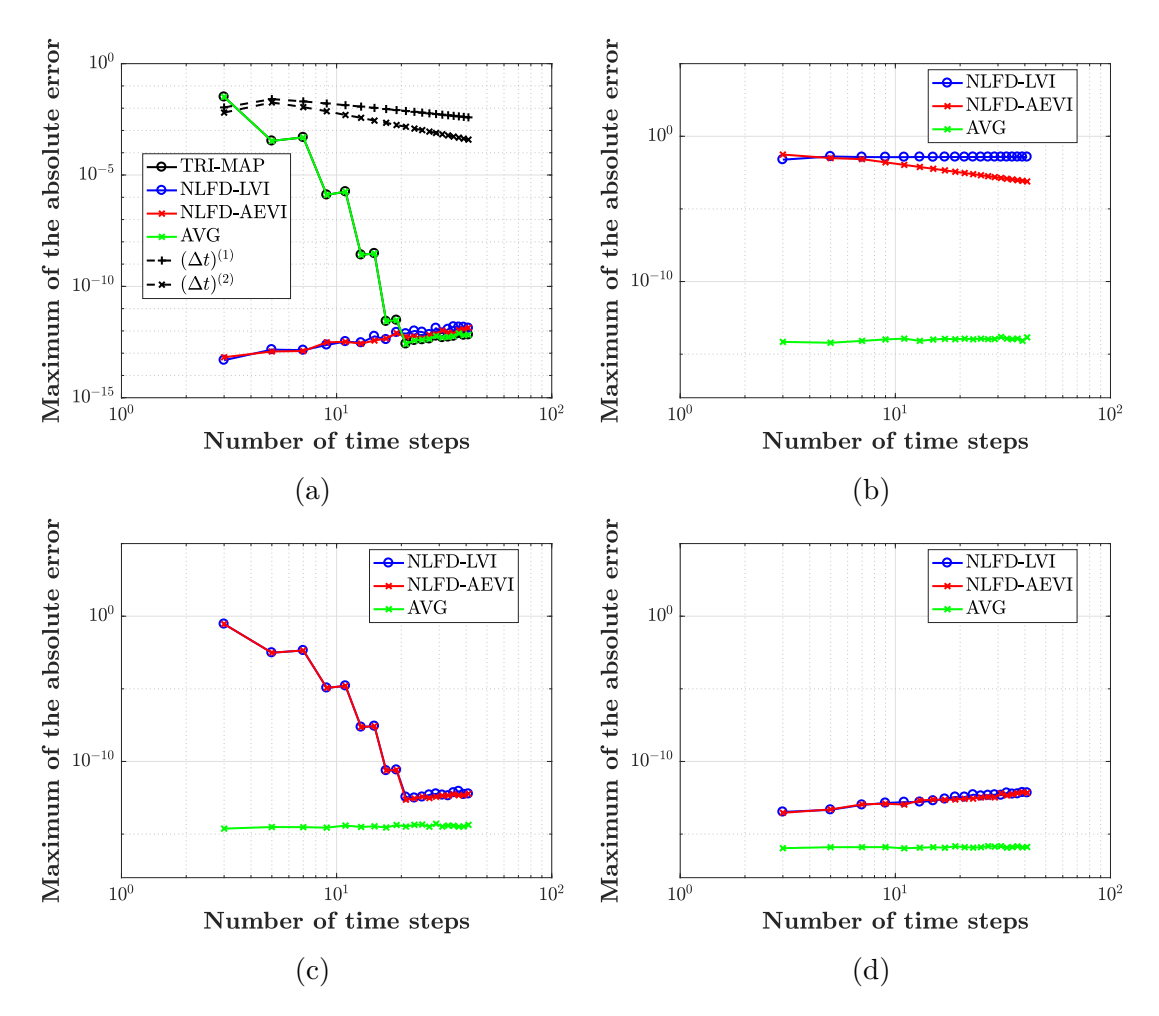


Figure 4–5: Case 2: (a) Comparison of the sum of the integrated face mesh velocities to the NLFD temporal derivative of the volume (b) Comparison of the individual integrated face mesh velocity to the values (TRI-MAP) in the x direction (c) in the y direction (d) in the z direction

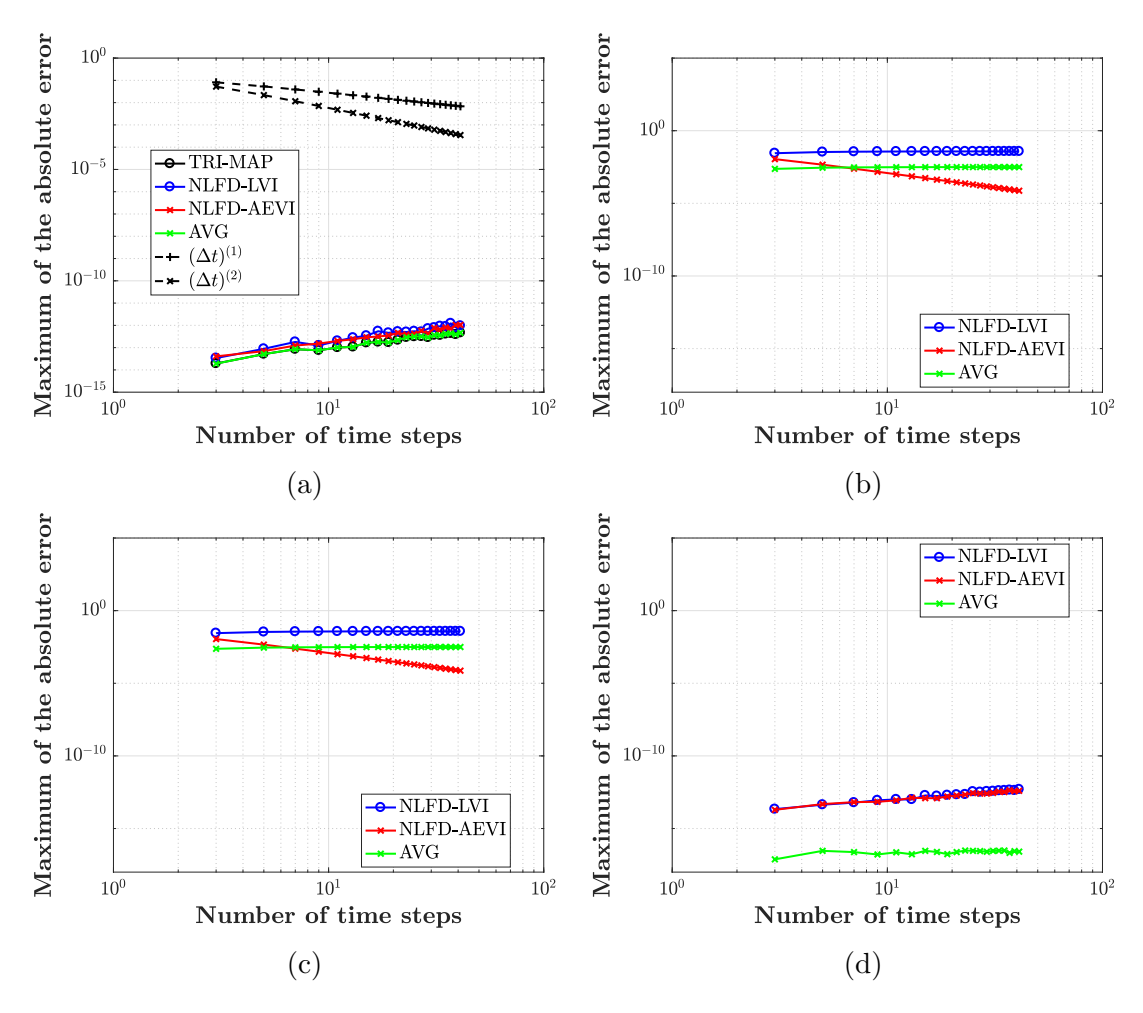


Figure 4–6: Case 3: (a) Comparison of the sum of the integrated face mesh velocities to the NLFD temporal derivative of the volume (b) Comparison of the individual integrated face mesh velocity to the values (TRI-MAP) in the x direction (c) in the y direction (d) in the z direction

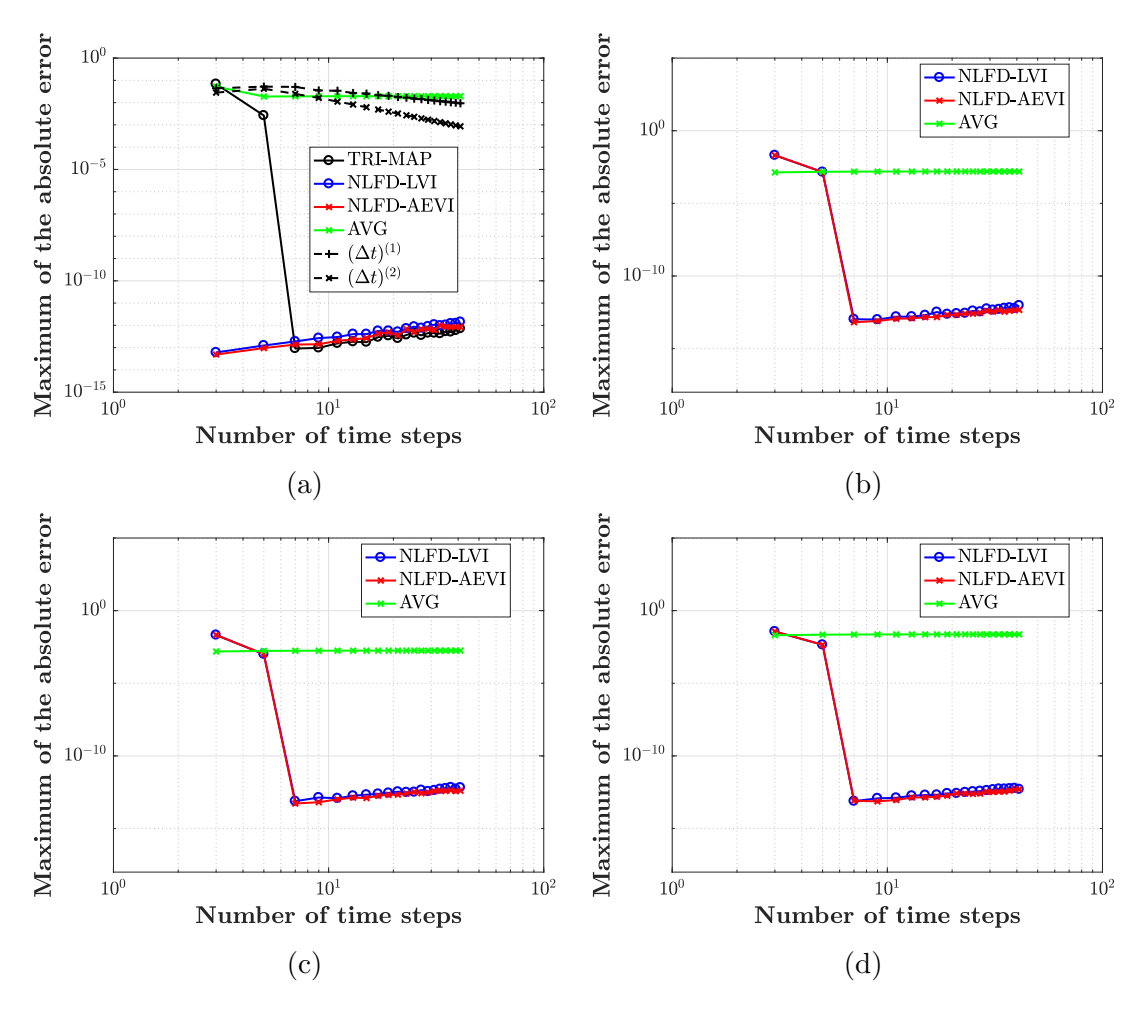


Figure 4–7: Case 4: (a) Comparison of the sum of the integrated face mesh velocities to the NLFD temporal derivative of the volume (b) Comparison of the individual integrated face mesh velocity to the values (TRI-MAP) in the x direction (c) in the y direction (d) in the z direction

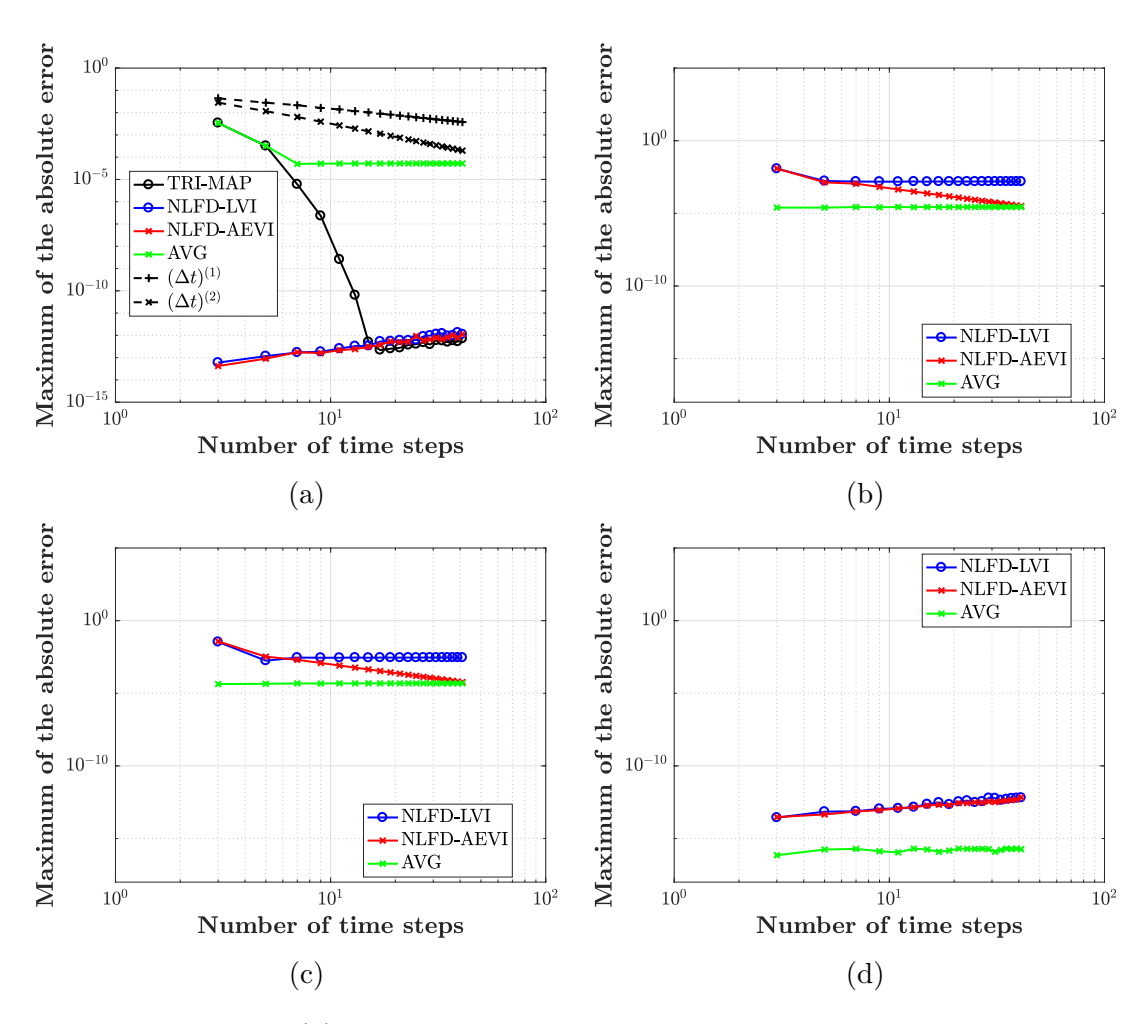


Figure 4–8: Case 5: (a) Comparison of the sum of the integrated face mesh velocities to the NLFD temporal derivative of the volume (b) Comparison of the individual integrated face mesh velocity to the values (TRI-MAP) in the x direction (c) in the y direction (d) in the z direction

4.5 Time-Spectral Method

The numerical results for the Time-Spectral method are the same as that shown for NLFD-LVI and NLFD-AEVI depending on which approach is retained to compute the volumetric increments. For this reason, the graphs are not reproduced herein. The comparisons and conclusions derived for the NLFD discretization hold for the Time-Spectral method as well.

4.6 Discussion

The limits of the previous method of Tardif and al. [37] (NLFD-LVI) were clarified and demonstrated numerically and a modified approach (NLFD-AEVI) has been presented that ensures the satisfaction of the Geometric Conservation Law for a flow solver based on either the NLFD or Time-Spectral discretization of the ALE formulation of the Navier-Stokes equations. The methods NLFD-AEVI and NLFD-LVI aim to satisfy the GCL by computing the integrated face mesh velocities according to the numerical discretization of the flow solver and take as input the face volumetric increments. The accuracy of the methods was shown to be highly dependent on the computation of the correct volumetric increments and in the worst cases considered converged at first-to-second-order for the NLFD-AEVI approach (Corollary 3.3.7) or zeroth-order for the NLFD-LVI procedure. The integrated face mesh velocities themselves may not converge to the correct values as demonstrated in our numerical test. Although the approaches have been verified to preserve uniform flow for any number of harmonics; such a low order of accuracy defeats the purpose of spectral in time methods. Hence an alternate novel approach has been developed based on a trilinear mapping between the physical domain and the computational space which allows the evaluation of the exact cell volume and integrated face mesh velocities. The disadvantage of this method is that it is not consistent with the discretization of the flow solver, meaning that freestream preservation is not satisfied for any number of harmonics as it is with the modified approach, NLFD-AEVI. However such inconvenience is compensated by its spectral rate of convergence, which is sufficient to ensure the satisfaction of the GCL and to preserve uniform flow.

CHAPTER 5 Two-dimensional aerodynamic simulations

In this chapter, we present the results of aerodynamic simulations employing the different developed methods. The RBF dynamic mesh deformation as well as the different methodologies to compute the integrated face mesh velocities were implemented in the in-house adaptative NLFD two-dimensional finite volume solver originally developed by Mosahebi and al. [28–31]. Instead of employing artificial dissipation, a Roe flux difference splitting scheme [36] is used to compute the convective fluxes. A Lower-Upper Symmetric-Gauss-Seidel (LU-SGS) implicit scheme [4] is used to solve the equation in pseudo-time (2.20). Since the current flux adjustment approach for temporal-mismatched control volumes in the adaptive approach renders the scheme non-conservative, the adaptation was turned off for all simulations.

In this section, results for aerodynamic computations of a plunging and/or pitching cylinder and a NACA0012 airfoil are presented. An O-grid topology is used for the cylinder mesh with 256x128 cells and a C-grid topology for the NACA0012 mesh with the same dimensions. The ratio between the farfield distance to the cylinder diameter D or the airfoil chord c is 200. All RBF points in the farfield are fixed (zero displacements).

It should be noted that the current solver is only able to resolve one dominant frequency in the domain which is specified for plunging cases by specifying the Strouhal number $St = \frac{2h_0f}{V_{\infty}}$ and the reduced frequency for pitching motions $\kappa = \frac{\pi fc}{V_{\infty}}$, with h_0

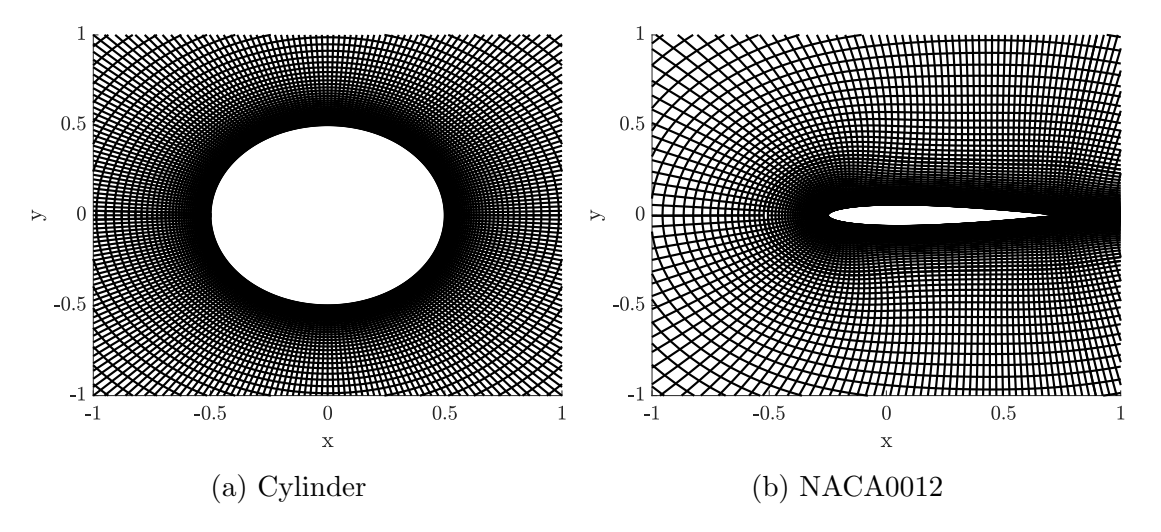


Figure 5–1: Near resolution of the undeformed meshes employed for the simulations

the plunging amplitude, c the chord or diameter of the body, V_{∞} the freestream velocity and $f = \frac{1}{T}$ the frequency of oscillation corresponding to the period T. The chord and diameter are both taken to be unitary. The Prandtl number Pr and the freestream temperature are held constant for all simulations and respectively taken equal to 0.75 and 300 K.

The following notations are adopted for the aerodynamic coefficients: stagnation pressure coefficient C_{ps} , total lift coefficient C_L , total drag coefficient C_D , pressure drag coefficient $C_{D,p}$ and skin friction drag coefficient $C_{D,v}$. The level to which the GCL is satisfied is measured by computing the maximum absolute difference between the NLFD temporal derivative of the volume from the flow solver and the sum of the integrated mesh velocities deduced from the various techniques and is denoted as \mathcal{E}_{GCL} . Flow solver residual is converged to a sufficient level to ensure that the aerodynamic coefficients are only impacted by the GCL error. In addition,

the values of the IFMV deduced from the NLFD-based methods are compared to the bilinear mapping approach which serves as the reference method in the x and y directions and denoted respectively as $\mathcal{E}_{IFMV,x}$ and $\mathcal{E}_{IFMV,y}$.

5.1 Plunging cylinder

As a first test case, a plunging cylinder in the y-direction is considered, the displacements of the RBF points at the surface of the cylinder are prescribed as follows:

$$\begin{cases} s_x(t) = 0, \\ s_y(t) = h_0 \sin(\omega t), \end{cases}$$
 (5.1)

where h_0 is the amplitude of the heaving motion. The results are compared to Mosahebi and al. [29] with $\frac{h_0}{D} = 0.2$, $M_{\infty} = 0.3$, $Re_{\infty} = 100$, and St = 0.16704. The frequency was chosen to be equal to the vortex shedding frequency computed for the stationary case. Table 5–1 presents the verification of the GCL and the convergence of the IFMV in each direction, the mean values of the drag coefficients are presented in Table 5–2 for different number of harmonics. The flow solver converged to machine accuracy for all cases.

Methods	\mathcal{E}_{GCL}	$\mathcal{E}_{IFMV,x}$	$\mathcal{E}_{IFMV,y}$
NLFD-LVI	$\leq 10^{-13}$	$\leq 10^{-12}$	$\leq 10^{-12}$
NLFD-AEVI	$\leq 10^{-13}$	$\leq 10^{-12}$	$\leq 10^{-12}$
BI-MAP	$\leq 10^{-12}$	N.A.	N.A.

Table 5–1: Level of satisfaction of the GCL and convergence of the integrated face mesh velocities in the case of the plunging cylinder using $1 \le N \le 7$ harmonics in the DFT

It is observed that the GCL and the IFMV have converged to machine accuracy for any number of harmonics and for all three methods. This result is consistent since

Methods	$\overline{C_{D,p}}$	$\overline{C_{D,v}}$	$\overline{C_D}$
All methods (1 harmonic)	1.16631	0.36754	1.52863
All methods (2 harmonics)	1.25273	0.38537	1.63810
All methods (3 harmonics)	1.23544	0.38297	1.61841
All methods (4 harmonics)	1.23329	0.38242	1.61571
All methods (5 harmonics)	1.23546	0.38283	1.61829
Mosahebi and al. [29] (10 modes)	1.22992	0.38044	1.61035

Table 5–2: Mean values of the drag coefficients in the case of the plunging cylinder with $M_{\infty} = 0.3$, $Re_{\infty} = 100$ and St = 0.16704.

the motions of the RBF points at the surface of the body are linear with the same amplitude and direction, hence in this specific case the three methods are equivalent and expected to produce the same results. As a consequence, the computed aerodynamic coefficients, as listed in Table 5–2, are identical for all methods within the accuracy of the flow solver. Given the number of modes employed in our simulations, the results are consistent with Mosahebi and al. [29]. However, it must be noted that even if one harmonic is sufficient to satisfy GCL at machine accuracy, the computation of the mean drag coefficients up to the second digit requires additional harmonics as shown in Figure 5–2.

The investigations of Young and al. [41, 42] and Yang [40] showed that the behavior of the drag coefficient is primarily due to the shedding of vortices. Vortices may appear either at the trailing edge and diffuse in the wake or at the leading edge and convect downstream before separating from the airfoil and diffuse into the downstream wake. These vortices contribute to the wake and influence the drag. The instantaneous total drag coefficient follows the temporal evolution from Figure 5–2b.

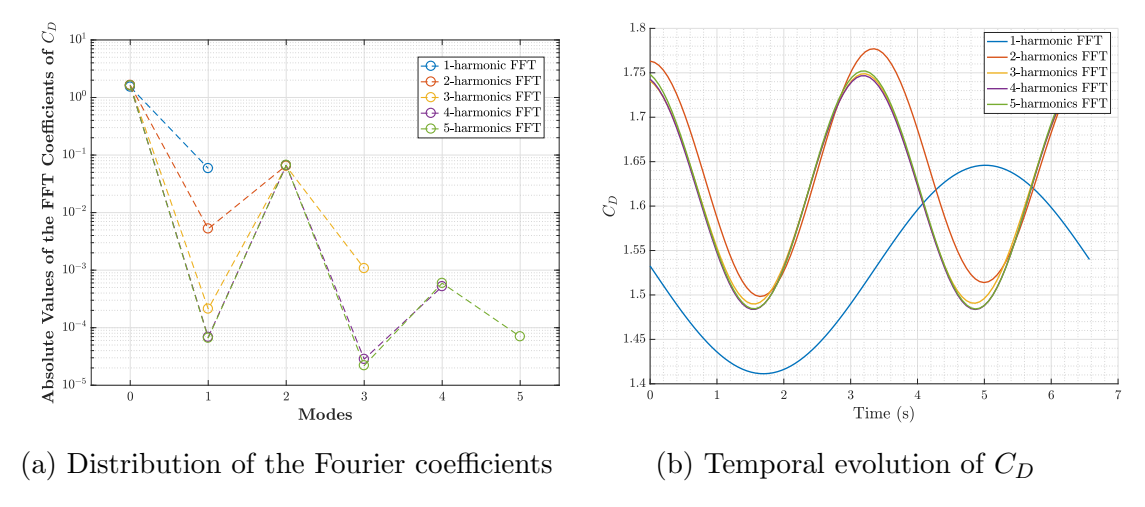


Figure 5–2: Total drag coefficient analysis for a plunging cylinder

5.2 Pitching cylinder

For the second case, a pitching cylinder about its center is considered with an angle varying from -10° to $+10^{\circ}$. The freestream Mach number, Reynolds number and the reduced frequency are chosen from [28], M = 0.3, Re = 100 and $\kappa = 0.52477$. The level to which GCL is satisfied is presented on Figure 5–3(a) and the convergence of the IFMV to the reference values in each direction on Figure 5–3(b) and Figure 5–3(c). Contrary to the previous case, the GCL is no longer statisfied for any number of harmonics using the BI-MAP method which converges at a spectral rate. The limits of the NLFD-based methods are observed when computing the integrated face mesh velocities; especially in the x direction where for solutions larger than three harmonics, the convergence of the NLFD-LVI approach reaches a threshold at 10^{-5} to 10^{-6} and the NLFD-AEVI method converges at first-to-second order. In the y direction, both methods converge at a spectral rate.

The mean values of the aerodynamic coefficients are presented in Table 5–3 and the drag polar (C_D versus C_L) are demonstrated in Figure 5–4, for 2 and 5 modes. Simulations with only 1-harmonic did not converge to a residual below the level of convergence of either the GCL or the IFMV and thus are not presented. For 2 and 5 modes, differences between the mean values of the aerodynamic coefficients begin to appear at the fifth decimal place and the relative gap between the different methods is always inferior to 0.01%. The results are still in good agreement with Mosahebi and al. [29]. As previously stated for the plunging cylinder even if one harmonic is sufficient to represent the motion of the mesh, additional modes are needed to correctly capture the instantaneous behavior of the total drag coefficient. In the industry, designer uncertainty goals for performance simulations on successive refined grids are usually up to ± 0.005 on the lift coefficient and ± 0.5 drag counts¹ on the drag coefficient [14]. Thus the differences herein on the mean total drag coefficient and maximum lift coefficient being respectively lower than one drag count and 0.01, they would not be considered worth further investigation.

 $^{^{1}}$ one drag count = 10^{-4} . C_{D}

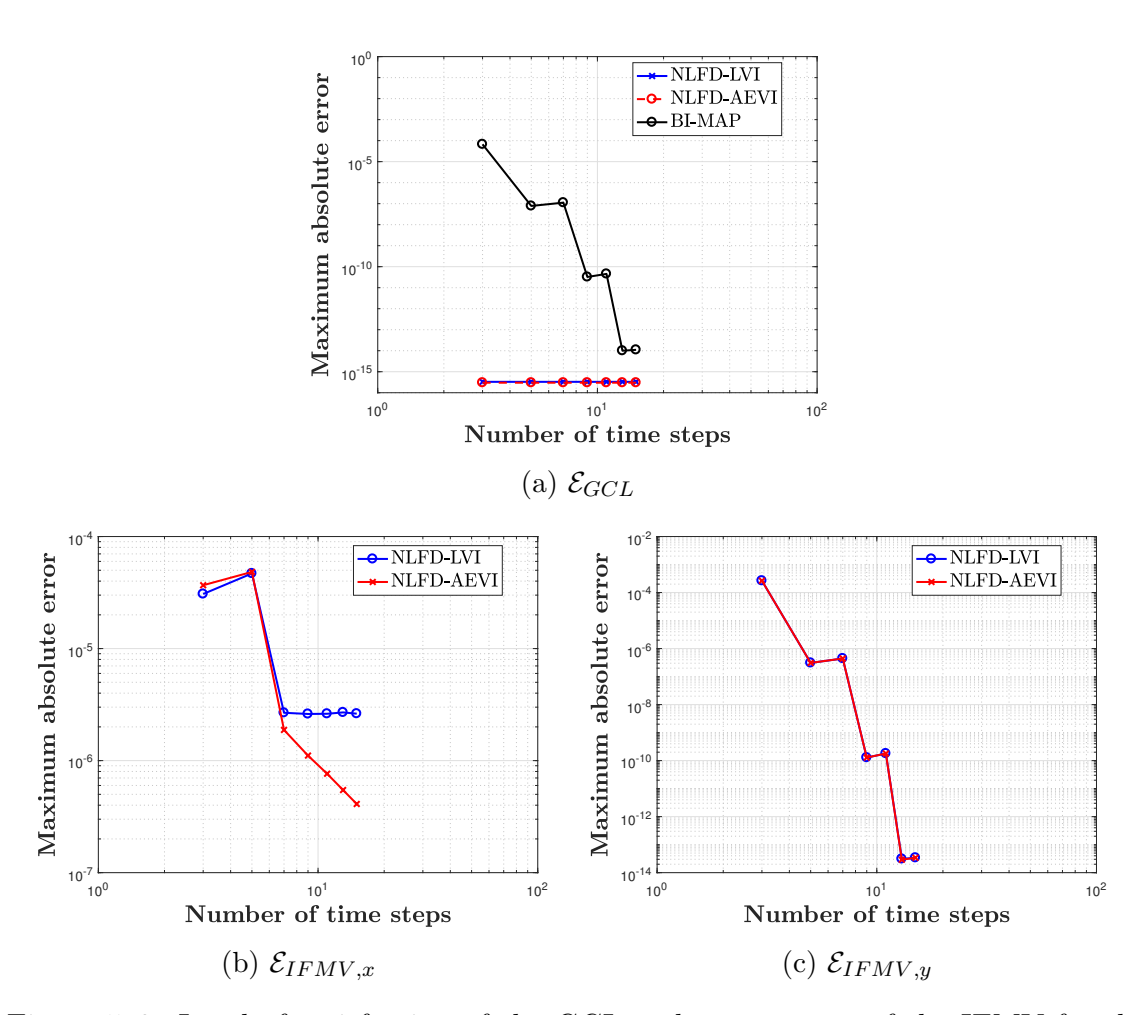


Figure 5-3: Level of satisfaction of the GCL and convergence of the IFMV for the pitching cylinder case

Methods	$\overline{C_{D,p}}$	$\overline{C_{D,v}}$	$\overline{C_D}$	$\overline{C_{ps}}$
NLFD-LVI (2 harmonics)	1.1031 <i>69</i>	0.354731	1.4579 <i>01</i>	1.033769
NLFD-AEVI (2 harmonics)	1.103187	0.354735	1.457922	1.033765
BI-MAP (2 harmonics)	1.103186	0.354738	1.457925	1.033771
NLFD-LVI (5 harmonics)	1.107 <i>321</i>	0.355542	1.462864	1.035812
NLFD-AEVI (5 harmonics)	1.107283	0.355535	1.4628 <i>19</i>	1.035823
BI-MAP (5 harmonics)	1.107267	0.355532	1.4628 <i>00</i>	1.035829
Mosahebi and al. [29] (10 harmonics)	1.11386	0.356830	1.47069	1.03252

Table 5–3: Mean values of the drag coefficients and maximum lift coefficient in the case of the pitching cylinder.

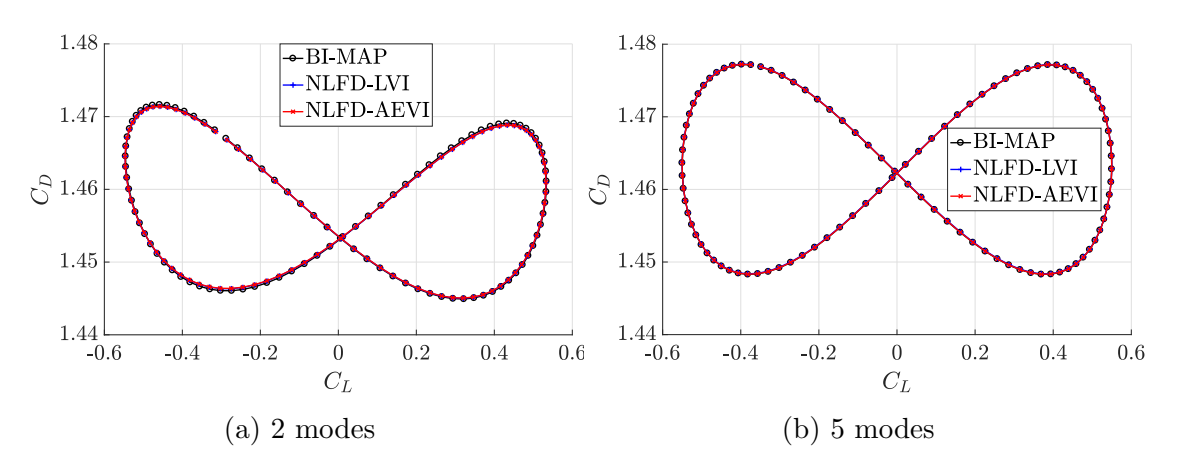


Figure 5–4: Drag polar \mathcal{C}_D vs \mathcal{C}_L for the pitching cylinder case

5.3 Plunging NACA0012 airfoil

In this section, a plunging NACA0012 airfoil in the y-direction is considered. The results are compared to Allaneau and al. [1] with $\frac{h_0}{D} = 0.08$, $M_{\infty} = 0.2$, $Re_{\infty} = 1850$ and St = 0.288. Table 5–4 presents the verification of the GCL and the convergence of the IFMV in each direction. The mean values of the drag coefficients are presented in Table 5–5 for different number of harmonics and the instantaneous behavior of the total lift and total drag on Figure 5–5.

Methods	\mathcal{E}_{GCL}	$\mathcal{E}_{IFMV,x}$	$\mathcal{E}_{IFMV,y}$
NLFD-LVI	$\leq 10^{-13}$	$\leq 10^{-13}$	$\leq 10^{-13}$
NLFD-AEVI	$\leq 10^{-13}$	$\leq 10^{-13}$	$\leq 10^{-13}$
BI-MAP	$\leq 10^{-13}$	N.A.	N.A.

Table 5–4: Level of satisfaction of the GCL and convergence of the integrated face mesh velocities in the case of the plunging NACA0012 using $1 \le N \le 7$ harmonics in the DFT

Methods	$\overline{C_{D,p}}$	$\overline{C_{D,v}}$	$\overline{C_D}$
All methods (1 harmonic)	-0.01494	0.05105	0.03611
All methods (2 harmonics)	-0.01391	0.05267	0.03876
All methods (3 harmonics)	-0.01353	0.05306	0.03953
All methods (4 harmonics)	-0.01392	0.05323	0.03938
All methods (5 harmonics)	-0.01337	0.05323	0.03986

Table 5–5: Mean values of the drag coefficients in the case of the plunging NACA0012 with $M_{\infty}=0.2,\ Re_{\infty}=1850$ and St=0.288.

Similar to the plunging cylinder case, it is observed that the GCL and the IFMV converge to machine accuracy for any number of harmonics and for all three methods, which is consistent for a linear motion with identical amplitudes and directions for the RBF points at the surface of the body. The computed average aerodynamic

coefficients are identical for all methods within the accuracy of the flow solver as well as the instantaneous behavior of the total lift and total drag which are consistent with the results of direct numerical simulation (DNS) provided by Allaneau and al. [1]. and Young and al. [42] who investigated the aerodynamic forces on a flapping airfoil.

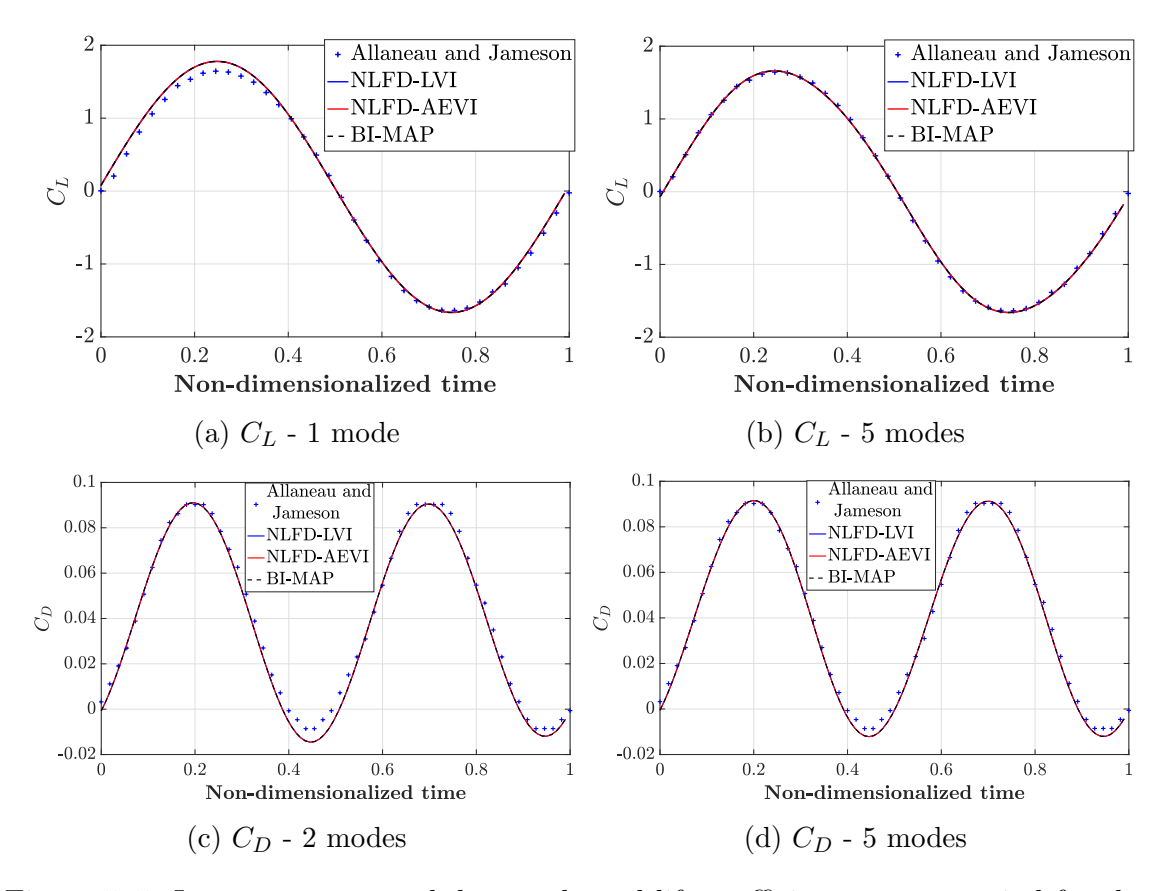


Figure 5–5: Instantaneous total drag and total lift coefficients over a period for the plunging NACA0012 case

5.4 Pitching NACA0012 airfoil

For the final test case, a pitching motion of the NACA0012 airfoil about the quarter chord is considered where two pitching angles are considered $\pm 5^{\circ}$ and $\pm 20^{\circ}$ with a reduced frequency κ respectively equal to 2 and 3.

5.4.1 Pitching NACA0012 at $\pm 5^{\circ}$ angle and $\kappa = 2$

The mean angle of attack is zero while the pitching angle varies from -5° to $+5^{\circ}$. The freestream Mach number, Reynolds number and the reduced frequency are chosen from [28], $M_{\infty} = 0.2$, $Re_{\infty} = 1100$ and $\kappa = 2$. The level to which GCL is satisfied is presented on Figure 5–6(a) and the convergence of the IFMV to the reference values in each direction on Figure 5–6(b) and Figure 5–6(c). The results are similar to the pitching cylinder case, the GCL is satisfied with all NLFD-based methods while the (BI-MAP) converges at a spectral rate. As for the integrated face mesh velocities, the results in the y direction are herein similar to the x direction, the convergence of the (NLFD-LVI) approach reaches a threshold close to 10^{-6} and the (NLFD-AEVI) method converges at first-to-second order beyond 3 harmonics.

The mean values of the aerodynamic coefficients are presented in Table 5–6 and drag polar is shown in Figure 5–7, for 1, 2 and 5 modes. For the 2 and 5 mode cases the differences between the mean values of the aerodynamic coefficients begin to appear at the third decimal for the drag coefficients and the second decimal for the maximum lift coefficient. The relative gap between the different methods is always inferior to 0.01% for the drag coefficients and 0.5% for the maximum lift coefficient. Differences are observed compared to Mosahebi [27] and Pedro and al. [34], which are due to the insufficient number of harmonics considered to represent the unsteadiness

of the flow with at most 5 harmonics. The graph of instantaneous C_D vs C_L shows significant differences between the NLFD-based methods and the BI-MAP method employing only one harmonic which drastically reduce with two or more harmonics. The differences between the methods are still being lower than one drag count and thus do not deserve further investigation for industrial applications.

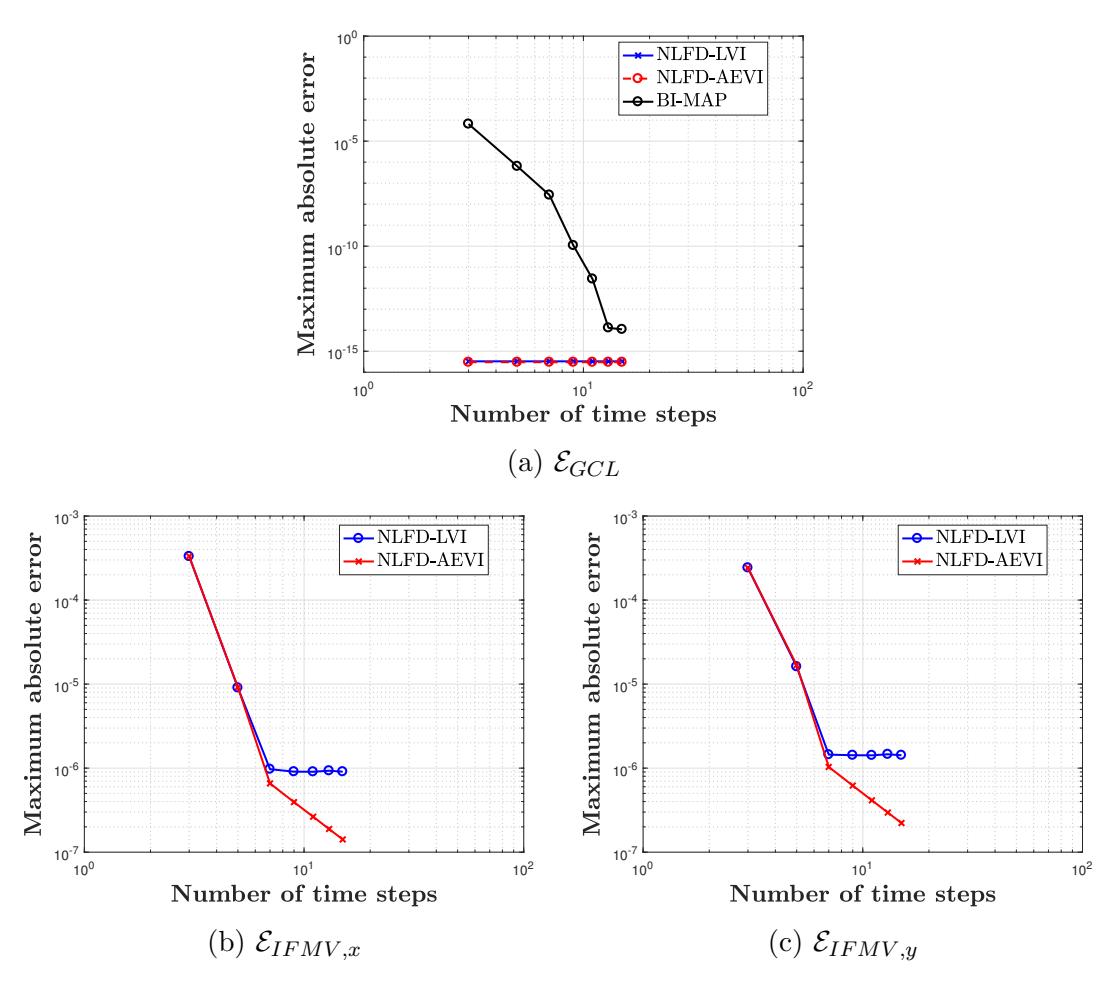


Figure 5–6: Level of satisfaction of the GCL and convergence of the IFMV for the pitching NACA0012 case at $\pm 5^{\circ}$ and $\kappa=2$

Methods	$\overline{C_{D,p}}$	$\overline{C_{D,v}}$	$\overline{C_D}$	$\max(C_L)$
NLFD-LVI (1 harmonic)	0.022492	0.085322	0.107815	0.82104
NLFD-AEVI (1 harmonic)	0.022506	0.085295	0.107802	0.81741
BI-MAP (1 harmonic)	0.022588	0.085351	0.107939	0.81715
NLFD-LVI (2 harmonics)	0.024502	0.086 <i>092</i>	0.110594	0.79241
NLFD-AEVI (2 harmonics)	0.02450 3	0.086089	0.110592	0.79224
BI-MAP (2 harmonics)	0.024501	0.086102	0.110604	0.79199
NLFD-LVI (5 harmonics)	0.024827	0.086247	0.111074	0.77927
NLFD-AEVI (5 harmonics)	0.024824	0.0862 <i>53</i>	0.111078	0.779 <i>30</i>
BI-MAP (5 harmonics)	0.024824	0.086256	0.1110 80	0.77923
Mosahebi [27] (adaptive methods)	0.0280	0.0859	0.1139	0.7201
Pedro and al. [34]	0.0276	0.0857	0.1132	0.7107

Table 5–6: Mean values of the drag coefficients and maximum lift coefficient in the case of the pitching NACA0012 airfoil at $\pm 5^{\circ}$ and $\kappa = 2$

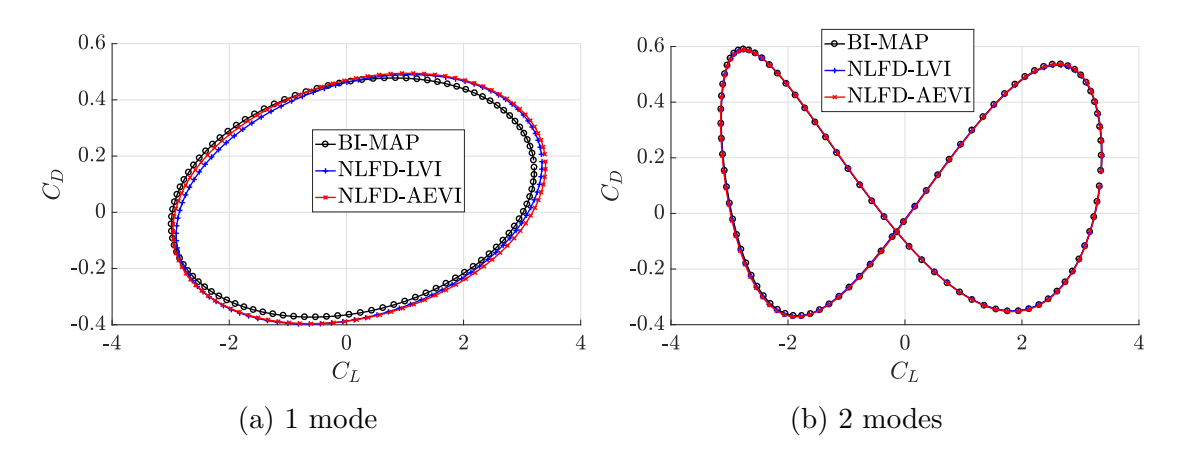


Figure 5–7: Drag polar C_D vs C_L for the NACA0012 airfoil case at $\pm 5^\circ$ and $\kappa=2$

5.4.2 Pitching NACA0012 at $\pm 20^{\circ}$ angle and $\kappa = 3$

The pitching angle variation is increased to $\pm 20^{\circ}$ and the reduced frequency to $\kappa = 3$ while all other parameters remain unchanged. The convergence of the density residual for N = 5 harmonics is presented on Figure 5–8(a). The level to which GCL is satisfied is presented on Figure 5–8(b) and the convergence of the IFMV to the reference values in each direction on Figure 5–8(c) and Figure 5–8(d). As expected, the convergence of the GCL is still at spectral rate and similarly the IFMV using the (NLFD-AEVI) method still converge at first-to-second order, however for both quantities additional harmonics are needed to reach an equivalent level of convergence compared to the $\pm 5^{\circ}$ pitching case. The convergence of the IFMV using the (NLFD-LVI) method reaches a threshold at 10^{-3} to 10^{-5} which is higher than the previous case. These observations are consistent since the amplitude of the pitching motion is larger, thus the non-linearity of the mesh deformation is more significant and places an additional challenge to the convergence of the GCL and IFMV.

Methods	$\overline{C_{D,p}}$	$\overline{C_{D,v}}$	$\overline{C_D}$	$\max(C_L)$
NLFD-LVI (5 harmonics)	-0.06 783	0.0 8980	0.02 <i>196</i>	10.4 <i>643</i>
NLFD-AEVI (5 harmonics)	-0.06 753	0.09134	0.02 <i>381</i>	10.4 <i>610</i>
BI-MAP (5 harmonics)	-0.06577	0.09167	0.02 <i>590</i>	10.4576

Table 5–7: Mean values of the drag coefficients and maximum lift coefficient in the case of the pitching NACA0012 airfoil at $\pm 20^{\circ}$ and $\kappa = 3$

The mean values of the drag coefficients and the maximum lift for the pitching NACA0012 airfoil at $\pm 20^{\circ}$ are presented in Table 5–7 for 5 harmonics as well as the drag polar Figure 5–9. The level of convergence of the density residual for each mode was stopped below 10^{-7} (Figure 5–8(a)), since the level of convergence of the GCL

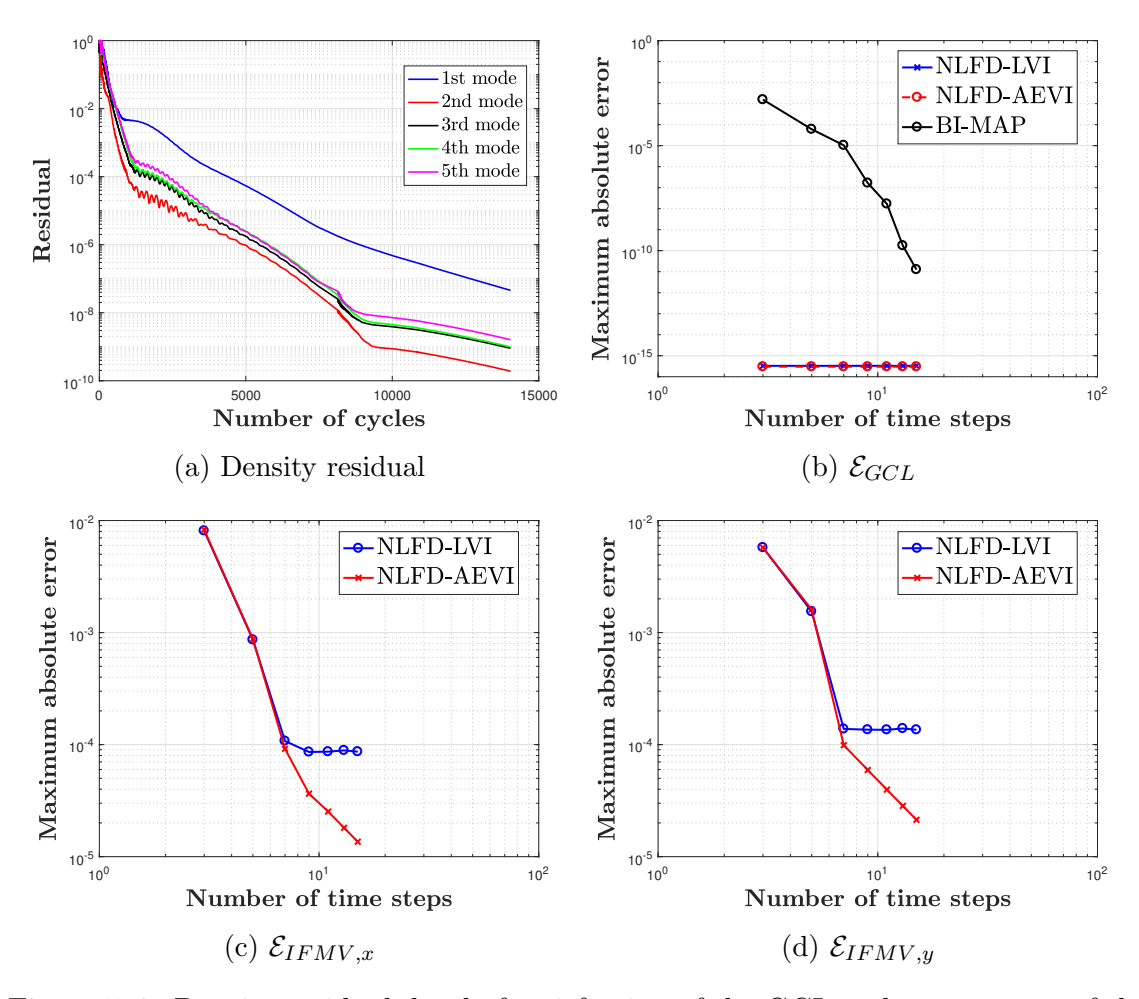


Figure 5–8: Density residual, level of satisfaction of the GCL and convergence of the IFMV for the pitching NACA0012 case at $\pm 20^{\circ}$ and $\kappa = 3$

is at 10^{-8} (Figure 5–8(b)) and the IFMV computed at machine accuracy for the BI-MAP method (Figures 5–8(c) and 5–8(d)) the values of the aerodynamic coefficients from the bi-mapping can be considered as reference. Absolute differences on the mean total drag coefficient of respectively 39.8 drag counts (NLFD-LVI) and 20.9 drag counts (NLFD-AEVI) are observed. These are much larger than the $\pm 5^{\circ}$ case and represent respectively 15.21% and 8.06% of relative gap. Such differences are much higher than one drag count and clearly shows the impact of having Integrated Face Mesh Velocities which converge at an order inferior to the one of the flow solver or the GCL. In addition, the analysis of the two components of the drag coefficient shows that the differences on the skin-friction drag are higher than on the pressure drag, a similar observation can be done for the previous $\pm 5^{\circ}$ pitching NACA0012 case (see Table 5–6) but not for the pitching cylinder case (see Table 5–3). The differences on the maximum lift coefficient are still lower than 0.01 and would not be worth further investigation. The velocity contours and streamlines are presented on Figure 5–11 at time instances t_0 , t_5 and t_{10} ; the vortices which cause the drag variation are visible at the leading edge and in the wake.

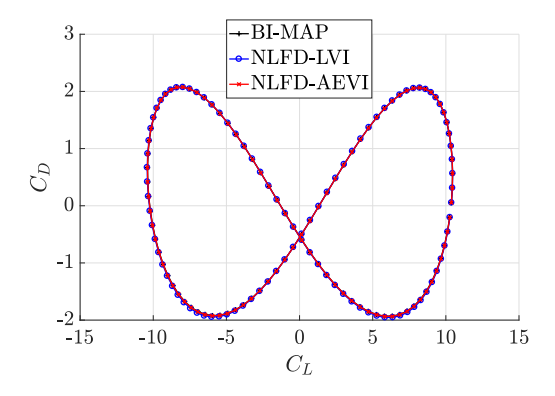


Figure 5–9: Drag polar C_D vs C_L for the NACA0012 airfoil case at $\pm 20^\circ$ and $\kappa = 3$

The absolute error distributions on the IFMV compared to the (BI-MAP) values in the x and y directions are presented on Figure 5–10 at a time instance $t_5 = \frac{5}{11}T$. The airfoil leading edge is positioned at $x_{LE} = -0.25$ and the trailing edge at $x_{TE} = 0.75$. The areas of maximum error begin at the trailing edge which is the RBF point with the largest prescribed motion amplitude.

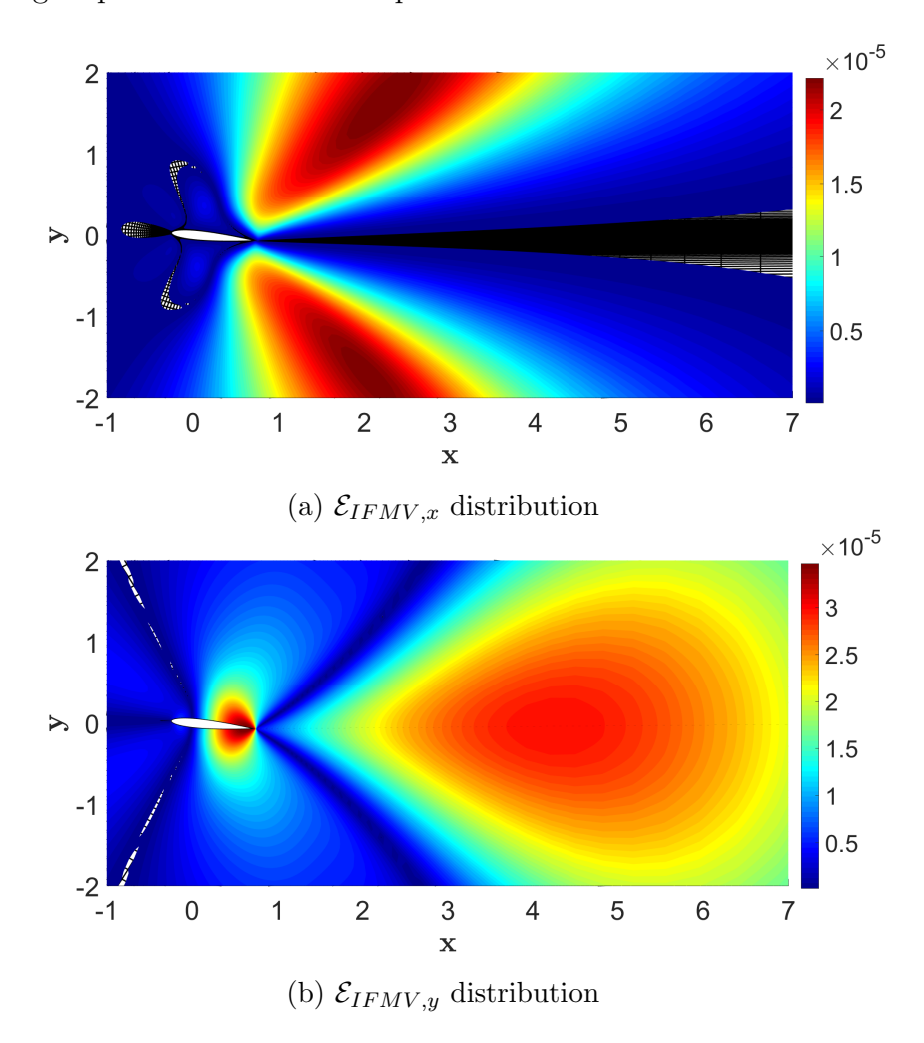


Figure 5–10: Error distributions on the IFMV for the pitching NACA0012 case at $\pm 20^\circ$ and $\kappa = 3$

The relative errors on the mean pressure coefficient at the surface of the airfoil and the mean wall shear stresses are presented on the Figure 5–12. It is observed that the relative error is much more significant for the wall shear stress which is required in the computation of the skin-friction drag coefficient than on the pressure coefficient which intervenes in the evaluation of the pressure drag. In addition, the errors are higher for the (NLFD-LVI) method than the (NLFD-AEVI) methodology which is consistent with the compared accuracy of both methods to compute the IFMV.

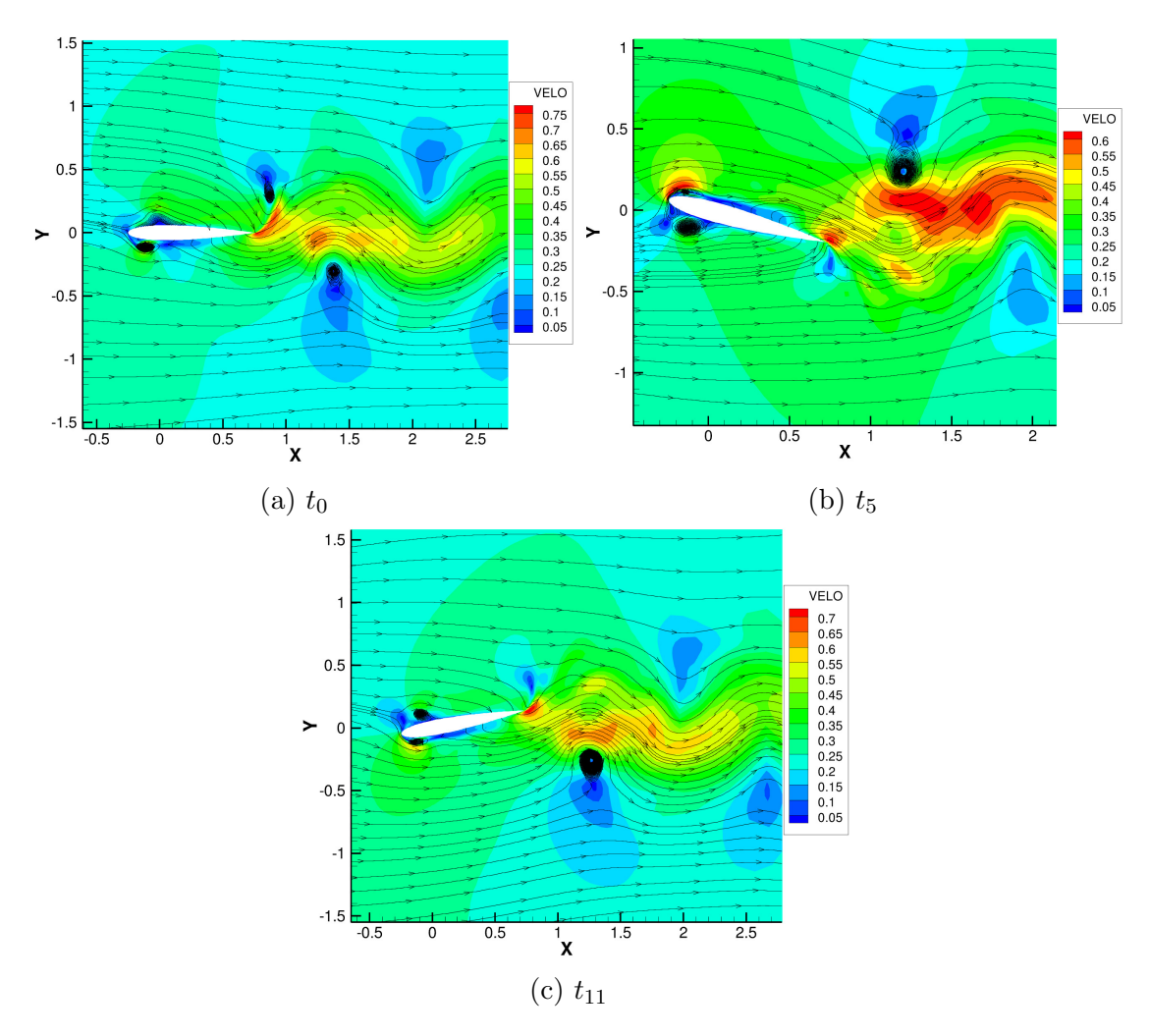


Figure 5–11: Fluid velocity contours and streamlines for the pitching NACA0012 case at $\pm 20^{\circ}$ and $\kappa = 3$ at time instances t_0 , t_5 and t_{10}

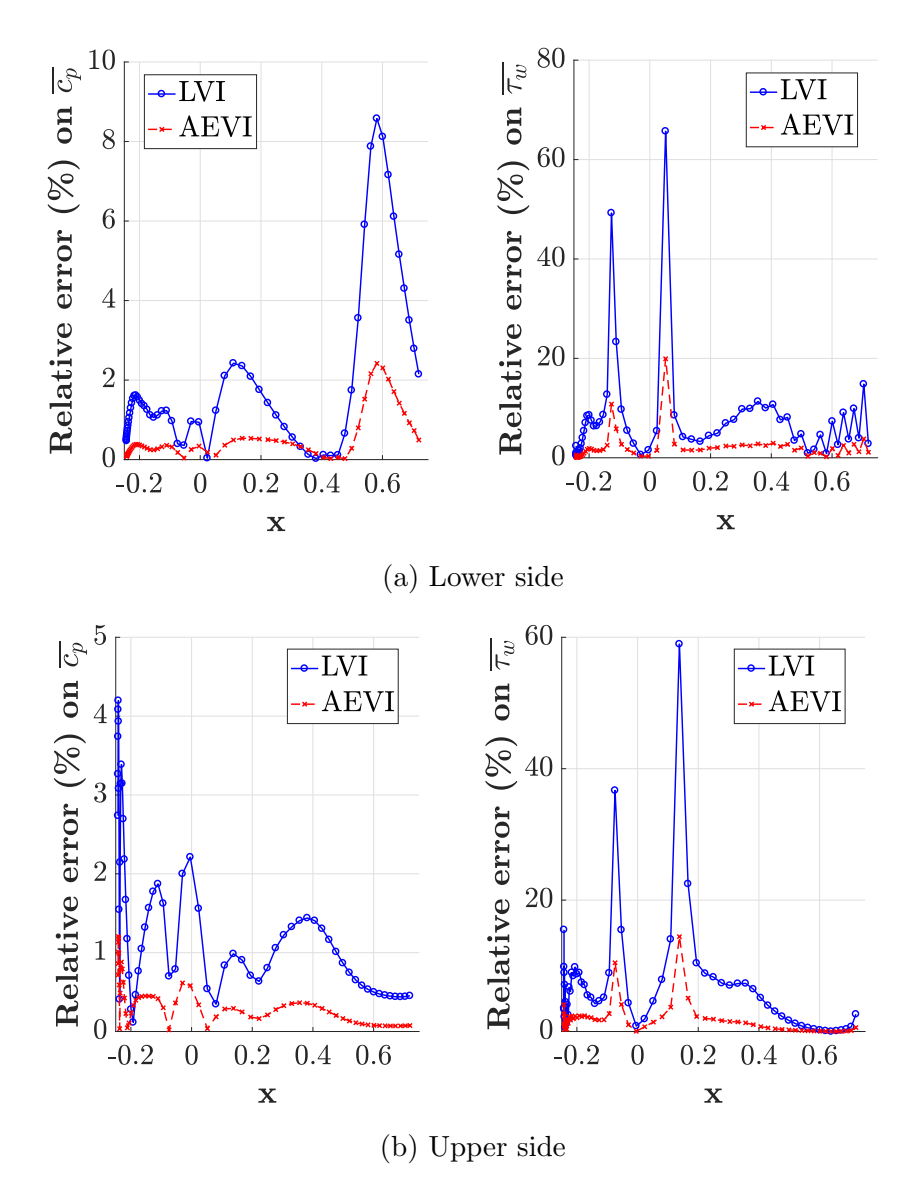


Figure 5–12: Relative errors on the mean pressure coefficient $\overline{c_p}$ and the mean wall shear stress $\overline{\tau_w}$ for the pitching NACA0012 case at $\pm 20^\circ$ and $\kappa=3$ at a time instance $t_5=\frac{5}{11}T$

5.5 Discussion

The different methodologies are compared based on five simple test cases. First, it was shown that for linear motions, no differences are observed and all methods are equivalent which is analytically expected. In addition it was also demonstrated that, the convergence of the GCL and IFMV is independent of the convergence of the aerodynamic coefficients.

For problems with more complex mesh motions, in the case of "small" deformations ($\pm 10^{\circ}$ pitching cylinder and $\pm 5^{\circ}$ pitching NACA0012 airfoil), differences between the methodologies to compute the time-average behavior of the drag coefficients were found to be below 0.01% relative to the mapping method for any number of harmonics, while the instantaneous behavior could present more significant distinctions which reduce as the number of harmonics increase in the temporal discretization. The order of magnitude of these differences being less than one drag count, would not be further investigated in industry. However as the non-linearity of the motion becomes more significant for "large" deformation amplitude ($\pm 20^{\circ}$ pitching NACA0012 airfoil), differences over twenty drag counts are observed even for a reasonable number of harmonics of five employed for the temporal discretization which corresponds to a level of convergence of the GCL around 10^{-9} using the mapping method and to IFMV converged between 10^{-4} to 10^{-5} using the NLFDbased methods. From the levels of convergence, it appears that the differences are mainly due to the inaccuracy of the IFMV and that enforcing solely the GCL does not guarantee the most accurate results.

In summary, the performances of the different methodologies are quite comparable regarding the average aerodynamic coefficients as long as the non-linearity of the mesh deformation is not too "large". The limits of each method appear for small number of harmonics, where the level of convergence of the GCL is low using the BI-MAP method while the level of convergence of the integrated face mesh velocities is low using the NLFD-based methods. However, at higher number of harmonics, the BI-MAP approach begins to satisfy the GCL, while the inaccurate IFMV from the NLFD-based methods appear to affect the accuracy of integrated function values such as the drag and lift coefficients.

CHAPTER 6 Conclusion and future work

The satisfaction of the Geometric Conservation Law (GCL) is essential to avoid the introduction of numerical errors or inaccuracies in the solution. The limitations of the initial approach proposed by Tardif and al. [37] were discussed. It was shown that this method satisfies the GCL with possibly non converging integrated face mesh velocities since it is based on a linear representation of the volumetric increments. Thus the approach of Tardif and al. [37] is ill-suited for complex non-linear motions.

Novel approaches were developed for both the Non-Linear Frequency Domain and the Time-Spectral methods to enforce the GCL. These methodologies are based on the computation of the Integrated Face Mesh Velocities (IFMV) through the evaluation of the Approximated Exact Volumetric Increments (NLFD-AEVI) or a mapping between the physical domain and the computational space (MAP). The techniques were thoroughly investigated both analytically and numerically in order to determine their accuracy and limitations. The NLFD-AEVI method was shown to satisfy GCL with first-to-second order accurate IFMV while the mapping-based methodologies enforce the GCL with a spectral rate of convergence through the computation of the exact integrated face mesh velocities. Hence it was proven that

satisfying the GCL does not guarantee that the errors in the integrated face mesh velocities are either at the same level or converge at the same rate. The different methods were demonstrated for both two-dimensional quadrilateral and three-dimensional hexahedral grids.

The comparison of the different methods on aerodynamic simulations were performed for plunging or pitching motions of a cylinder and a NACA0012 airfoil. For linear motions, all the methods are equivalent and produce the same results. Depending on the degree of non-linearity of the mesh motion, differences appear between the methods which can become significant for "large" mesh deformations. It was observed that the differences on the drag coefficients decrease as the temporal discretization is refined but may persist to be above one drag count and thus deserve further consideration from an industrial point of view. Lastly, it was shown that the rate of convergence of the Geometric Conservation Law is independent from the rate of convergence of aerodynamic coefficients.

Additional investigation of three-dimensional aerodynamic performances which would allow for more complex mesh deformations is needed to evaluate the differences between the developed methodologies. The correct determination of the impact of the GCL as well as the IFMV on aerodynamic computation is fundamental in order to evaluate the accuracy of the flow solver. Indeed for a pitching airfoil with a large pitching angle, the separation of the flow is convected along the chord in the downstream direction and Rigid Grid Motion is not sufficient to preserve the cell density in the wake, thus dynamic mesh deformation along with the GCL satisfaction is essential for such simulations. Moreover these future investigations should not be

only restricted to aerodynamic coefficients but expanded to Limit Cycle Oscillation in aeroelastic cases in order to further extend the current in-house solver.

References

- [1] Y. Allaneau and A. Jameson. Direct Numerical Simulations of Plunging Airfoils. In 48th AIAA Aerospace Sciences Meeting & Exhibit, Orlando, Florida, Jan 2010. American Institute of Aeronautics and Astronautics.
- [2] J. Blajek. Computational Fluid Dynamics: Principles and Applications. Elsevier, 1988.
- [3] N. Butsuntorn and A. Jameson. Time spectral method for rotorcraft flow. In 46th AIAA Aerospace Sciences Meeting & Exhibit, Reno, Nevada, Jan 2008. American Institute of Aeronautics and Astronautics.
- [4] J.-S. Cagnone and S. Nadarajah. Implicit nonlinear frequency-domain spectraldifference scheme for periodic euler flow. AIAA Journal, 47(2):361–372, Feb 2009.
- [5] J. K. Dukowicz. Efficient volume computation for three-dimensional hexahedral cells. *Journal of Computational Physics*, 74(2):493–496, Feb 1988.
- [6] S. Étienne, A. Garon, and D. Pelletier. Perspective on the geometric conservation law and finite element methods for ALE simulations of incompressible flow. *Journal of Computational Physics*, 228(7):2313–2333, Apr 2009.
- [7] C. Farhat, P. Geuzaine, and C. Grandmont. The Discrete Geometric Conservation Law and the Nonlinear Stability of ALE Schemes for the Solution of Flow Problems on Moving Grids. *Journal of Computational Physics*, 174(2):669–694,

Dec 2001.

- [8] A. Gopinath and A. Jameson. Time spectral method for periodic unsteady computations over two- and three- dimensional bodies. In 43rd AIAA Aerospace Sciences Meeting & Exhibit, Reno, Nevada, Jan 2005. American Institute of Aeronautics and Astronautics.
- [9] A. Gopinath and A. Jameson. Application of the time spectral method to periodic unsteady vortex shedding. In 44th AIAA Aerospace Sciences Meeting & Exhibit, Reno, Nevada, Jan 2006. American Institute of Aeronautics and Astronautics.
- [10] H. Guillard and C. Farhat. On the significance of the geometric conservation law for flow computations on moving meshes. Computer Methods in Applied Mechanics and Engineering, 190(11-12):1467–1482, Dec 2000.
- [11] K. C. Hall and W. S. Clark. Linearized euler predictions of unsteady aerodynamic loads in cascades. *AIAA Journal*, 31(3):540–550, Mar 1993.
- [12] K. C. Hall and E. F. Crawley. Calculation of unsteady flows in turbomachinery using the linearized euler equations. *AIAA Journal*, 27(6):777–787, June 1989.
- [13] K. C. Hall, J. P. Thomas, and W. S. Clark. Computation of unsteady nonlinear flows in cascades using a harmonic balance technique. AIAA Journal, 40(5):879– 886, May 2002.
- [14] Michael J. Hemsch. "statistical analysis of computational fluid dynamics solutions from the drag prediction workshop. Journal of Aircraft, 41(1):95–103, Jan-Feb 2004.

- [15] C. W. Hirt, A. A. Amsden, and J. L. Cook. An arbitrary Lagrangian-Eulerian computing method for all flow speeds. *Journal of Computational Physics*, 135(2):203–216, Aug 1997.
- [16] A. Jameson. Analysis and design of numerical schemes for gas dynamics, 1: artificial diffusion, upwind biasing, and their effect on accuracy and multigrid convergence. *International Journal of Computational Fluid Dynamics*, 4(3):171– 218, 1995.
- [17] A. Jameson, W. Schmidt, and E. Turkel. Numerical solution of the Euler equations by finite volume methods using Runge Kutta time stepping schemes. In 14th Fluid and Plasma Dynamics Conference, Palo Alto, California, Jun 1981. American Institute of Aeronautics and Astronautics.
- [18] P. Knabner, S. Korotov, and G. Summ. Conditions for the invertibility of the isoparametric mapping for hexahedral finite elements. Finite Elements in Analysis and Design, 40(2):159–172, Dec 2003.
- [19] B. Koobus and C. Farhat. Second-order time-accurate and geometrically conservative implicit schemes for flow computations on unstructured dynamic meshes. Computer Methods in Applied Mechanics and Engineering, 170(1-2):103–129, Feb 1999.
- [20] M. Lesoinne and C. Farhat. Geometric conservation laws for flow problems with moving boundaries and deformable meshes, and their impact on aeroelastic computations. Computer Methods in Applied Mechanics and Engineering, 134(1-2):71–90, Jul 1996.

- [21] J. I. López, M. Brovka, J. M. Escobar, R. Montenegro, and G. V. Socorro. Strategies for optimization of hexahedral meshes and their comparative study. Engineering with Computers, 33(1):33–43, Jan 2017.
- [22] D. J. Mavriplis and C. R. Nastase. On the geometric conservation law for highorder discontinuous Galerkin discretizations on dynamically deforming meshes. *Journal of Computational Physics*, 230(11):4285–4300, may 2011.
- [23] D. J. Mavriplis and Z. Yang. Construction of the discrete geometric conservation law for high-order time-accurate simulations on dynamic meshes. *Journal of Computational Physics*, 213(2):557–573, Apr 2006.
- [24] M. McMullen, A. Jameson, and J. Alonso. Application of a non-linear frequency domain solver to the euler and navier-stokes equations. In 40th AIAA Aerospace Sciences Meeting & Exhibit, Reno, Nevada, Jan 2002. American Institute of Aeronautics and Astronautics.
- [25] M. S. McMullen and A. Jameson. The computational efficiency of non-linear frequency domain methods. *Journal of Computational Physics*, 212(2):637–661, Mar 2006.
- [26] M. S. McMullen, A. Jameson, and J. Alonso. Demonstration of nonlinear frequency domain methods. AIAA Journal, 44(7):1428–1435, Jul 2006.
- [27] A. Mosahebi. An Implicit Adaptive Non-Linear Frequency Domain Method for Periodic Viscous Flows on Deformable Grids. PhD thesis, McGill University, 2012.
- [28] A. Mosahebi and S. Nadarajah. An adaptive nonlinear frequency domain method for viscous periodic steady state flows. In 48th AIAA Aerospace Sciences

- Meeting Including the New Horizons Forum and Aerospace Exposition, Orlando, Florida, Jan 2010. American Institute of Aeronautics and Astronautics.
- [29] A. Mosahebi and S. Nadarajah. An implicit adaptive non-linear frequency domain method (pnlfd) for viscous periodic steady state flows on deformable grids. In 49th AIAA Aerospace Sciences Meeting including the New Horizons Forum and Aerospace Exposition, Orlando, Florida, Jan 2011. American Institute of Aeronautics and Astronautics.
- [30] A. Mosahebi and S. Nadarajah. Algorithmic advanced for the adaptive non-linear frequency domain method. In 51st AIAA Aerospace Sciences Meeting including the New Horizons Forum and Aerospace Exposition, Dallas/Ft. Worth, Texas, Jan 2013. American Institute of Aeronautics and Astronautics.
- [31] A. Mosahebi and S. Nadarajah. An implicit and adaptive nonlinear frequency domain approach for periodic viscous flows. *Journal of Computational Physics*, 278:92–116, Dec 2014.
- [32] S. Nadarajah. Convergence studies of the time accurate and non-linear frequency domain methods for optimum shape design. *International Journal of Computational Fluid Dynamics*, 21(5-6):189–207, Jun 2007.
- [33] B. Nkonga and H. Guillard. Godunov type method on non-structured meshes for three-dimensional moving boundary problems. *Computer Methods in Applied Mechanics and Engineering*, 113(1–2):183–204, Mar 1994.
- [34] G. Pedro, A. Suleman, and N. Djilali. A numerical study of the propulsive efficiency of a flapping hydrofoil. *International Journal for Numerical Methods* in Fluids, 2003.

- [35] W. E. Pracht. Calculating three-dimensional fluid flows at all speeds with an Eulerian-Lagrangian computing mesh. *Journal of Computational Physics*, 17(2):132–159, Feb 1975.
- [36] P.L. Roe. Approximate Riemann Solvers, Parameter Vectors, and Difference Schemes. *Journal of Computational Physics*, 135(2):250–258, Aug 1997.
- [37] P.-O. Tardif and S. Nadarajah. Three-dimensional aeroelastic solutions via the nonlinear frequency-domain method. AIAA Journal, 55(10):3553–3569, Jul 2017.
- [38] P. D. Thomas and C. K. Lombard. Geometric Conservation Law and Its Application to Flow Computations on Moving Grids. AIAA Journal, 17(10):1030–1037, Oct 1979.
- [39] H. Wendland. Piecewise polynomial, positive definite and compactly supported radial functions of minimal degree. Advances in Computational Mathematics, 4(1):389–396, Dec 1995.
- [40] S. Yang. Computation of the Flows over Flapping Airfoil by the Euler Equations. In 43rd AIAA Aerospace Sciences Meeting & Exhibit, Reno, Nevada, Jan 2005. American Institute of Aeronautics and Astronautics.
- [41] J. Young and J. Lai. Oscillation Frequency and Amplitude Effects on the Wake of a Plunging Airfoil. *AIAA Journal*, 42(10):2042–2052, Oct 2004.
- [42] J. Young and J. Lai. On the aerodynamic forces of a plunging airfoil. *Journal* of Mechanical Science and Technology, 2007.
- [43] H. Zhang, M. Reggio, J. Y. Trépanier, and R. Camarero. Discrete form of the GCL for moving meshes and its implementation in CFD schemes. *Computers*

- and Fluids, 22(1):9-23, Jan 1993.
- [44] Shangyou Zhang. On the nested refinement of quadrilateral and hexahedral finite elements and the affine approximation. *Numerische Mathematik*, 2004.
- [45] P. Zwanenburg and S. Nadarajah. Equivalence between the Energy Stable Flux Reconstruction and Filtered Discontinuous Galerkin Schemes. *Journal of Com*putational Physics, 306:343–369, Feb 2016.